The Dissertation Committee for John Raymond Jardel
certifies that this is the approved version of the following dissertation:

Measuring Dark Matter Profiles Non-parametrically in Dwarf Spheroidal Galaxies

Committee:

Karl Gebhardt, Supervisor

Shardha Jogee

John Kormendy

Miloš Milosavljević

Louis Strigari

Measuring Dark Matter Profiles Non-parametrically in Dwarf Spheroidal Galaxies

by

John Raymond Jardel, B.S.; M.A.

DISSERTATION

Presented to the Faculty of the Graduate School of

The University of Texas at Austin

in Partial Fulfillment

of the Requirements

for the Degree of

DOCTOR OF PHILOSOPHY

THE UNIVERSITY OF TEXAS AT AUSTIN

May 2014

For my parents, John and Mary

Acknowledgments

This thesis represents the culmination of six years of very hard work for very little pay. That's six years of late nights and early mornings. Six years spent in a windowless office drinking way too much coffee. Six years of dealing with buggy code (including a six month period where all I did every day was try to find a seg fault). Six years of hardware failures and bad weather for observing. Six years of angry referee reports. At the same time, it was also six years of learning. Six years of uncovering truths about the universe that no one knew before. Six years of travel to cool places. Six years of setting my own schedule and being accountable to no one but myself. And if I had to do it all again, I'd do it in a heartbeat.

I have many people to thank for the scientific content of this thesis. I thank my advisor, Karl Gebhardt, for giving me the independence that allowed me to succeed in graduate school. I thank my committee members: Shardha Jogee, John Kormendy, Miloš Milosavljević, and Louis Strigari. There are many others to thank, but at the top of the list is Remco van den Bosch, whom I called my "de facto advisor" for the first few years.

On a personal note, I owe my sanity to the incredible friendships I developed over these six years. I was fortunate to enter the program with a class that, I'll wager, is the most outgoing, friendly, fun-loving bunch of astrophysicists ever found in any graduate program. I made too many close friends to name them all, but

special honors go to Paul, Manos, Chalence, JJ, Chris, Irina, Keaton, Kevin, Taylor, Jacob, Sean, Joel, Casey, Eric, Jeremy, Josh, Ross, Amy, Remco, Randi, and the Amandas. I thank everyone else that shared their time with me, especially the regulars at Friday happy hours at the Crown, those involved in Astrovolley volleyball, the Ultra Deep Fielders (our astro softball team), and the #weirdnight crew. I owe sincere thanks to Tom Montemayor—the "Patron Saint" of graduate students—for the countless boat parties, land parties, and volleyball strategy sessions (a.k.a. parties). I also give my heartfelt thanks to my girlfriend, Katharine Heffner; you made this last (and most stressful) year the happiest of my life.

Finally, I thank my family for their constant support of me. My parents, John and Mary, and my sister Jaclyn have always been my biggest cheerleaders. Your support means the world to me, and I couldn't have done this without you.

As I leave the ivory tower of academia for the 9-5 of the real world, I'd like to pause for a moment to put a proper bookend on this chapter of my life. This has been an incredible experience for me, but the following quote sums up my feelings most appropriately.

> Science is a wonderful thing if one does not have to earn one's living at it.
>
> - Albert Einstein

Measuring Dark Matter Profiles Non-parametrically in Dwarf Spheroidal Galaxies

Publication No. _____

John Raymond Jardel, Ph.D.
The University of Texas at Austin, 2014

Supervisor: Karl Gebhardt

Although exotic objects like supermassive black holes (SMBHs) and dark matter halos do not emit or interact with light, we can still detect them across the vastness of space. By observing the gravitational dance of objects we can see, astronomers are able to infer the mass of the invisible objects they orbit. This has led to the discovery that nearly every massive galaxy hosts a SMBH at its center, and has confirmed that every galaxy is embedded in an extended halo of dark matter. However, the practice of inferring mass from the motions of bright kinematics tracers has many complications, not the least of which is that we seldom observe more than the line-of-sight component of the instantaneous velocity of a star. Consequently, astronomers must build dynamical models of the galaxies they wish to study. These models often rely on overly restrictive assumptions, or are crippled by degeneracies amongst their parameters and lack predictive power.

In this thesis, I introduce a significant advancement into the field of dynamical modeling. My modeling technique is based on the powerful principle of orbit superposition, also known as Schwarzschild Modeling. This technique is robust to many of the degeneracies associated with dynamical modeling, and has enjoyed much success in measuring the SMBHs and dark matter halos of large elliptical or bulge-dominated galaxies. I use it in Chapter 2 to accurately measure the SMBH in the Sombrero Galaxy (NGC 4594) and to constrain its dark matter halo. Unfortunately, when measuring dark matter halos with Schwarzschild Modeling, the modeler is required to adopt a parameterization for the dark matter density profile $\rho_{DM}(r)$. Often this is precisely the quantity one wishes to measure. To avoid this reliance on a priori parameterizations, I introduce a technique that calculates $\rho_{DM}(r)$ non-parametrically. Armed with this powerful new technique, I set out to measure the distribution of dark matter in the halos of some of the smallest galaxies in the Universe.

These dwarf spheroidal galaxies (dSphs) orbit the Milky Way as satellites, and their dark matter content has been studied extensively. However, the models used to probe their halos have been simplistic and required overly restrictive assumptions. As a result, robust conclusions about their dark matter content have remained elusive. Into this controversial and active area of study, I bring Non-Parametric Schwarzschild Modeling. The results I find offer the most robust and detailed measurements of the dark matter profiles in the dSphs to date.

I begin my study with the first application of standard Schwarzschild Modeling to any dSph galaxy by using it in Chapter 3 on Fornax. This chapter details the

process of re-tooling Schwarzschild Modeling for the purpose of measuring these small galaxies. In Chapter 4, I introduce the fully non-parametric technique, and apply it to Draco as proof of concept. Chapter 5 presents the main results of this thesis. Here I apply Non-Parametric Schwarzschild Modeling to Draco, Carina, Fornax, Sculptor, and Sextans. By relaxing the assumption of a parameterization for $\rho_{DM}(r)$, I find a variety of profile types in these five galaxies—some of which are consistent with past observations, others consistent with predictions from simulations, and still others were completely unanticipated. Finally, in Chapter 6 I describe the modeling of these galaxies in more detail. I demonstrate the accuracy of Non-Parametric Schwarzschild Modeling by recovering a known $\rho_{DM}(r)$ from artificial simulated data. I also expound upon the modeling results by presenting the detailed orbit structure of the five dSphs. Lastly, I compare my results to hydrodynamical simulations to explore the link between dark matter profile type and the baryon content of the dSphs.

Table of Contents

List of Tables

List of Figures

Chapter 1

Introduction

Light, seeking light, doth light of light beguile;
So ere you find where light in darkness lies,
Your light grows dark by losing of your eyes.

Shakespeare - "Love's Labour's Lost"

In most fields of science, experiments can be designed, variables controlled for, and, in general, the objects under study can be manipulated directly. When one wishes to study a star, a galaxy, or even the Universe itself, this strategy is clearly impossible. Instead, the astronomer's toolbox contains only the light emitted by distant sources and a profound understanding of the laws of the natural Universe.

If this is challenging enough when one's objects actually emit light, it might seem impossible to study the mysteries of black holes and dark matter which, by definition, do not emit light for us to study. Instead, we divine these objects' presence by detecting their influence on bodies that do emit light. The key to this entire process lies in understanding the gravitational influence that black holes and dark matter exert on stars or gas in galaxies. Indeed, the entirety of this thesis is devoted to studying the motions of stars to infer the presence of unseeen mass, a process known as dynamical modeling.

1.1 Dark Matter and Galaxies

Galaxies like our Milky Way are vast collections of stars, gas, and dust bound together by the force of gravity. They range in size from the smallest dwarfs with luminosities $L \sim 300 L_{\odot}$ up to the giant elliptical galaxies found in the centers of galaxy clusters with $L \sim 10^{12} L_{\odot}$. A convenient way to organize the diverse zoo of galaxy types is to divide them into two classes based on their shape: flattened disky systems or puffed-up spheroidal systems. The fundamental difference between these classes is the method by which they support themselves against gravitational collapse. Flattened, or disk, galaxies are supported by the ordered motions of their stars on roughly circular orbits. Stars in ellipsoidal-shaped galaxies, on the other hand, orbit with more complicated patterns. In general, these systems are supported against gravity through the random motions of their stars. I focus on the latter class of galaxies in this thesis, as the methods required to model them are often more complex.

For most galaxies, a significant fraction of their mass is in the form of dark matter—a substance that neither emits light, nor interacts with it. Despite its ethereal nature, astronomers have determined that dark matter constitutes roughly 83% of the total matter densty of the universe (Komatsu et al., 2011). Shortly after the Big Bang, this dark matter was well-mixed with normal matter. Then, as the gravitational forces from matter overwhelmed the initial expansion of the universe on small scales, galaxies began to form. Hot gas that was accreted by these first galaxies was able to cool and lose energy—a freedom not allowed of the dissipationless dark matter particles. As a result, baryons migrated closer to the centers of these

new galaxies, leaving a triaxial halo of dark matter extending to much larger radii. Inside this halo, the gas eventually cooled enough to form stars.

With modern computing power, it is relatively easy to simulate the formation of these dark matter halos. Since the dark matter particles are dissipationless, they can only exchange energy through gravitational forces. Furthermore, since dark matter is the dominant component of mass in the universe, one only needs to simulate its behavior to learn much about the formation of structure. Such simulations look remarkably similar to our universe on large scales. This is seen as some of the strongest evidence for the Cold Dark Matter (CDM) theory of structure formation (Viel et al., 2008; Reid et al., 2010; Komatsu et al., 2011). In CDM, dark matter is cold (i.e. has little free-streaming velocity), dissipationless, and non-interactive. This description of dark matter has become a standard ingredient in any theory describing the formation of galaxies in the universe.

An interesting side effect came from these large-scale simulations. It was observed that each dark matter halo, regardless of when it first formed, how massive it was, or what kind of environment it was in, had a density distribution that could be parameterized by a single two-parameter function: the Navarro-Frenk-White (NFW) profile (Navarro et al., 1996b):

$$\rho_{\rm NFW}(r) = \frac{\rho_s r_s^3}{r(r^2 + r_s^2)}. \tag{1.1}$$

Inside the scale radius r_s, $\rho_{\rm NFW}$ decreases with logarithmic slope $\alpha = d\log\rho/d\log r = -1$, there is a transition region near $r \sim r_s$, and finally $\rho_{\rm NFW}$ falls off as $\alpha = -3$ for

$r \gg r_s$. This "Universal Density Profile" describes any bound system of dark matter from the smallest dwarf galaxy, to the largest galaxy cluster. The profile is called "cuspy" since $\rho_{\rm DM}$ increases as $r \to 0$. The discovery of this feature set off nearly two decades of observational studies comparing modeled dark matter profiles in real galaxies to the NFW profile.

Since the Navarro-Frenk-White papers, modern simulations with higher resolution have found the Einasto profile a better fit to the simulated halos (Navarro et al., 2004; Merritt et al., 2005; Gao et al., 2008; Springel et al., 2008; Navarro et al., 2010). Unlike the NFW profile, the inner portion of the Einasto profile does not have a constant slope of $\alpha = -1$, but instead α varies with radius according to a power law $\alpha(r) \propto r^n$. These profiles are still cuspy, although they can have shallower cusps than the NFW $\alpha = -1$ cusp (Stadel et al., 2009). Nevertheless, over a short radial range, these two families of functions look very similar. The differences are so small (see Figure 1.1) that observational results are still compared with the NFW profile, despite the formal preference for Einasto profiles over NFW profiles.

1.1.1 The Influence of Baryons on the Universal Density Profile

The portrait that CDM paints of galaxy formation in our universe is one that is painted with a broad brush. The large scale features are accurately captured, but when one examines the finer details, the portrait no longer represents reality. This is because CDM simulations lack an important component of the universe's content—baryons. In other words, these simulations do not form stars, and galaxies are described only as objects that live within dark matter halos. While this gets the

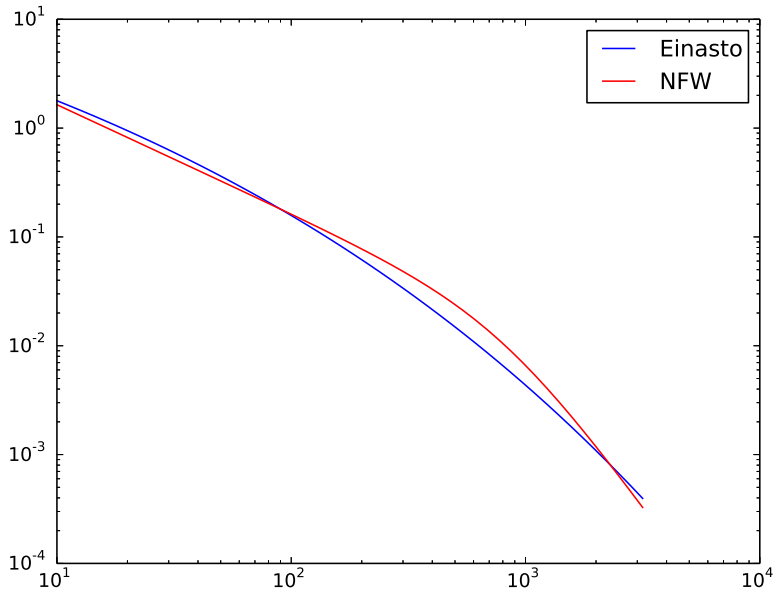

Figure 1.1 Comparison between an NFW profile and an Einasto profile. The inner portion of the NFW profile has a power-law slope of -1. The Einasto profile has a slope which varies as a power law. However, over a limited radial range the two profiles look quite similar.

large scale structure of the universe right, it neglects the details of individual galaxy formation. Any discussion of the dark matter density profile of real galaxies must be taken in that context.

So what kind of effect can baryons have on dark matter particles? They do not interact directly, so they experience no collisional forces. However, baryons are able to gain and lose energy in ways unavailable to the non-interacting dark matter. Therefore, their mass distribution is allowed to change through non-gravitational interactions. If this change is significant, and the local gravitational potential is dominated by the baryons, then the dark matter particles will be gravitationally influenced by the redistribution of baryons. Such processes are referred to as feedback, since they are generally second order effects.

The centers of galaxies are particularly vulnerable to feedback, as dissipative baryons outnumber their dark matter counterparts at small radii. Indeed, the process of growing a galaxy inside a dark matter halo is known to exert a compressive force on the halo, resulting in an increase in central dark matter densty. When changes to the halo are slow, this process is called adiabatic compression (Blumenthal et al., 1986). Other baryonic processes can cause a decrease in central density, and the shape of the dark matter profile is the result of the battle between these competing effects.

1.2 Observational Results

One of the most interesting aspects of CDM, and the primary topic of this thesis, is the prediction of the Universal Density Profile and the search to observe

this profile in nearby galaxies. To observe $\rho_{DM}(r)$ in a real galaxy, one must construct a model of that galaxy's gravitational potential. Such dynamical models use kinematics, either of stars or gas, to trace the potential and derive $\rho_{DM}(r)$. Instead of finding the cuspy NFW profile, early results studying low-mass disk galaxies found dark matter profiles that had flat, uniform-density central cores (Burkert, 1995; Persic et al., 1996; de Blok et al., 2001; Blais-Ouellette et al., 2001; Simon et al., 2005). This became known as the core/cusp debate (de Blok, 2010), and has motivated many studies to create dynamical models of nearby galaxies.

1.2.1 The Challenges of Dynamical Modeling

The principle of using the motions of stars (dynamics) to infer the gravitational presence of dark matter or a black hole is straightforward. Simply find a galaxy and look for stars moving suspiciously fast. These stars are likely moving fast because something is exerting a gravitational force on them. The more matter there is (of any kind) the stronger this force will be, and the faster it will cause the galaxy's stars to orbit. If the combined mass of everything we can see in the galaxy (stars, gas, planets, dust, etc.) is not enough to explain the mass inferred by the gravity measured, then this suggests the remaining mass is dark matter.

In practice, this procedure is complicated by a number of things. Since the distances involved in measuring a galaxy are so immense, it takes millions of years for stars to move enough for us to observe them. Thus, a galaxy today will look the same tomorrow, and we are rarely able to gain any time-dependent information. Instead, we measure the instantaneous velocities of stars using spectroscopy. Un-

fortunately, this limits our knowledge of the stars' velocities to only the component that falls along the line of sight; their transverse motions in the plane of the sky are completely unknown.

To deal with this challenge, we construct dynamical models of varying degrees of sophistication, depending on the problem at hand. For flat disk galaxies, one can usually assume the stars are on circular orbits and the modeling is simplified. In spheroidal galaxies, stars make more complicated orbits and this increases the complexity of the models needed to describe them. Often these models group stars located near each other and we describe their velocities in a statistical sense. We define the mean velocity V of these stars, and the velocity dispersion σ represents the degree with with these stars' velocities differ. Both of these quantities are intrinsically three-dimensional, but we only observe their components that lie along the line of sight. This lack of information sets a basic limit on the level of accuracy with which we can measure the mass of a galaxy and how it is distributed. More sophisticated models can guess at these unknown components of V and σ, using knowledge of the physics of galaxy dynamics, but this lack of information sets a fundamental limit to their accuracy.

1.2.1.1 The Jeans Degeneracy

The Jeans Equations offer a first look into how the velocities of stars encode information about the mass profile of a galaxy. In spherical symmetry, the Jeans Equation can be written:

$$M(r) = \frac{V^2 r}{G} - \frac{\sigma_r^2 r}{G}\left(\frac{\partial \ln \nu}{\partial \ln r} + \frac{\partial \ln \sigma_r^2}{\partial \ln r} + 2\beta(r)\right), \tag{1.2}$$

where $\nu(r)$ is the three-dimensional stellar light profile, G is Newton's gravitational constant, and $\beta(r)$ is called the anisotropy term. It represents the degree to which stars' orbits are radially or tangentially biased. This quantity is defined as $\beta \equiv 1 - \sigma_t^2/\sigma_r^2$, where σ_t is the tangential component of the three-dimensional velocity dispersion tensor $\overleftrightarrow{\sigma}$, and similarly σ_r is the radial component. Since we only ever have knowledge of the line-of-sight component of $\overleftrightarrow{\sigma}$, β is very difficult to constrain directly. Since β contributes to Equation 1.2 at the same level as the actual dynamics of the galaxy, this makes Jeans-based models highly sensitive to the anisotropy.

The "Achilles Heel" of Jeans models is the anisotropy; it is nearly impossible to constrain $\beta(r)$ from measurements of the line-of-sight components of V and σ alone. Consequently, some Jeans models attempt to simplify things and assume isotropy. However, Evans et al. (2009) show the assumption of isotropy forces spherical Jeans Models to recover constant-density profiles, and therefore biases results. The other approach is to parameterize $\beta(r)$ and run many models varying the parameters. This approach has two flaws: (1) nature is always better at finding ways to vary $\beta(r)$ than modelers are at parameterizing it, and (2) this approach marginalizes over our lack of knowledge of $\beta(r)$, therefore absorbing the uncertainty on $\beta(r)$ into the final mass profile $M(r)$. This leads to a strong degeneracy between mass and anisotropy, known as the Jeans Degeneracy.

To illustrate this, Wolf et al. (2010) plot the modeled mass profile for the Carina galaxy using the same set of kinematics but varying assumptions about the

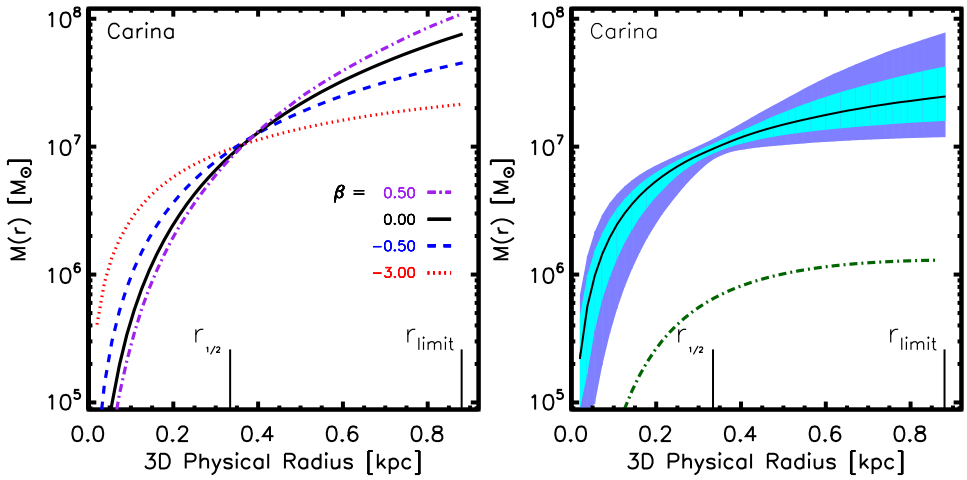

Figure 1.2 From Wolf et al. (2010), showing the strong dependence of $M(r)$ on anisotropy. The same kinematics are used for each model, but the anisotropy is allowed to vary between models. Left: anisotropy β is assumed to be constant with radius. Right: anisotropy is allowed to vary with radius according to an adopted parameterization for $\beta(r)$. The 68% and 95% confidence intervals are shown in color.

anisotropy. Figure 1.2 shows that variations in anisotropy preclude the level of precision needed to make meaningful measurements of $\rho_{DM}(r)$.

1.2.1.2 Schwarzschild Modeling

The Jeans Degeneracy is a fundamental limitation on the accuracy of dynamical models when simplifying assumptions are unrealistic (e.g. circular orbits, isotropy). There is simply not enough information in the projected velocity dispersion σ_p to break the degeneracy between mass and anisotropy. Fortunately, there is other information one can exploit to gain leverage over the anisotropy.

Instead of only using a group of stars' mean velocity V and projected dis-

persion σ_p, one can use the full distribution of the stars' line-of-sight velocities. These line-of-sight velocity distributions (LOSVDs) are centered about V with a width proportional to σ_p. Critically, their shapes contain information about the types of orbits the observed stars make (van der Marel & Franx, 1993). For example, stars on primarily radial orbits produce triangular-shaped LOSVDs, and stars on tangentially-biased orbits make LOSVDs that are flat-topped. By fitting to the full shape of the LOSVD, models can constrain the types of orbits the stars are on, and from that they gain information about the anisotropy and break the Jeans degeneracy.

Schwarzschild's orbit-superposition technique (Schwarzschild, 1979) is well-suited to exploit this advantage. Schwarzschild modeling, described in detail in later chapters, works by creating a library of all allowed stellar orbits for a modeled galaxy. These orbits are then weighted according to how well they can be combined to fit the observed LOSVDs of the galaxy being modeled.

Schwarzschild modeling has a long history of success measuring the supermassive black holes at the centers of large galaxies (van der Marel et al., 1998; Gebhardt et al., 2000a, 2003). For a thorough review of its history regarding black hole mass measurements, see Kormendy & Ho (2013). Relatively recently, it has been adapted to measuring dark matter profiles (Thomas et al., 2007b, 2009; Schulze & Gebhardt, 2011; Murphy et al., 2011) in large galaxies. In Chapter 3, I apply this powerful modeling tool for the first time to a dwarf galaxy with resolved stellar kinematics.

1.2.1.3 Assumptions about the Density Profile

Despite its many advantages over other forms of modeling, Schwarzschild models used to measure dark matter profiles have one glaring weakness. They require the modeler to adopt a parameterization for the density profile—precisely the thing they wish to measure. To mitigate this circular logic, a typical strategy is to adopt, for example, a cored profile as well as a cuspy profile. One then runs models with each parameterization, searching for each profile's best fitting model. The best fitting parameterization is the one with the overall lowest value of χ^2.

This strategy at least avoids begging the question; however, it is certainly not the most efficient way to measure $\rho_{\rm DM}(r)$. One must search for the χ^2 minimum for each parameterization to be tested. Even worse, this approach is obviously limited to finding only the types of profiles one asks it to find. Again, a common theme of this thesis is that nature is better at making distributions than we are at guessing parameterizations. Following this logic, I reason that it is better to ask "What is $\rho_{DM}(r)$?" than to ask "Does model x fit the data better than model y?".

In Chapter 4, I introduce a powerful improvement to Schwarzschild modeling that implements a procedure to calculate $\rho_{\rm DM}(r)$ directly, without assuming any parameterization. In later chapters, I apply the Non-parametric Schwarzschild technique to an interesting class of dwarf galaxies to construct the most general models of them to date. With these models, I find a variety of interesting density profiles including classical NFW-like cusps, observed constant-density cores, and profiles with shapes not observed before.

1.3 The Milky Way's Dwarf Spheroidals

I focus the majority of work in this thesis studying the dwarf spheroidal galaxies (dSphs) that orbit our Milky Way as satellites. They are some of the faintest galaxies ever observed, representing the extreme low end of the galaxy luminosity function. They are ellipsoidal in shape, supported against gravity by the random motions of their stars. This makes dynamical modeling significantly more challenging, as $\sigma \gg V$ in Equation 1.2, and it opens the can of worms that is the Jeans Degeneracy. Consequently, the dSphs require a proper treatment of the velocity anisotropy for accurate measurements of $\rho_{DM}(r)$.

Although the dSphs are important objects and have been studied extensively, the models used to measure their dark matter content have been limited to Jeans-based studies. As such, modelers have had to make the simplifying assumption of isotropy (Gilmore et al., 2007; Walker et al., 2007), or have been forced to marginalize over their ignorance of the anisotropy (Walker et al., 2009a; Wolf et al., 2010). Either approach is clearly less than desirable; there is low-hanging fruit here.

Perhaps one reason why Schwarzschild modeling has not been used extensively to study the dSphs is due to how kinematic data are collected for dSphs. Since the dSphs are relatively nearby, we can resolve individual stars even using ground-based observations. Unlike in more distant galaxies, single stars can be targeted with spectroscopy and their individual radial velocities can be obtained. For Jeans modelers and those using V and σ to describe their kinematics, calculation of these quantities amounts to taking statistical moments of the observed velocities. Since Schwarzschild modeling is based on fitting to the full distribution of velocities, the

analysis involves reconstructing the LOSVD from samples of discrete velocities. This process is known as density estimation, and statistical techniques exist to solve this problem (see Chapters 3 and 4). Building LOSVDs in this manner is fundamentally different from the way they are typically measured in larger, more distant galaxies where one must deconvolve the LOSVD from a spectrum of the integrated light of many thousands or millions of stars along the line of sight. Nevertheless, once LOSVDs are constructed for the dSphs, the application of Schwarzschild's technique is straightforward.

1.3.1 The Perfect Dark Matter Laboratories

The dSphs offer a number of attractive advantages when one wishes to study dark matter and galaxy formation. From a dynamical modeling perspective, they offer clean measurements of their dark matter density profiles. With mass-to-light ratios $M/L \gtrsim 10-100$ (Mateo, 1998; Simon & Geha, 2007), the stars can be largely ignored and treated as massless tracer particles in a potential defined by the dark matter halo. This simplifies the modeling significantly, and makes the dSphs ideal laboratories for studying dark matter.

Although the dominance of dark matter in the dSphs is helpful in modeling them, it raises an interesting question. How did the dSphs lose the majority of their baryons? Adopting the Cosmological Principle, we assume they were born with the same ratio of baryons to dark matter that all galaxies once had. Clearly some transformative event happened in their distant past that caused some dSphs to lose upwards of 99% of their baryon content.

A closer look at the star formation histories of the dSphs offers some insight into their past. Many show periods of extended bursty star formation, like that seen in dwarf irregular galaxies (Mateo 1998; Kormendy & Bender 2012 and references therein). However, no dSph has had any star formation in the last 10^8 years (Tolstoy et al., 2009; de Boer et al., 2012a), and many have had no star formation for much longer (Mateo, 1998; de Boer et al., 2012b). This, plus the lack of any detection of HI gas (Mateo, 1998), paints a picture of quenched star formation brought about by the sudden removal of gas.

The shallow potential wells of the dSphs make mass loss a plausible mechanism. However, to explain their large present day values of M/L we need the mass loss to be preferrentially baryonic. A natural source of this feedback can be found in outflows driven by supernovae. These can easily drive winds of 10,000 km s^{-1}. If the coupling of this energy to the galaxy's gas is even moderately efficient, then it will exceed the escape velocity and leave the system. A burst of star formation will translate to a burst of supernovae, so one can imagine a series of episodic supernova-driven winds clearing the interstellar medium of its gas reservoir.

Even though the winds from supernova have no direct effect on the dark matter, the gravitational perturbation caused by the immediate removal of gas can cause dark matter particles near the galaxy's center to gain energy. This results in a net decrease in the central dark matter density, and it is particularly strong if the central density has been enhanced by prior adiabatic compression. In effect, the baryons cool and fall to the center of the potential, dragging in dark matter with them. Then, they are instantaneously removed from the central region and the halo

rebounds outward (Dekel & Silk, 1986; Navarro et al., 1996a; Binney et al., 2001). Recent hydrodynamical simulations, which promise a more faithful treatment of baryonic processes such as cooling, star formation, and supernovae feedback, have found that this feedback mechanism can be particularly effective in transforming the cuspy NFW profile into a core under the right circumstances (Governato et al. 2012; Pontzen & Governato 2014; see Figure 1.3). Additionally, they find that the mechanism does not need to expel gas from the galaxy. Rather, they show that the gas must only leave the central region of the galaxy on timescales shorter than the dynamical time. If these modest conditions are acheived, then dark matter particles can irreversably gain energy and migrate outwards reducing a once cuspy profile to a core (Pontzen & Governato, 2012).

So it appears that measuring the dark matter profiles of the dSphs is useful for two reasons. First, their profile shapes are still hotly debated in the context of the core/cusp debate. Dynamical models that are robust to uncertainties in the anisotropy have the potential to put this debate to rest. Second, and perhaps more importantly, such measurements serve as observational constraints for a general theory outlining the interplay between dark matter and baryons. In Chapter 6, I place the dSphs on Figure 1.3 to test if supernova feedback can explain the variety of dark matter profiles I measure.

A third reason the dSphs are important is that they represent the smallest galaxies we can ever hope to study in detail with dynamical models. They are the final frontier for tests of CDM, and can teach us if galaxy formation changes in the low-mass regime. In fact, there is evidence that a change does occur at low

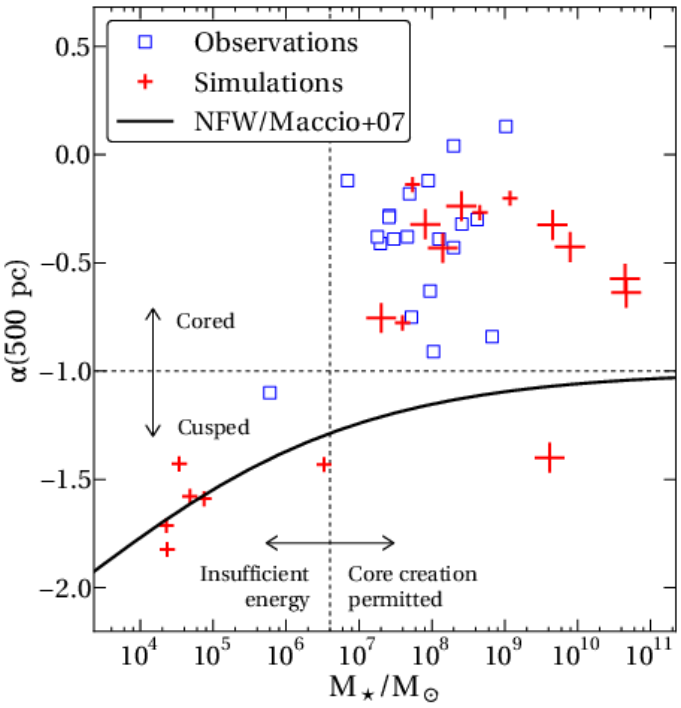

Figure 1.3 From Pontzen & Governato (2014) plotting dark matter density profile slope α (measured at $r = 500$ pc) versus stellar mass in simulated galaxies and observed HI-rich dwarf galaxies. The authors claim that more star formation results in more episodic supernova feedback, which lowers the density of the inner dark matter halo.

masses. The classic "Missing Satellites Problem" reveals that CDM simulations containing only dark matter vastly over-predict the number of low-mass subhalos that orbit the Milky Way (Moore et al., 1999; Klypin et al., 1999). To resolve this dispute, it is widely believed that there is a minimum mass that must be acheived before a galaxy forms inside a dark matter halo. Since we cannot observe empty halos, the Missing Satellites Problem may be a statement about the efficiency of star formation in low-mass halos.

It is relatively easy to believe that these would-be galaxies failed because their tiny potential wells were incapable of holding onto enough cold gas to form stars. Energetic phenomena such as supernovae outflows (Navarro et al., 1996a; Governato et al., 2012; Pontzen & Governato, 2014), the re-ionization of the universe (Bullock et al., 2000; Bovill & Ricotti, 2009), or ram-pressure stripping (Arraki et al., 2014) can easily impart sufficient energy for a small galaxy's gas supply to escape before it is able to cool and form stars. However, it has been recently claimed that some of these missing satellites are, in fact, more massive galaxies (Boylan-Kolchin et al., 2012). This constitutes a bigger problem for CDM, as it is unclear how massive subhalos could fail to form stars. However, the devil may be in the details of how baryons are able to interact with dark matter (Zolotov et al., 2012; Brooks et al., 2013). I return to this discussion in Chapter 6, armed with robust mass profiles for the five dSphs.

Chapter 2

Orbit-Based Dynamical Models of the Sombrero Galaxy (NGC 4594)[1]

> Astronomy, that micography of heaven, is the most magnificent of the sciences... Astronomy has its clear side and its luminous side; on its clear side it is tinctured with algebra, on its luminous side with poetry.
>
> Victor Hugo - *Post-scriptum de ma vie*

We present axisymmetric, orbit-based models to study the central black hole, stellar mass-to-light ratio, and dark matter halo of NGC 4594 (M104, the Sombrero Galaxy). For stellar kinematics, we use published high-resolution kinematics of the central region taken with the *Hubble Space Telescope*, newly obtained Gemini long-slit spectra of the major axis, and integral field kinematics from the SAURON instrument. At large radii, we use globular cluster kinematics to trace the mass profile and apply extra leverage to recovering the dark matter halo parameters. We find a black hole of mass $M_\bullet = (6.6 \pm 0.4) \times 10^8 M_\odot$, and determine the stellar $M/L_I = 3.4 \pm 0.05$ (uncertainties are the 68% confidence band marginalized over the other parameters). Our best fit dark matter halo is a cored logarithmic model with asymptotic circular speed $V_c = 376 \pm 12$ km s^{-1} and core radius $r_c = 4.7 \pm 0.6$

[1]Published in Jardel, J. R., Gebhardt, K., Shen, J., Fisher, D., Kormendy, J., Kinzler, J., Lauer, T. R., Richstone, D., and Gültekin, K., 2011, ApJ, 739, 21. Reprinted with permission from the American Astronomical Society.

kpc. The fraction of dark to total mass contained within the half-light radius is 0.52. Taking the bulge and disk components into account in our calculation of σ_e puts NGC 4594 squarely on the M-σ relation. We also determine that NGC 4594 lies directly on the M-L relation.

2.1 Introduction

Most galaxies are thought to host supermassive black holes (SMBHs) at their centers. The masses of these SMBHs have been observed to correlate with several properties of their host elliptical galaxies and of the classical bulge components of their host disk galaxies. For example, $M_\bullet$ correlates with galaxy/bulge mass (Dressler, 1989; Magorrian et al., 1998; Laor, 2001; McLure & Dunlop, 2002; Marconi & Hunt, 2003; Häring & Rix, 2004), luminosity (the M-L relation) (Kormendy, 1993; Kormendy & Richstone, 1995; Kormendy & Gebhardt, 2001; Gültekin et al., 2009b), velocity dispersion (the M-σ relation) (Ferrarese & Merritt, 2000; Gebhardt et al., 2000a; Tremaine et al., 2002; Gültekin et al., 2009b), and globular cluster content (Burkert & Tremaine, 2010; Harris & Harris, 2011). These and other, similar correlations suggest that galaxy formation and black hole growth are fundamentally linked. To better understand this interplay, accurate black hole masses are needed.

One challenge that limits the accuracy is the determination of the host galaxy's inclination. Projection effects are difficult to model and cause loss of information, leading to systematic uncertainties. Therefore, SMBHs in galaxies whose inclination is confidently known have the best chance of being accurately and robustly measured. Another issue that limits the accuracy is the effect a dark matter halo has on the determination of SMBH mass. Gebhardt & Thomas (2009) show that orbit-based models can underestimate black hole mass when dark matter is not considered in the modeling, however Schulze & Gebhardt (2011) find the effect is small when the black hole's sphere of influence is well-resolved.

NGC 4594 (M104, or the Sombrero Galaxy) is a nearly edge-on Sa type spiral with a prominent stellar disk and large, classical bulge (Kormendy & Kennicutt, 2004). The shape of this disk indicates that it (and thus the entire galaxy) is inclined at an angle very close to 90°. Throughout this paper we assume a distance to NGC 4594 of 9.8 Mpc, calculated from surface brightness fluctuations (Tonry et al., 2001). Unless otherwise stated, all distance-dependent quantities are scaled to this value. Tonry et al. (2001) use a value of $H_0 = 74$ km s^{-1} Mpc^{-1} in their distance determinations, however we compare our $M_\bullet$ and L_V to Gültekin et al. (2009b) who adopt $H_0 = 70$ in their work. We therefore scale the Gültekin et al. (2009b) distances down by 6%. Black hole mass scales as $M_\bullet \propto D$ and luminosity as $L_V \propto D^{-2}$; these quantities are adjusted accordingly.

NGC 4594 was one of the first galaxies in which a black hole was detected, and it has a long history of study. Kormendy(1988, hereafter K88) first found evidence for a massive black hole of $M_\bullet = 5.4^{+11.8}_{-3.7} \times 10^8\ M_\odot$ using only ground-based observations. With isotropic Jeans models, Emsellem et al. (1994b) measured a black hole of mass $M_\bullet = (5.4 \pm 0.5) \times 10^8\ M_\odot$. Later, Kormendy et al. (1996, hereafter K96) used high-resolution kinematics from the Faint Object Spectrograph (FOS) on the *Hubble Space Telescope* (*HST*)—the same data set we include—to measure $\log M_\bullet = 8.8 \pm 0.5\, M_\odot$. This corresponds to a mass of $5.8^{+12.4}_{-4.0} \times 10^8\, M_\odot$. With isotropic models, Magorrian et al. (1998) obtained a value of $M_\bullet = 6.9^{+0.2}_{-0.1} \times 10^8$ $M_\odot$. These values for $M_\bullet$ all lie towards the high mass end of the M-σ and M-L relations. Massive SMBH measurements are frequently being revised, and we expect the confidently known inclination of NGC 4594 to lead to one of the more secure

measurements of a high mass SMBH.

We present new Gemini spectroscopy of the major axis, as well as SAURON integral field kinematics covering the central region of the galaxy. We also use high-resolution *HST*/FOS kinematics of the nucleus and kinematics derived from globular clusters at large radii. We combine these kinematic datasets with *HST* and ground-based photometry to run axisymmetric orbit-based models. These models allow us to measure the black hole mass, stellar mass-to-light ratio, and dark matter halo of NGC 4594. In addition, we also recover information about the internal orbit structure of the galaxy.

2.2 Data Reduction and Analysis

Dynamical modeling requires as input the three-dimensional luminosity density distribution $\nu(r)$, as well as the line-of-sight velocity distribution (LOSVD) at many locations in the galaxy. We use *HST* and ground-based images for the photometry. Our kinematics include high-resolution *HST*/FOS spectra, long-slit spectra from GNIRS on Gemini, SAURON integral field kinematics, and individual velocities of globular clusters (GCs). We discuss each in turn.

2.2.1 Photometry

In order to cover a large enough dynamical range to have leverage on both the central SMBH and dark halo, we use surface brightness profiles from *HST* and ground-based images. The stellar disk of NGC 4594 dominates at intermediate radii on the major axis causing the isophotes in this region to be substantially flattened.

This abrupt change in ellipticity introduces an additional challenge to the deprojection. Our standard technique is to assume that the surfaces of constant luminosity density ν are coaxial, similar spheroids (Gebhardt et al., 1996). Clearly the presence of a disk invalidates this assumption, so we decompose the surface brightness into bulge and disk components, deprojecting each separately so that our assumption holds for each component. Afterwards, we re-combine the deprojected profile of each component $\nu_{\rm bulge} + \nu_{\rm disk}$ and input the total $\nu(r)$ into our modeling program.

The bulge-disk decomposition fits directly to a projected image. We construct a model disk by considering a Sersic (1968) profile:

$$\mu(R) = \mu_0 \exp[-(R/R_0)^{1/n}] \tag{2.1}$$

where μ_0 is the surface brightness at $R = R_0$ and n is the Sérsic index. For $n = 1$, the profile is an exponential. For inclinations other than 90°, the projection of our disk model is an ellipse. By specifying the inclination of the disk i, the axial ratio b/a of the ellipse is given by $b/a = cos\ i$ for a thin disk.

We construct many disk models by varying μ_0, R_0, i, and n (keeping n close to 1). Each model is then subtracted from the image until the residual brightness distribution has elliptical isophotes. The remaining light is assigned to the bulge component. A 1D major axis bulge profile is produced by averaging the bulge light in elliptical, annular isophotes. Hence, we are left with an analytic disk model and a non-parametric bulge model. We identify the best bulge and disk models as those that minimize the rms residuals of the model-subtracted image.

Table 2.1 Summary of Disk Parameters Fit

Disk	μ_0 (mag arcsec^{-2})	R_0 (arcsec)	n	i	
Outer 1	18.8	66.8	1.0	80	
Outer 2	16.7	40.1	1.0	80	
Nuclear	20.4	4.1	1.1	83	

In addition to the obvious main disk, NGC 4594 hosts a well-studied nuclear disk (Burkhead 1986, K88, K96) at small radii. We fit the nuclear disk in the *HST* image and the main disk in the ground-based image. Because we fit directly to the images, dust lanes and object masking become important. We keep a bad pixel list which instructs our code to ignore trouble spots. Dust lanes are selected by eye, while SExtractor (Bertin & Arnouts, 1996) is used to identify foreground stars, background galaxies, and globular clusters.

2.2.1.1 *HST* Image

To probe the nuclear region, we use a PSF-deconvolved *HST* Wide Field Planetary Camera 2 (WFPC2) image (GO-5512; PI: Faber). This image is presented in K96 and provides an excellent view of the central region of the galaxy. Centered on the PC1 camera, the image is taken in the F547M filter, and has a scale of $0\farcs0455$ pixel^{-1} of the central $34'' \times 34''$ of the galaxy. The PSF deconvolution uses the Lucy-Richardson algorithm (Richardson, 1972; Lucy, 1974) for 40 iterations and is well-tested on WFPC2 images (Lauer et al., 1998). The best fit parameters from the bulge-disk decomposition are listed in Table 2.1.

NGC 4594 is also thought to have weak LINER emission (Bendo et al., 2006) and there is a point source in the *HST* image. Furthermore, heavy dust ab-

sorption also makes the determination of the central bulge surface brightness profile difficult for $R \lesssim 0\farcs17$. To deal with these issues, we extrapolate the bulge surface brightness $\mu_{\rm bulge}(R)$ inwards to $R = 0\farcs02$ with a constant slope fit to the region near $R = 0\farcs17$. Figure 2.1 shows the result of this extrapolation, as well as the other components fit in the ground-based image.

2.2.1.2 Ground-Based Image

We obtained a wide-field, *I*-band image from the Prime Focus Camera on the McDonald 0.8 m telescope. This instrument provides a large unvignetted field of view (45×45 arcmin^2) and a single CCD detector. Therefore, we can more robustly carry out sky-subtraction and accurately constrain the faint isophotes. The image is corrected for bias, flat field, and illumination using standard routines in IRAF.

In our fit to the ground-based image, we ignore the central $20''$ due to over-exposure and contamination from the nuclear disk. We attempt fits in the region $20''-900''$ with only one stellar disk given by Equation (2.1), however these produce unacceptable residuals. Instead of modifying Equation (2.1), we add a second disk (in addition to the nuclear disk fit only in the *HST* image). This approach is similar to the Multi-Gaussian Expansion technique used to model the light distribution of bulges and ellipticals (Emsellem et al., 1994a). A summary of all components fit is given in Table 2.1 and plotted in Figure 2.1.

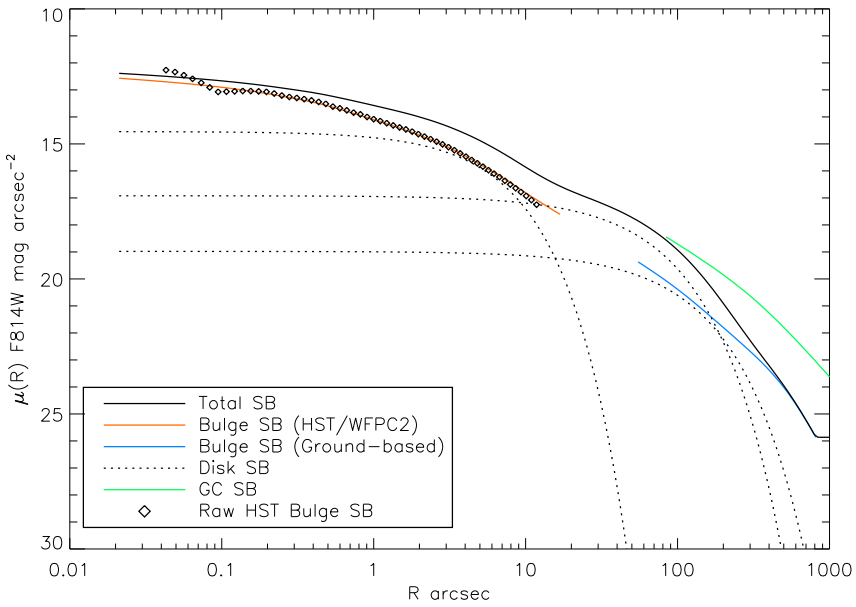

Figure 2.1 Radial plot of all resulting components from our bulge-disk decomposition along the major axis. Dotted lines are the disk profiles with parameters from Table 2.1. The solid black line is the total surface brightness (bulge + disks). Solid colored lines are the bulge profiles, the red line is the result from fits to the *HST* image, and the blue line is from the ground-based image. Diamonds indicate the raw *HST* bulge profile before we apply our dust correction and point-source removal. The gap between the *HST* and ground-based bulge profiles is interpolated over before deprojection. Plotted in green is the globular cluster surface brightness profile, arbitrarily scaled to match the stellar surface brightness at its innermost point.

2.2.1.3 Globular Cluster Profile

Globular clusters (GCs) are essentially bright test particles that allow us to probe the potential at radii where the stellar light is faint. They have been used in orbit-based models of other galaxies (Gebhardt & Thomas, 2009; Shen & Gebhardt, 2010; Murphy et al., 2011). To include them in our models, we use the GC number density profile (Rhode & Zepf, 2004) as an analog to the stellar density. The number density profile is converted to a surface brightness profile by arbitrarily adjusting the zero point to match the stellar profile in log space.

The green line in Figure 2.1 shows that the slope of the GC surface brightness profile is different from that of the stars. We run models using both the measured luminosity density distribution of the GCs and assuming that of the stars. We find significant preference for the measured GC profile.

2.2.1.4 Bulge Profile

Our bulge-disk decomposition returns a non-parametric form of the bulge profile. It is not necessary to have a parameterized bulge profile for our dynamical models, however we fit a Sérsic profile to ground-based bulge model using Equation (2.1). The bulge is well-fit by a Sérsic function, with the rms residuals equal to 0.08 mag arcsec^{-2}. We measure $\mu_0 = 13.5$ mag arcsec^{-2},$R_0 = 0.''1$, and $n = 3.7$.

We can convert the central surface brightness μ_0 and radius R_0 parameters to the more familiar "effective" parameters μ_e and R_e. The effective radius R_e is given by $R_e = (b_n)^n R_0$ and the effective surface brightness $\mu_e = \mu_0 + 2.5\log(e)\, b_n$ (Mackey & Gilmore, 2003). The factor b_n depends on n; an expansion for b_n can

be found in Mackey & Gilmore (2003). Applying these conversions, we obtain $\mu_e = 21.3$ mag arcsec^{-2} and $R_e = 156.2''$.

We obtain a simpler estimate for the half-light radius of the bulge from integration of the surface brightness profile; no fitting functions are required. We estimate $R_e = 117'' \pm 12''$. The integrated magnitudes are calculated for component x by $L_x = 2\pi \int I_x(r) r\, dr$. This does not take into account the ellipticity of each component, so we scale the luminosity by $L_x^{true} \approx (1-\epsilon_x)L_x$ where ϵ_x is the ellipticity of each component, assumed to be constant with radius. The bulge profile is known to become rapidly circular for $r \gtrsim 100''$ (Burkhead, 1986) so our procedure almost certainly underestimates $M_{\rm bulge}$ and B/T. These numbers are computed as a sanity check only, and do not affect the dynamical models.

The absolute integrated magnitudes are $M_{\rm disk} = -21.4$ and $M_{\rm bulge} = -22.5$ in F814W, corrected for Galactic extinction along the line of sight (Schlegel et al., 1998). Using the *HST* calibration package SYNPHOT (described in detail below), we convert these F814W magnitudes to V-band Vega magnitudes. We obtain $M_{V,\rm bulge} = -22.1$ and $M_{V,\rm disk} = -21.0$. These structural parameters lie exactly on the fundamental plane for bulges and ellipticals as presented in Kormendy et al. (2009). Our integrated magnitudes translate to a bulge-to-total ratio $B/T = 0.73$ with the nuclear disk contributing 1% of the total light. This value of B/T is lower than previous measurements—Kormendy et al. (2011) report $B/T = 0.925 \pm 0.013$. Our B/T, however, is in good agreement with a recent measurement by Gadotti & Sánchez-Janssen (2012, model BD). Regardless of the value of B/T, our dynamical models are unaffected, because we add all the bulge and disk light together again

after the deprojection.

We do not explore the possibility of fitting an exponential stellar halo in addition to a bulge and disk as Gadotti & Sánchez-Janssen (2012) do. Our bulge-disk decomposition produces a non-parametric bulge profile which could in principle be a combination of a Sérsic bulge plus exponential halo. However, this resulting profile is well-fit by a Sérsic function with n significantly larger than 1. We therefore do not agree with the claim made by Gadotti & Sánchez-Janssen (2012) that the bulge of NGC 4594 is actually an exponential stellar halo.

2.2.1.5 Deprojection

We combine the *HST* and ground-based bulge profiles by zero-pointing both to F814W. We calculate the F547M photometric zero point for the *HST* image from the SYNPHOT package in IRAF. Spectral template fitting (Section 2.2.2.1) shows that in the central region of the galaxy $\gtrsim 85\%$ of the light comes from K6III stars. We therefore convert the F547M zero point to F814W with SYNPHOT using the Bruzual Atlas[2] template for a K6III star.

Before deprojection, we extrapolate the one-dimensional profiles $\mu(R)$ with a constant slope to $R = 1800''$. The three disk profiles are then combined and deprojected via Abel inversion in the manner described in Gebhardt et al. (1996). We assume an inclination of $i = 90^\circ$. The inclinations of the combined disk components imply an ellipticity of $e = 0.83$. Our composite bulge profile is deprojected in a

[2]http://www.stsci.edu/hst/observatory/cdbs/bz77.html

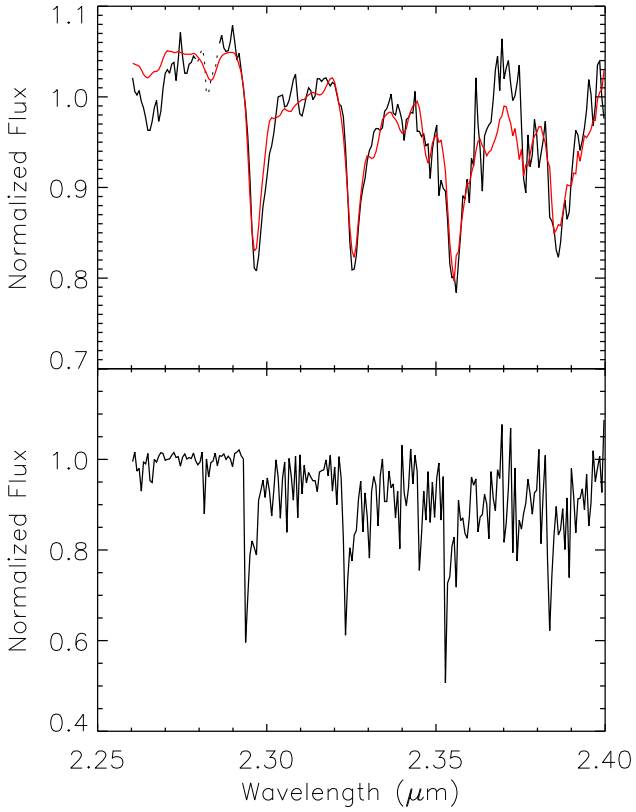

Figure 2.2 Example Gemini spectrum. Top: observed galaxy spectrum (black) and best-fit LOSVD-convolved template star (red). Dotted lines indicate regions of the spectrum ignored in the fit. Bottom: spectrum of the template star. The velocity dispersion of the LOSVD in this fit is $\sigma = 190 \pm 12\,\mathrm{km\ s^{-1}}$

similar fashion, assuming a constant ellipticity of 0.25 (Burkhead, 1986). We then add $\nu_{\mathrm{disk}}(r,\theta) + \nu_{\mathrm{bulge}}(r,\theta)$ to obtain the total luminosity density distribution $\nu(r,\theta)$ input to our models.

The globular cluster luminosity density profile is obtained via a similar deprojection, but with the additional assumption of spherical symmetry. The normalization of the GC light profile is irrelevant, as our models fit only to the slope of the

profile.

2.2.2 Kinematics

Kinematics for NGC 4594 come from four sources. The first uses near-IR data from Gemini/GNIRS long-slit observations along the major axis. These data were taken under good seeing conditions (around $0\farcs5$) and has high S/N. The second set comes from the Faint Object Spectrograph (FOS) on *HST* using the square aperture of $0\farcs21 \times 0\farcs21$ and is published in K96. The third set of data is from the SAURON instrument (Emsellem et al., 2004). The SAURON data for NGC 4594 have not been published previously. Individual velocities from globular clusters are our fourth source of kinematics. These data are published in Bridges et al. (2007). We describe each dataset in detail.

2.2.2.1 Gemini Kinematics

We use GNIRS (Elias et al., 2006) on the Gemini South Telescope to measure near-IR spectra of NGC 4594. The data were taken on 17 January, 2005. We placed the $150'' \times 0\farcs30$ slit along the major axis with the galaxy nucleus centered within the slit. We use a spatial pixel size of $0\farcs15$. With the 32l l/mm grating in 3rd order, we obtain a wavelength coverage of 19800–26200 Å at 6.4 Å per pixel. Using sky lines, we measure a resolving power around 1700 or an instrumental dispersion of 75 km s^{-1}. The total on-target exposure is 24 minutes, taken in 12, 2-minute individual exposures. Sky frames of equal exposure are taken throughout.

From both setup images and images of telluric standards, we measure a

FWHM in the spatial direction of $0\farcs5$, assuming a Gaussian distribution. We use this PSF for the dynamical models.

We use a custom pipeline to reduce the GNIRS data; however, it produces very similar results to the Gemini GNIRS reduction package. The pipeline includes dark subtraction, wavelength calibration for the individual exposures, sky subtraction, registration and summing.

There is adequate signal to extract kinematics out to a radius of $45''$. Figure 2.2 shows an example spectrum, where we plot the data in black and the template convolved with the best-fit line-of-sight velocity distribution (LOSVD). The velocity templates come from the GNIRS spectral library (Winge et al., 2009), where we select stars with a range of types from G dwarf to late giant. The kinematic extraction program performs a simultaneous fit to the LOSVD and relative weights of the templates. This procedure is described in Gebhardt et al. (2000a) and Pinkney et al. (2003). We present these data in the form of Gauss-Hermite moments in Table 2.2.

Figure 3.2 shows the kinematics derived from our analysis of the Gemini spectra. Between $1''$ and $5''$, V rises and σ drops. This is the result of the nuclear disk which becomes important at this radial range K88. Beyond $10''$, we see similar behavior in V and σ, it is caused by the main stellar disk.

2.2.2.2 *HST*/FOS Kinematics

K96 present *HST*/FOS kinematics of the nuclear region of NGC 4594. The FOS has a $0\farcs21 \times 0\farcs21$ aperture. There are three pointings with accurately known positions for NGC 4594 (GO-5512; PI: Faber). The dynamical models include the

exact placement and aperture size for the FOS pointing K96, and use the *HST* PSF (Gebhardt et al., 2000a).

2.2.2.3 SAURON Kinematics

We also include SAURON integral field kinematics The SAURON data are from a single pointing exposing on the central region, taken in the low resolution setting of the instrument (Bacon et al., 2001). In addition to V and σ, the SAURON data also include the higher order Gauss-Hermite moments h_3 and h_4. Details of the data reduction and analysis can be found in Bacon et al. (2001); Emsellem et al. (2004).

Our modeling code fits to the entire LOSVD rather than its moments, so we reconstruct LOSVDs from the Gauss-Hermite moments. We create 100 Monte Carlo realizations of a non-parametric LOSVD from the uncertainties in the Gauss-Hermite parameters of each SAURON bin (Gebhardt & Thomas, 2009). The 1433 reconstructed SAURON LOSVDs are spatially sampled more finely than our modeling bins. We therefore average the SAURON data to match our binning by weighting according to the uncertainties in the LOSVDs.

We re-construct Gauss-Hermite moments from the combined LOSVDs from the SAURON data for plotting purposes only. Figure 3.2 shows these moments near the major and minor axes. The major axis V for the SAURON data is significantly lower than that measured for the Gemini data. The reason for this is that SAURON data are binned to match the gridding of our model bins. Near the major axis, the bins range in polar angle from $\theta = 0 - 11^{\circ}$. These bins are described by a single

Table 2.2 Gemini Kinematics

R arcsec	V km s^{-1}	ΔV km s^{-1}	σ km s^{-1}	$\Delta\sigma$ km s^{-1}	h_3	Δh_3	h_4	Δh_4
0.00	19	14	253	16	-0.087	0.033	0.023	0.046
0.15	-36	11	257	12	-0.008	0.042	-0.016	0.038
0.30	-75	12	249	8	-0.053	0.048	-0.017	0.037
0.52	-112	11	234	8	0.020	0.037	-0.047	0.035
0.82	-144	12	221	9	0.060	0.038	-0.051	0.032
1.20	-172	9	202	9	0.065	0.039	0.003	0.031
1.73	-190	8	185	9	0.107	0.031	0.018	0.031
2.40	-208	7	184	9	0.089	0.032	0.024	0.031
3.30	-232	8	175	9	0.140	0.029	0.044	0.027
4.57	-236	9	171	7	0.173	0.032	0.023	0.027
6.45	-235	7	178	9	0.165	0.033	0.058	0.025
8.77	-189	11	203	11	0.028	0.039	-0.007	0.036
11.40	-171	10	192	10	0.071	0.033	-0.009	0.033
14.32	-187	16	185	15	0.227	0.042	0.102	0.060
17.70	-201	13	229	16	-0.023	0.042	0.020	0.050
22.20	-228	12	198	14	0.125	0.040	0.052	0.047
28.58	-235	11	194	14	0.122	0.042	0.036	0.051
36.08	-285	6	141	10	0.046	0.041	0.032	0.034
44.40	-277	7	149	9	0.094	0.042	0.101	0.039
-0.15	45	12	240	15	-0.026	0.034	0.002	0.041
-0.30	112	11	243	15	-0.052	0.036	-0.016	0.038
-0.52	130	10	224	15	-0.080	0.043	0.014	0.037
-0.82	162	8	212	10	-0.068	0.049	0.019	0.030
-1.20	176	7	206	11	-0.066	0.047	0.065	0.031
-1.73	205	7	190	12	-0.087	0.043	0.022	0.037
-2.40	226	7	173	12	-0.101	0.037	0.053	0.039
-3.30	244	9	187	11	-0.113	0.039	0.037	0.037
-4.65	246	8	184	12	-0.130	0.035	0.025	0.040
-6.15	237	9	220	14	-0.133	0.042	0.094	0.035
-8.40	221	9	211	13	-0.191	0.051	0.079	0.036
-10.95	162	9	209	14	-0.093	0.048	0.028	0.043
-14.25	178	9	198	14	-0.092	0.059	0.046	0.042
-19.20	204	10	198	17	-0.166	0.060	0.094	0.048
-24.52	207	11	193	17	-0.045	0.057	0.029	0.052
-29.33	241	11	182	16	-0.149	0.054	0.092	0.050
-36.15	271	11	180	12	-0.084	0.046	0.053	0.042
-45.15	274	10	141	9	-0.053	0.041	-0.029	0.028

LOSVD constructed by averaging individual LOSVDs which sample the region at smaller spatial scales. Thus, the average LOSVD contains contributions from LOSVDs as much as $\theta = 11^\circ$ above the major axis.

2.2.2.4 Globular Cluster Kinematics

At large radii, we use individual globular cluster velocities published in Bridges et al. (2007) to derive LOSVDs. The data contain positions and radial velocities for 108 globular clusters in NGC 4594. We discard the innermost 14 GCs as there are too few GCs inside $R \lesssim 130''$ to reconstruct an LOSVD in the inner parts of the galaxy. Assuming axisymmetry, the positions of the GCs are folded about the minor and major axes. In order to preserve rotation, we flip the sign of the velocity for all GCs that are folded about the minor axis. The GCs are then divided into annular bins extending from $\theta = 0^\circ$ to 90° at radii of $131''$, $214''$, $350''$, $574''$, and $941''$ with roughly 20 GCs per bin.

Within each spatial bin, we calculate the LOSVD from the discrete GC velocities by using an adaptive kernel density estimate adapted from Silverman (1986) and explained in Gebhardt et al. (1996). Each LOSVD contains 15 velocity bins. The velocity bins are highly correlated for the GCs, and there are likely only a few degrees of freedom per LOSVD. The 1-σ uncertainties in the LOSVDs are estimated through bootstrap resamplings of the data (Gebhardt et al., 1996; Gebhardt & Thomas, 2009).

We compute Gauss-Hermite moments from the GC LOSVDs—again for plotting purposes only—and show these in Figure 3.2. Uncertainties are calculated

by fitting moments to each resampling of the LOSVD during the bootstrap. The GC kinematics resemble the minor axis stellar kinematics in many of the panels. For example, their dispersions appear to be an extrapolation of the minor axis velocity dispersions. There is slight rotation (small h_3) and possible evidence of radial anisotropy (positive h_4).

2.3 Dynamical Models

The dynamical models rely on the orbit superposition technique first developed by Schwarzschild (1979). We assume axisymmetry and match the luminosity density profile and kinematics of the galaxy to those reconstructed from an orbit library. The library is populated with orbits carefully chosen to sample E, L_z, and the third, non-classical integral I_3.

The code used in this paper is described in Gebhardt et al. (2000a, 2003), Thomas et al. (2004, 2005), and Siopis et al. (2009). Similar axisymmetric codes are presented in Rix et al. (1997), van der Marel et al. (1998), Cretton et al. (1999), and Valluri et al. (2004). Van den Bosch et al. (2008) present a fully triaxial Schwarzschild code. The basic outline of our code is as follows: (*i.*) convert the luminosity density distribution $\nu(r)$ into the stellar density $\rho(r)$ via an assumed stellar mass-to-light ratio M/L_I. (*ii.*) Add to this density the contribution from a black hole of mass $M_\bullet$ and a dark matter halo with density profile $\rho_{DM}(r)$. (*iii.*) Calculate the potential Φ associated with this density distribution and integrate a large number of orbits (typically $\sim$ 20,000) over many dynamical times. (*iv.*) Assign a weight w_i to each orbit and determine the w_i values by minimizing the χ^2 difference between the

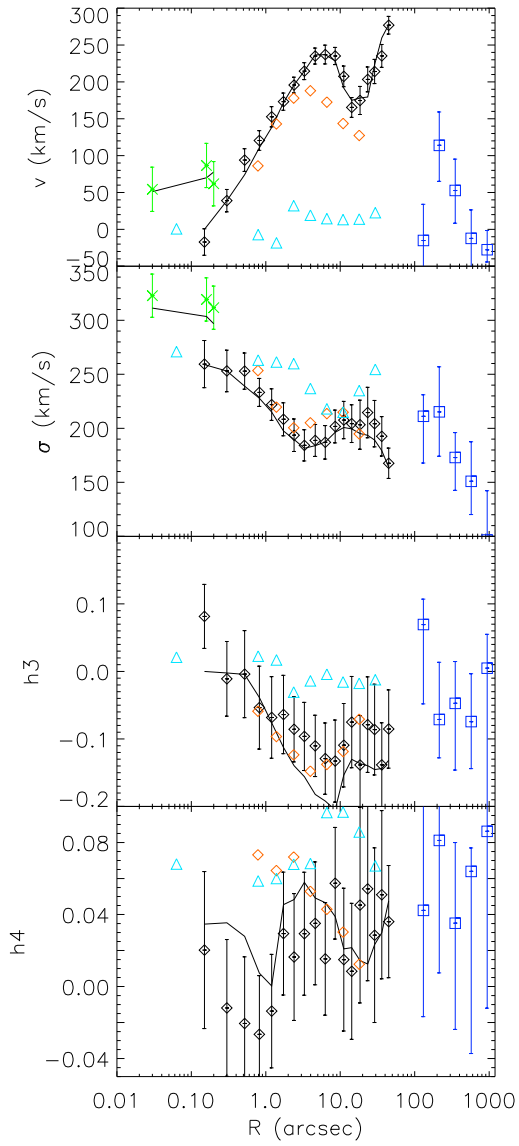

Figure 2.3 Gauss-Hermite moments for NGC 4594 from various sources. Black diamonds with error bars are from Gemini long-slit observations along the major axis. Red diamonds are from SAURON data near the major axis. Light blue triangles are SAURON data near the minor axis. Green crosses are the 3 *HST* data points, and dark blue squares are from the globular clusters. Solid lines are the result of our best fit model.

observed kinematics and luminosity density of the galaxy and those resulting from the PSF-convolved orbit library, subject also to the constraint of maximum entropy.

We maximize the entropy-like quantity $\hat{S} \equiv S - \alpha\chi^2$ where S is the Boltzmann entropy and α controls the relative weight of S or χ^2. For small values of α, reproducing the observed kinematics becomes unimportant, and the models act to only maximize entropy. As α increases, maximizing entropy becomes less important, and more weight is given to matching the observations. In practice, we start with a small value of α and gradually increase it until χ^2 asymptotes. The interested reader may see Siopis et al. (2009) or Shen & Gebhardt (2010) for more details.

Our model grid consists of 19 radial and 5 azimuthal bins covering a radial range of 0.″03 to 1800″spaced logarithmically. Additionally, we use 15 velocity bins to describe our LOSVDs. We incorporate the effects of seeing by convolving the light distribution for each orbit with a model PSF before comparing with data (Gebhardt et al., 2000a). We approximate the PSF as Gaussian with a FWHM of either 0.″94, 0.″5 or 0.″09 depending on whether the data are from SAURON, Gemini, or *HST* observations respectively. The convolution extends to a radius of $10 \times$ FWHM.

We run over 8,500 models with different values of the model parameters M/L_I, $M_\bullet$, and ρ_{DM}. We use $\Delta\chi^2$ statistics to determine the best fit parameter values and their uncertainties. Models whose values of χ^2 are within $\Delta\chi^2 = 1$ of the minimum for a given model parameter (marginalized over the others) define the 1-σ or 68% confidence band of that parameter.

2.3.1 Model Assumptions

Our fiducial density profile is a combination of stellar mass, dark matter, and a central SMBH:

$$\rho(r,\theta) = \frac{M}{L}\nu(r,\theta) + \rho_{DM}(r,\theta) + M_{\bullet}\delta(r) \tag{2.2}$$

where M/L_I is the stellar mass-to-light ratio, assumed constant with radius and $\delta(r)$ is the Dirac delta function. The angle θ is the angle above the major axis. While ρ_{DM} can in principle be a function of θ, we do not consider flattened models. We assume a spherically symmetric, logarithmic halo of the form:

$$\rho_{DM}(r) = \frac{V_c^2}{4\pi G}\frac{3r_c^2 + r^2}{(r_c^2 + r^2)^2} \tag{2.3}$$

This profile is cored for radii $r \lesssim r_c$ and produces a flat rotation curve with circular speed V_c for $r \gg r_c$. It has two free parameters, r_c and V_c, which are varied in the fitting process. Including M/L_I and $M_{\bullet}$, this brings the total number of model parameters to four.

Recently, Gebhardt & Thomas (2009) have shown that the inclusion of a dark matter halo can significantly affect modeled BH masses. To test for this, we run a smaller suite of models without a dark halo.

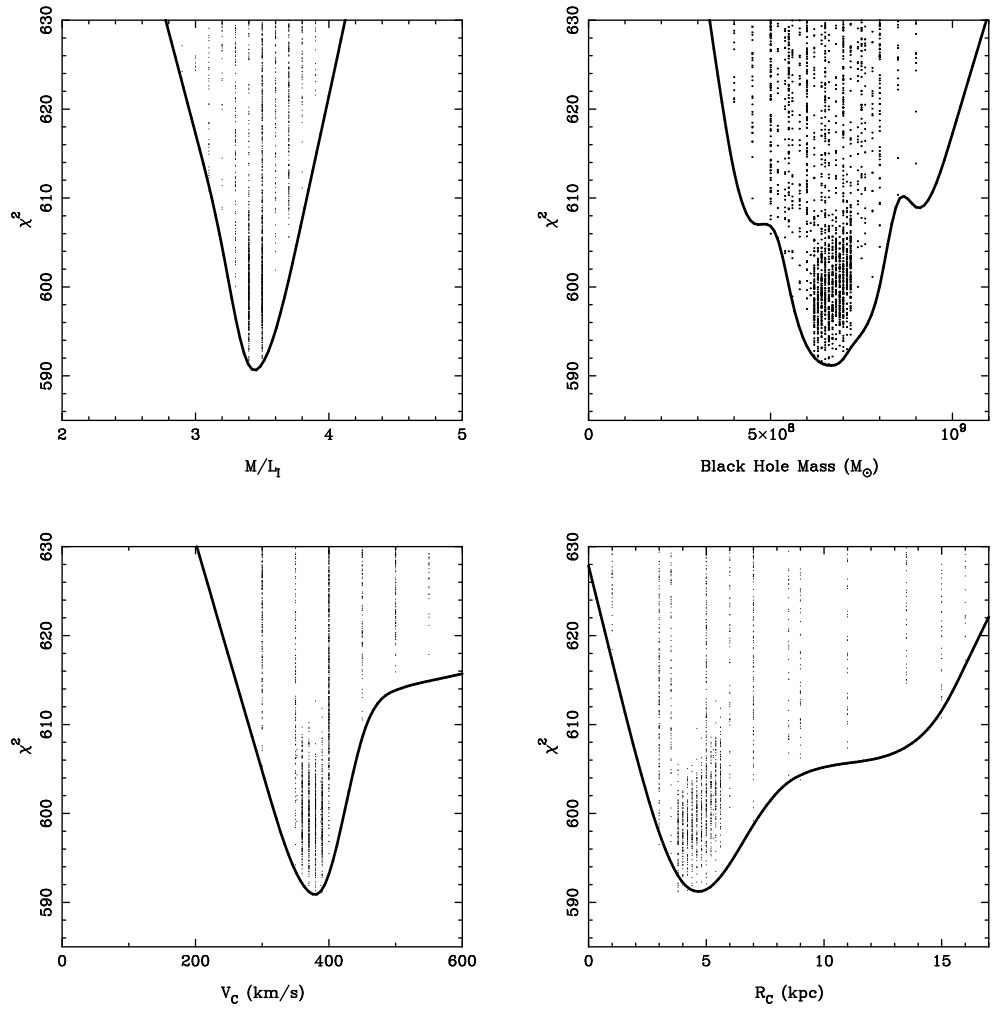

Figure 2.4 χ^2 as a function of the four modeled parameters—M/L_I, $M_\bullet$, V_c, and r_c. Every dot represents a single model. The solid line is a smoothed fit to the minimum, which represents the marginalized values.

2.4 Results

Our best-fit values for the four model parameters are $M/L_I = 3.4 \pm 0.05 \frac{M_\odot}{L_\odot}$, $M_\bullet = (6.6 \pm 0.4) \times 10^8 M_\odot$, $V_c = 376 \pm 12$ km s $^{-1}$, and $r_c = 4.7 \pm 0.6$ kpc. Figure 2.4 shows the χ^2 minima around each of the model parameters. Each dot represents a single model and the solid curve is a smoothed fit to the minimum. The points of the solid curve at $\Delta\chi 2 = 1$ above the minimum determine the 1-σ confidence limits on the parameters. All four model parameters have well-behaved χ^2 curves with sharp, well-defined minima. This allows robust determination of the model parameters with small 1-σ uncertainties.

The uncertainties we present are derived strictly from $\Delta\chi^2$ statistics. The 1-σ error bars on quoted parameters correspond to models within $\Delta\chi^2 = 1$ of the minimum value. Systematic effects are likely to contribute in addition to this quoted uncertainty. While in general for other galaxies one of the biggest sources of systematic uncertainty is inclination, for NGC 4594 inclination uncertainties are unimportant. Other sources of uncertainty may include effects due to non-axisymmetries, but these are likely small or zero since only the most massive ellipticals are thought to be significantly triaxial (Binney, 1978; Kormendy & Illingworth, 1982; Tremblay & Merritt, 1996). For more on systematic uncertainties, the reader is referred to Gebhardt et al. (2003) and Gültekin et al. (2009a,b).

Figure 2.5 shows correlations among the four model parameters. Plotted are the different projections of the four dimensional parameter space; every small dot corresponds to a model run. Red dots are models that lie within $\Delta\chi^2 = 4$ of the minimum, and large black dots are within $\Delta\chi^2 = 1$. There appears to be a

slight correlation between M/L_I and $M_\bullet$—much less severe than in M87 (Gebhardt & Thomas, 2009). Not surprisingly, the high resolution of our *HST* kinematics is able to break the degeneracy between $M_\bullet$ and M/L_I. We discuss this further below. The dark halo parameters do not show any obvious correlation, indicating the GC and stellar kinematics were able to break the degeneracy usually observed between these two parameters.

Our best fit model has (unreduced) $\chi^2 = 582.6$. It is non-trivial to calculate the number of degrees of freedom ν_{DOF}. Roughly, $\nu_{DOF} = N_{LOSVD} \times N_{bin}$, however there are complicated correlations between velocity bins (Gebhardt et al., 2003). With this crude estimate for ν_{DOF}, our best fit model has reduced $\chi^2_\nu = 0.6$.

We compare the modeled value of our stellar mass-to-light ratio with that obtained from evolutionary population synthesis models (Maraston, 1998, 2005). We adopt values of 10 Gyr and 0.1 for the stellar age and metallicity of NGC 4594 (Sánchez-Blázquez et al., 2006) and use these to derive the predicted I-band M/L_I from the Maraston models. For a Salpeter IMF with stellar masses drawn from the range $0.1 - 100 M_\odot$, this analysis yields $M/L_I = 3.99$. If instead the stars obey a Kroupa IMF drawn from the same range, then $M/L_I = 2.58$. We multiply these by a factor of 1.096 corresponding to $A_I = 0.099$ to correct for Galactic extinction along the line of sight (Schlegel et al., 1998) to obtain $M/L_I = 2.83$ and $M/L_I = 4.37$. Our dynamically-derived stellar $M/L_I = 3.4 \pm 0.05$ falls nicely between these two values.

In Figure 2.6, we plot the total mass-to-light ratio as a function of radius for our best fit model with 1-σ uncertainties (gray region). The red cross-hatched re-

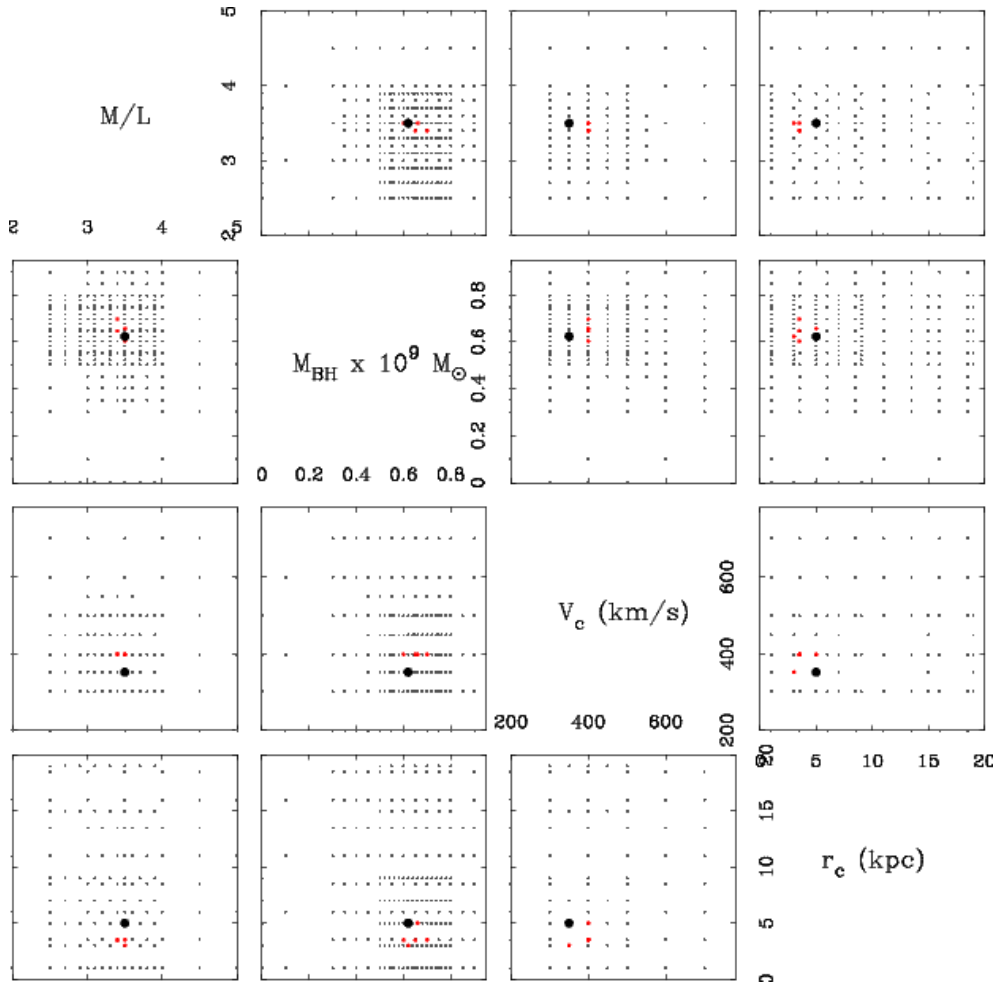

Figure 2.5 Correlation plots among the 4 parameters. Each dot represents a single model. Red dots are within the 95% confidence band and large black dots are within the 68% confidence band for an individual parameter

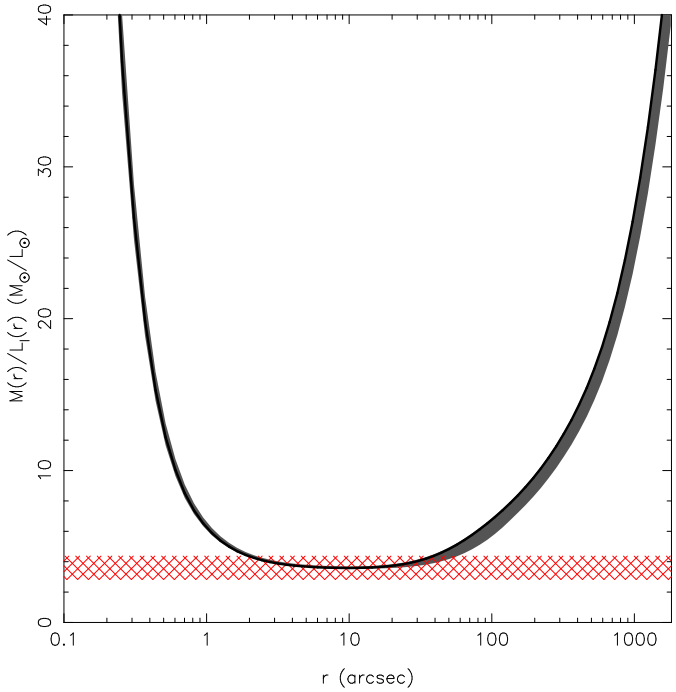

Figure 2.6 Local dynamical mass-to-light ratio for the best fit model. The gray band indicates the 68% confidence band, as determined from the limits placed on the 4 model parameters. The red cross-hatched region indicates the extinction corrected stellar M/L_I derived from population synthesis models.

gion represents the range in stellar M/L_I from stellar population models described above. Total M/L_I rises near the center of the galaxy due to the contribution of the supermassive black hole. As we go out in radius, the stars become more important to the total mass over roughly the range $5''$ to $50''$. Here the total M/L_I approaches both our dynamically determined M/L_I and the range derived from stellar population models. Past $50''$ M/L_I once again rises due to the importance of the dark halo.

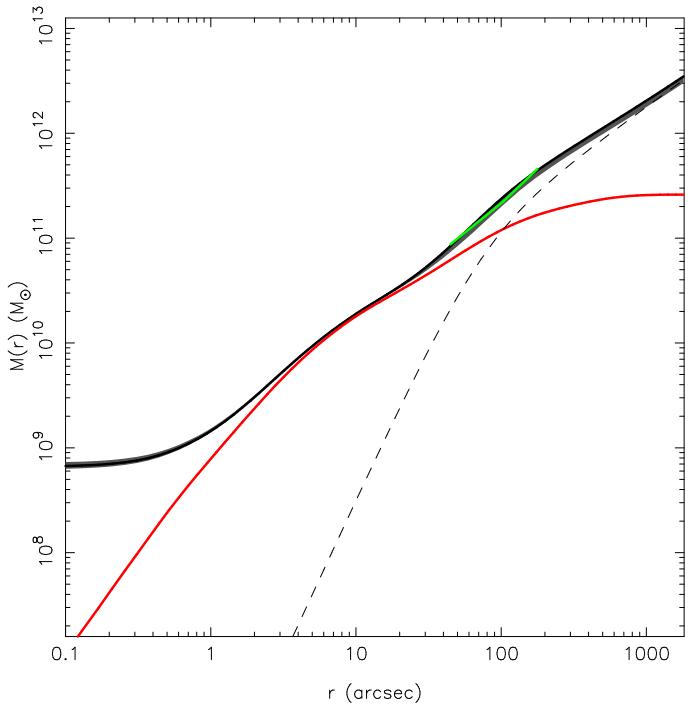

Figure 2.7 Mass enclosed within spherical shells for our best fit model and 68% confidence region. The red line is the stellar mass profile while the black line and surrounding confidence region represent the total mass (black hole + stars + DM). The dashed line is our best-fit dark matter halo. Green indicates the mass profile derived in Kormendy & Westpfahl (1989) from gas rotation.

Figure 4.10 plots the enclosed mass of each component as well as the total mass of the galaxy. At our innermost bin, the total mass is almost two orders of magnitude greater than the stellar mass, meaning we are probing the black hole's sphere of influence quite well. The green line plotted is the mass profile Kormendy & Westpfahl (1989) derive from their gas rotation curve. It agrees well with the total mass distribution derived here.

2.4.1 Models without Dark Matter

We run 189 models with no dark halo. In these models, we exclude the globular cluster data and use only the stellar kinematics. Correspondingly, the number of degrees of freedom impacting the unreduced χ^2 are proportionately fewer. We measure a black hole mass of $M_\bullet = (6.6 \pm 0.3) \times 10^8 M_\odot$ and stellar mass-to-light ratio of $M/L_I = 3.7 \pm 0.05$. The minimum unreduced $\chi^2 = 628$, proving models without a dark halo are a worse fit.

We do not see the dramatic change that Gebhardt & Thomas (2009) see in M87 where the inclusion of a DM halo causes their determination of $M_\bullet$ to double. Instead, our results mirror those of Shen & Gebhardt (2010) in NGC 4649 where the inclusion of a DM halo does not significantly change the modeled $M_\bullet$. The likely explanation for this behavior is the inclusion of high resolution *HST* kinematics in both NGC 4649 and NGC 4594. Schulze & Gebhardt (2011) find the same effect for a larger sample of galaxies. Whenever the data have high enough resolution to resolve the black hole's radius of influence $R_{\rm inf} \sim GM_\bullet/\sigma^2$, dark matter has no significant effect on the determination of $M_\bullet$. For NGC 4594 we measure $R_{\rm inf} \simeq 57$ pc $\simeq 1\farcs2$. We use *HST*/FOS kinematics whose central pointing has a PSF of $0\farcs09 \simeq 0.08 R_{\rm inf}$. Additionally, the light profile of NGC 4594 is more centrally concentrated than that of M87. These factors combine to allow a more accurate determination of $M_\bullet$, removing the freedom that the models have to trade mass between $M_\bullet$ and M/L_I. This is evidenced by the lack of correlation among $M_\bullet$ and M/L_I in Figure 2.5.

2.4.2 Orbit Structure

Having already determined the orbital weights that provide the best fit to the data, we reconstruct the internal unprojected moments of the distribution function. We perform this analysis on our best fit model and the models that define the 68% confidence region (over all combinations of the four model parameters), yielding internal moments at each grid cell.

We define the tangential velocity dispersion to be $\sigma_t \equiv \sqrt{\frac{1}{2}(\sigma_\phi^2 + \sigma_\theta^2)}$ where σ_ϕ is actually the second moment, containing contributions from both streaming and random motion in the ϕ direction. Figure 2.8 shows the radial run of the ratio σ_r/σ_t. The second moment of the DF is tangentially biased where the disk is important (gray region) as expected but mostly is isotropic elsewhere. The red region plots σ_r/σ_t for stars near the minor axis, showing almost perfect isotropy. The green region indicates that at large radii, globular cluster kinematics show significant radial anisotropy. We discuss the implications of this in Section 2.5.2 below.

2.5 Discussion

2.5.1 Black Hole-Bulge Correlations

We discuss the position of NGC 4594 on the M-σ and M-L relations, as defined by Gültekin et al. (2009b, hereafter G09) and compare our values of the correlation parameters to previous measurements. We calculate the effective velocity dispersion σ_e similar to G09.

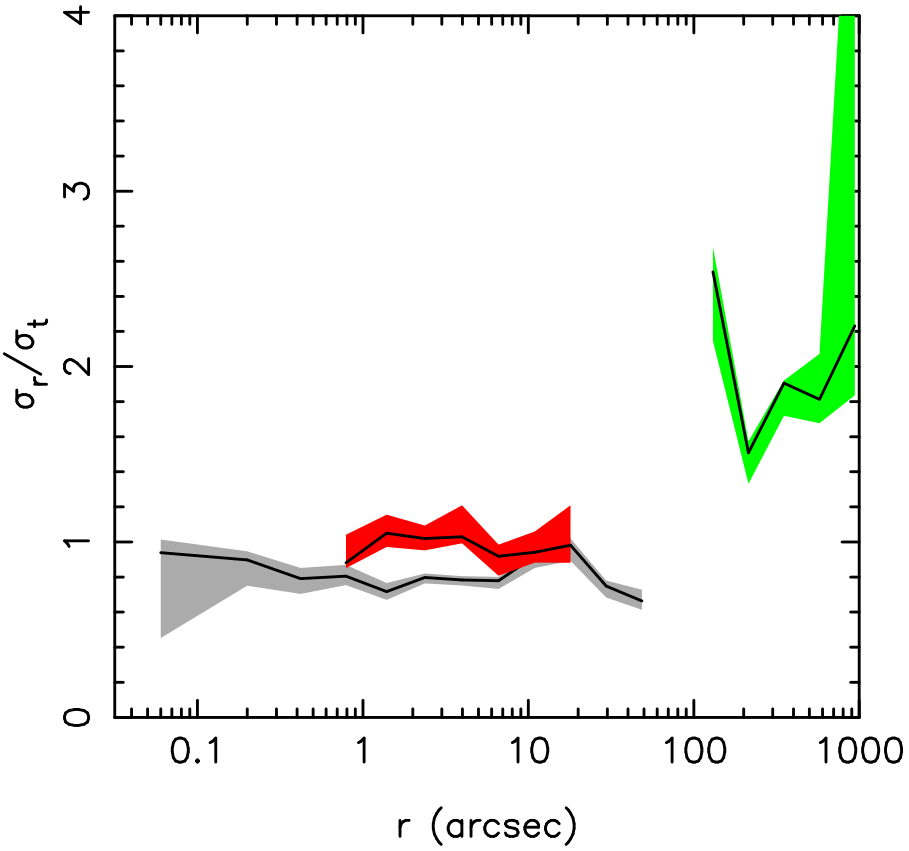

Figure 2.8 Radial run of the ratio of the radial to tangential components of the velocity dispersion tensor. Shaded ares represent 68% confidence regions, with gray indicating stars near the major axis, red meaning stars near the minor axis, and green representing GCs averaged over all angles.

$$\sigma_e^2 \equiv \frac{\int_{R_{\rm inf}}^{R_e} (V^2(R) + \sigma^2(R)) I(R) dR}{\int_{R_{\rm inf}}^{R_e} I(R) dR} \tag{2.4}$$

where $V(R)$ is the rotational velocity and $I(R)$ is the surface brightness profile. This makes σ_e essentially the surface-brightness-weighted second moment. Instead of integrating from the center of the galaxy ($R = 0$) as G09 did, we integrate from $R > R_{\rm inf}$ to ensure that we do not bias σ_e with the high dispersion near the black hole. Our outermost kinematic data point is at $R = 45''$, thus we have a gap in kinematic coverage between $45'' < R < R_e = 114''$. The velocity dispersion near the end of our long-slit data is dropping sharply, however V may still contribute to the integral for $R > 45''$. To investigate this, we use the gas rotation curve presented in Kormendy & Westpfahl (1989) which extends well beyond R_e. Truncating the integral at $R = 45''$ gives $\sigma_e = 292$ km s^{-1} while using the extended rotation curve yields $\sigma_e = 297$ km s^{-1}.

The problem with this definition of σ_e is that it includes a contribution from the rotation of the disk. It has been shown that black hole mass does not correlate with disk properties (Kormendy et al., 2011) so this is not ideal. However, to compare with G09 we must be consistent in our calculation of σ_e. We therefore quote this value of σ_e when we compare to the M-σ relation determined by G09. As we expect black hole mass to track bulge quantities, disk contribution to σ_e is likely to add a source of intrinsic scatter to spiral galaxies in the M-σ relation. In fact, spiral galaxies are observed to have larger scatter about M-σ than ellipticals of similar σ_e.

We also discuss some possible alternatives to σ_e where we attempt to remove

the disk contribution. One option is to remove $V^2(R)$ from Equation (2.4) altogether. Bulges are known to rotate, however, (Kormendy & Illingworth, 1982) and this will likely underestimate σ_e. This crude calculation gives $\sigma_e = 200$ km s^{-1}.

Another option is to assume some degree of bulge rotation a priori. If we assume NGC 4594 rotates isotropically (Kormendy & Illingworth, 1982), then its flattening determines its position on the $V/\sigma - \epsilon$ diagram (Binney, 1978). Kormendy (1982) shows that the relation

$$\frac{V}{\sigma} \approx \sqrt{\frac{\epsilon}{1-\epsilon}} \tag{2.5}$$

approximates the isotropic rotator line to roughly 1% accuracy. We use our value of the bulge ellipticity $\epsilon = 0.25$ in Equation (2.5) and assume this value of V/σ applies globally to the entire bulge. We then use our measured dispersion profile $\sigma(R)$ to determine the bulge velocity $V_{\rm bulge}(R)$. Using these quantities, we determine $\sigma_e =$ 230 km s^{-1}. We compare this to the kinematics listed in Kormendy & Illingworth (1982). These data include long-slit spectra taken at a position angle parallel to the major axis, but 30″, 40″, and 50″ above it. From these data, it is apparent that the bulge σ off the major axis is roughly constant at ~ 220 km s^{-1}. The rotation velocity rises from 0 to 100 km s^{-1} at large radii. We estimate the luminosity-weighted mean $V \sim 50$ km s^{-1}. Adding this in quadrature to the constant bulge $\sigma = 220$ km s^{-1} gives $\sigma_e \approx 226$ km s^{-1}. This estimate does not contain any rotation from the disk, and is consistent with our determination of $\sigma_e = 230$ km s^{-1} obtained by assuming a constant V/σ.

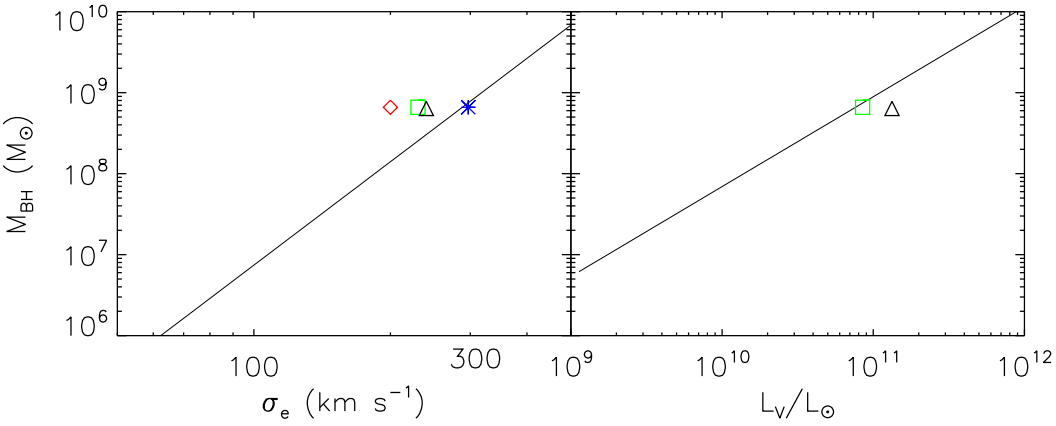

Figure 2.9 Position of NGC 4594 on the G09 M-σ and M-L relations. The plot of M-σ (left) shows the three ways we calculate σ_e as well as the value from G09 (black triangle). In order of increasing σ_e we plot σ_e with no rotation (red diamond), σ_e assuming a value of V/σ (green square) and σ_e as in G09 (blue asterisk). For the M-L relation (right) we plot the G09 value (black triangle) along with our measurement (green square).

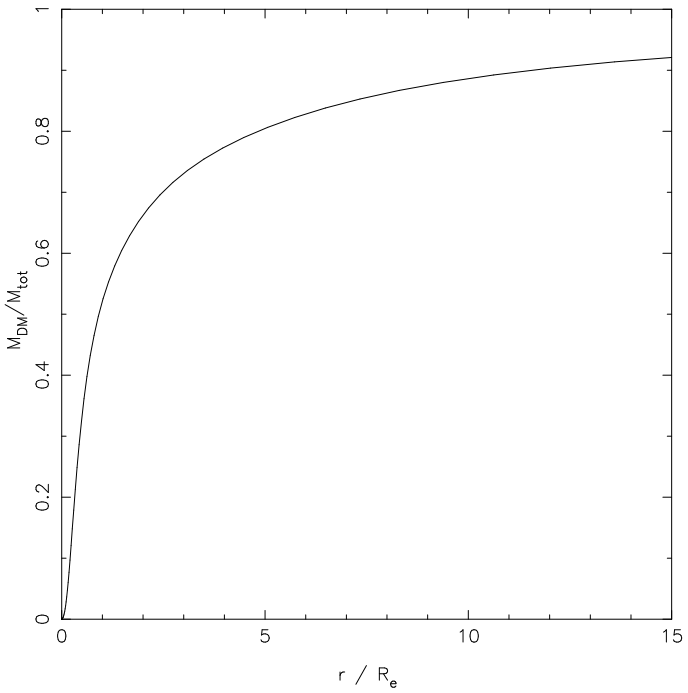

Figure 2.10 Fraction $M_{DM}/(M_\star + M_{DM})$ of enclosed mass that is dark matter as a function of radius.

Our black hole mass $M_\bullet = (6.6 \pm 0.4) \times 10^8 M_\odot$ agrees nicely with that of G09 which uses the K88 value. In fact, when corrected for their various distance determinations, most values of $M_\bullet$ in the literature agree quite well (K88, Emsellem et al. 1994b, K96, Magorrian et al. 1998) despite the many modeling techniques and datasets used. This is likely due to the high degree of isotropy as evidenced in Figure 2.8, deduced from the $V/\sigma - \epsilon$ diagram (Kormendy & Illingworth, 1982), and noted in K88.

Figure 2.9 plots the position of NGC 4594 on the G09 M-σ and M-L relations. We plot each determination of σ_e in the left-hand panel. Straightforward application of Equation (2.5) leads to a value of σ_e that falls directly on the G09 M-σ line (blue asterisk). Next closest is the method of calculating σ_e by assuming a value of V/σ (green square). This point lies 0.44 dex above the G09 line, however this is still within the estimated scatter. The calculation of σ_e that ignored all rotation is, not surprisingly, farthest from the G09 line. Calculation of the relevant quantities for comparison with the M-L relation is straightforward, and we plot our value of $M_\bullet$ and L_V (green square) along with that from G09 in the right-hand panel.

2.5.2 Globular Clusters

As demonstrated in section 2.4.2, we find significant radial anisotropy in the globular clusters. It is interesting that the stellar kinematics at smaller radii do not show this feature. This difference in orbital properties combined with the difference in their light profiles might suggest the GCs and stars are two distinct populations of tracer particles. This could also indicate the two populations have

different formation scenarios.

Unfortunately, there is no radius in the galaxy where we have simultaneous coverage of both stellar and GC kinematics. Thus, we are unable to test whether the stellar orbits become more radial in the $\sim 50''$ between where the stellar kinematics run out and the GCs begin. However, since the light profiles of both populations are significantly different (Figure 2.1) there is no reason to assume they should share similar orbit properties.

Figure 2.8 shows the globular clusters in NGC 4594 are radially anisotropic ($\sigma_r/\sigma_t > 1$) over roughly the radial range 100-1000$''$ (approximately 1-10 R_e). Previous studies of the GC systems of galaxies have found their velocity ellipsoids to be isotropic (Côté et al., 2001, 2003). However, these studies used spherical Jeans modeling instead of the more general axisymmetric Schwarzschild code we use.

Rhode & Zepf (2004) determine with high confidence that the color distribution of the GC system in NGC 4594 is bimodal. This may indicate different subpopulations of GCs with different orbital properties that formed at different epochs in the galaxy's history. In our analysis, we make no distinction between red and blue subpopulations. We use the light profile and kinematics of all available GCs, regardless of color. However, since we use different sources for our kinematics and photometry data, there is the possibility that each source draws from a different GC subpopulation.

2.5.3 Dark Halo

The parameters V_c and r_c of our model dark halo imply a central dark matter density of $\rho_c = 0.35 \pm 0.1 M_\odot$ pc^{-3} Using an improved Jeans modeling technique, Tempel & Tenjes (2006) model NGC 4594 and find a dark matter halo with central density $\rho_c = 0.033 M_\odot$ pc^{-3}, ten times lower than our value. They, however, measure a larger stellar $M/L_{IV} = 7.1 \pm 1.4$ in the bulge.

We plot the fraction of enclosed mass that is dark matter as a function of half-light radius R_e in Figure 2.10. At 1 R_e there is already a roughly 50-50 mix of stars and DM. Inside of R_e the dark matter still contributes a non-negligible fraction to the total mass content.

In a study measuring dark matter properties in 1.7×10^5 local ($z < 0.33$) early-type galaxies from the Sloan Digital Sky Survey, Grillo (2010) find a correlation between the fraction of dark matter within R_e and the logarithmic value of R_e. With our measured value of R_e, this correlation predicts a dark matter fraction at R_e of 0.68. Our value of 0.52 is smaller, but still within their 68% confidence limit.

Thomas et al. (2009) derive scaling relations for halo parameters based on observations of early-type galaxies in the Coma cluster. These relations are constructed for similar galaxies using the same halo parameterization and modeling code used in this paper. This makes comparison to our parameters straightforward. We compare to the observed relations between halo parameters r_c, V_c, and ρ_c and total blue luminosity L_B. Our value of V_c falls directly on the V_c-L_B relation, however our measured r_c is smaller by roughly an order of magnitude. Since $\rho_c \propto V_c^2/r_c^2$, the

discrepancy in r_c causes our measurement of ρ_c to be high when compared to the Thomas et al. (2009) ρ_c-L_B relation. Scatter in this relation is large, however, and the environment of NGC 4594 is different from that of the Coma galaxies.

Kormendy & Freeman (2004, 2011) also derive scaling laws for similar parameters in galaxies of later Hubble type (Sc-Im). We measure a much higher density and much smaller core radius than the Kormendy & Freeman (2004, 2011) relations imply at the L_B of NGC 4594. We interpret this as the result of severe compression of the halo by the gravity of the baryons (Blumenthal et al., 1986). Such an effect is expected in early-type galaxies with massive bulges.

We thank Eric Emsellem for providing reduced SAURON data and helpful comments. This work would not be feasible without the excellent resources of the Texas Advanced Computing Center (TACC). KG acknowledges support from NSF-0908639. DR is grateful for hospitality and support from the Institute for Advanced Study in the form of a Corning Glass Works Foundation Fellowship.

Chapter 3

The Dark Matter Density Profile of the Fornax Dwarf[1]

It cannot be seen, cannot be felt,
Cannot be heard, cannot be smelt.
It lies behind stars and under hills,
And empty holes it fills.

J.R.R. Tolkien - "The Hobbit"

We construct axisymmetric Schwarzschild models to measure the mass profile of the local group dwarf galaxy Fornax. These models require no assumptions to be made about the orbital anisotropy of the stars, as is the case for commonly used Jeans models. We test a variety of parameterizations of dark matter density profiles and find cored models with uniform density $\rho_c = (1.6 \pm 0.1) \times 10^{-2} M_\odot$ pc^{-3} fit significantly better than the cuspy halos predicted by cold dark matter simulations. We also construct models with an intermediate-mass black hole, but are unable to make a detection. We place a 1-σ upper limit on the mass of a potential intermediate-mass black hole at $M_\bullet \leq 3.2 \times 10^4 M_\odot$.

[1]Published in Jardel, J. R., & Gebhardt, K., 2012, ApJ, 746, 89. Reprinted with permission from the American Astronomical Society.

3.1 Introduction

Low-mass galaxies provide a unique testing ground for predictions of the cold dark matter (CDM) paradigm for structure formation, since they generally have a lower fraction of baryons than massive galaxies. These galaxies allow for a more direct measurement of the underlying dark matter potential, as the complicated effects of baryons on the dark matter are less pronounced. A particularly testable prediction of CDM is that all galaxies share a universal dark matter density profile, characterized by a cuspy inner power law $\rho \propto r^{-\alpha}$ where $\alpha = 1$ (Navarro et al. 1996b, hereafter NFW). Many authors have investigated low-mass spirals and found, in contrast to the predictions of CDM, dark matter density profiles with a flat inner core of slope $\alpha = 0$ (Burkert, 1995; Persic et al., 1996; de Blok et al., 2001; Blais-Ouellette et al., 2001; Simon et al., 2005). This has launched the debate known as the core/cusp controversy.

A number of other studies have investigated the mass content of dwarf spheroidal galaxies (dSphs). Gilmore et al. (2007) give a comprehensive review of recent attempts to constrain the inner slope of their dark matter profiles with Jeans modeling (Jeans 1919; Binney & Tremaine 1987, chapter 4). When significant, cored profiles are preferred for all dSphs modeled (Gilmore et al. 2007, and references therein).

These results, however, are subject to a major caveat of Jeans modeling; it is complicated by the effect of stellar velocity anisotropy. Models fit to the line-of-sight component of the velocity dispersion, but anisotropy can severely affect the modeling of enclosed mass. Therefore, additional assumptions must be made. The

studies presented in Gilmore et al. (2007) assume spherical symmetry and isotropy. Evans et al. (2009) show that a weakness of Jeans modeling is that given these assumptions combined with the cored light profiles observed in dSphs, the Jeans equations do not allow solutions with anything other than a cored dark matter profile.

Walker et al. (2009b) construct more sophisticated models and attempt to parameterize and fit for the anisotropy. As a result, preference for cored profiles becomes model-dependent. They therefore are unable to put significant constraints on the slope of the dark matter profile. This highlights the main problem with Jeans modeling—it is highly dependent on the assumptions made.

Distribution function models can be made more general than Jeans models, and progress has been made applying them to a number of dSph systems (Kleyna et al., 2002; Wu, 2007; Amorisco & Evans, 2011b). Nevertheless these models still make strong assumptions such as spherical symmetry or isotropy, and models that do fit for anisotropy do so without using the information about the stellar orbits contained in the line-of-sight velocity distributions (LOSVDs).

We employ a fundamentally different modeling technique, known as orbit-based (or Schwarzschild) modeling, that allows us to use this information to self-consistently calculate both the enclosed mass and orbital anisotropy. Schwarzschild modeling is a mature industry, but one that has seldom been applied to the study of dSph galaxies (see Valluri et al. 2005).

In addition to being well-suited for measuring dark matter profiles, Schwarzs-

child modeling has often been used to search for black holes at the centers of galaxies. Another unresolved issue relevant to the study of dSphs is whether they host an intermediate-mass black hole (IMBH). In a hierarchical merging scenario, smaller galaxies are thought to be the building blocks of larger galaxies. It is thought that all massive galaxies host a supermassive black hole (SMBH) at their center, therefore it is logical to believe that their building blocks host smaller IMBHs. Evidence for these IMBHs is scarce, however, and dynamical detections are even scarcer. The closest and lowest mass example of a dynamical measurement is an upper limit on the local group dSph NGC 205 of $M_\bullet \leq 2.2 \times 10^4 M_\odot$ (Valluri et al., 2005). Black holes in this mass range can provide constraints on theories of black hole growth and formation. The two most prominent competing theories of nuclear black hole formation are direct collapse of primordial gas (Umemura et al., 1993; Eisenstein & Loeb, 1995; Begelman et al., 2006) or accretion onto and mergers of seed black holes resulting from the collapse of the first stars (Volonteri & Perna, 2005).

In this paper we present axisymmetric, three-integral Schwarzschild models in an effort to determine the inner slope of the dark matter density profile as well as the orbit structure of the Fornax dSph. We also investigate the possibility of a central IMBH. We assume a distance of 135 kpc to Fornax (Bersier, 2000).

3.2 Data

To construct dynamical models, we require a stellar light profile as well as stellar kinematics in the form of LOSVDs. We use published data for both the photometry and kinematics, and describe the steps taken to convert this data into

useful input for our models.

3.2.1 Stellar Density

To determine the stellar density, we use a number density profile from Coleman et al. (2005) extending to 4590″. We linearly extrapolate the profile out to 6000″—a physical radius of 3.9 kpc at our assumed distance. We also extrapolate the profile inwards at constant density from 90″ to 1″.

To convert to a more familiar surface brightness profile we apply an arbitrary zero-point shift in log space, adjusting this number so that the integrated profile returns a luminosity consistent with the value listed in Mateo (1998). Adopting an ellipticity of $e = 0.3$ (Mateo, 1998), we deproject under the assumption that surfaces of constant luminosity are coaxial spheroids (Gebhardt et al., 1996), and for an assumed inclination of $i = 90°$.

3.2.2 Stellar Kinematics

We derive LOSVDs from individual stellar velocities published in Walker et al. (2009a). The data contain heliocentric radial velocities and uncertainties with a membership probability for 2,633 Fornax stars. Most of these are single-epoch observations, however some are multi-epoch. Stars that have more than one observation are averaged, weighted by their uncertainties. After making a cut in membership probability at 90%, we are left with 2,244 stars. Although a significant number of stars observed may be in binary or multiple systems, simulations have shown that such systems are unlikely to affect measured dispersions (Hargreaves et al., 1996;

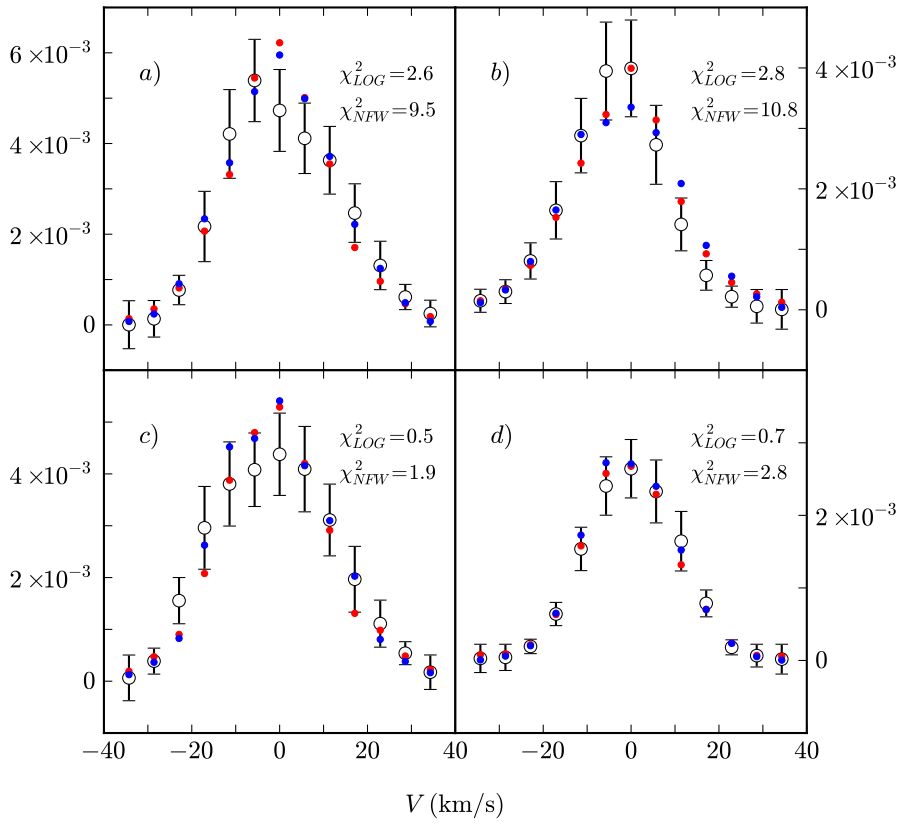

Figure 3.1 Line-of-sight velocity distributions of four bins. Open circles with error bars are the data. Over-plotted are the model values for the best-fitting cored model (red) and NFW model (blue). Bins are located at: (a) $R = 297''$, $\theta = 18°$ (b) $R = 550''$, $\theta = 18°$ (c) $R = 1008''$, $\theta = 45°$ (d) $R = 2484''$, $\theta = 45°$. Quoted χ^2 values are unreduced.

Olszewski et al., 1996; Mateo, 1998).

We adopt a position angle $PA = 41^\circ$ (Walker et al., 2006). We assume symmetry with respect to both the major and minor axes and fold the data along each axis. To preserve any possible rotation, we switch the sign of the velocity whenever a star is flipped about the minor axis.

The transverse motion of Fornax contributes a non-negligible line-of-sight velocity to stars, particularly those at large galactocentric radius. Using the equations in Appendix A of Walker et al. (2008), we correct for this effect. We adopt values for the proper motion of $(\mu_\alpha, \mu_\delta) = (47.6, -36.0)$ mas century^{-1} (Piatek et al., 2007) and assume the heliocentric radial velocity of Fornax is 53.3 km s^{-1} (Piatek et al., 2002).

We divide our meridional grid into 20 radial bins, equally spaced in approximately log r from $1''$to $5000''$. There are 5 angular bins spaced equally in $\sin\theta$ over 90° from the major to the minor axis (Gebhardt et al., 2000a; Siopis et al., 2009). From the positions of the folded stellar velocity data, we determine the best binning scheme so that each grid cell contains at least 25 stars from which to recover the LOSVD. Our first bin with enough stars to meet this criterion is centered at $47''$, and the last bin is centered at $2500''$. We therefore have two-dimensional kinematics coverage over the radial range $47''$-$2500''$(30pc - 1.6 kpc). At small radii the number density of stars with velocity measurements is low, thus our central LOSVDs have higher uncertainty compared to those at larger radii.

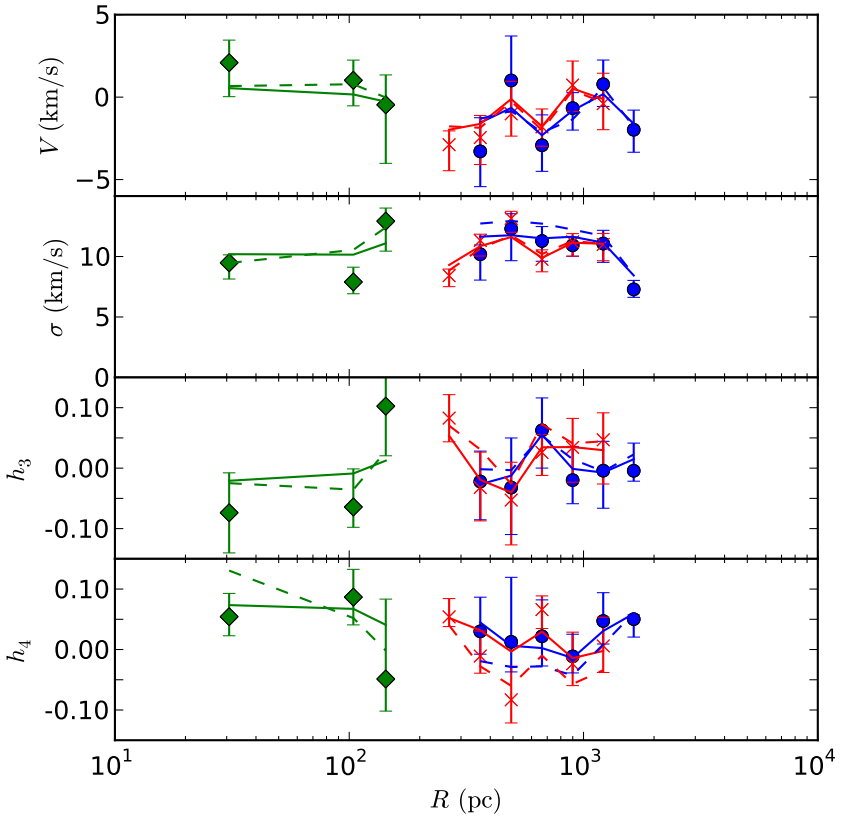

Figure 3.2 Gauss-Hermite moments for stars near the major axis (blue), minor axis (red), and averaged over all angles (green). Solid lines correspond to the best-fit model with a cored dark matter halo, dashed lines are for the best-fit model with a NFW halo.

Table 3.1. Best-Fit Model Parameters

DM Profile	χ^2	$\frac{M}{L_V}$	c	r_s (kpc)	ρ_c ($M_\odot pc^{-3}$)	$M_\bullet(M_\odot)$	N_{model}
NFW	239.8	1.3 ± 0.6	4.1 ± 0.26	11.7 ± 1.4	—	—	3124
Log	162.6	1.5 ± 0.5	—	—	$1.6 \pm 0.1 \times 10^{-2}$	—	4319
Log	162.6	1.6 ± 0.2	—	—	$1.6 \pm 0.1 \times 10^{-2}$	$\leq 3.2 \times 10^4$	3423

Note. — Best-fit parameters for NFW, and cored logarithmic dark matter halos. χ^2 is un-reduced, the number of degrees of freedom are the same for each model. Model parameters and 1-σ uncertainties are quoted. N_{model} lists the number of models run for the corresponding parameterization.

Within each grid cell, we calculate the LOSVD from discrete stellar velocities by using an adaptive kernel density estimate adapted from Silverman (1986) and explained in Gebhardt et al. (1996). We estimate the $1-\sigma$ uncertainties in the LOSVDs through bootstrap resamplings of the data (Gebhardt et al., 1996; Gebhardt & Thomas, 2009). The bootstrap generates a new sample from the data itself by randomly picking N data points, where N is the total number of stars in a given bin, allowing the same point to be chosen more than once. We then estimate the LOSVD from that realization and repeat the procedure 300 times. The 68% confidence band on the LOSVDs corresponds to the 68% range of the realizations. We compare the velocity dispersion as measured by the LOSVDs with the biweight scale (i.e., a robust estimate of the standard deviation, see Beers et al. 1990) of the individual velocities and note good agreement.

Figure 4.3 plots the LOSVDs of four bins. Rather than parameterizing these LOSVDs with Gauss-Hermite moments, our models instead fit directly to the LOSVDs to constrain the kinematics of the galaxy. However, we do fit Gauss-Hermite moments for plotting purposes only. These data are presented in Figure 3.2 for stars that have been grouped into bins near the major axis (blue) and minor axis (red). Near the center of the galaxy the density of stars with kinematics is sparse, so we therefore group stars into annular bins covering all angles (green). We estimate the 1-σ uncertainties of the Gauss-Hermite moments by fitting to each of the 300 realizations calculated during the bootstrap discussed above. The error bars plotted contain 68% of the 300 realizations.

3.3 Dynamical Models

The modeling code we use is described in detail in Gebhardt et al. (2003), Thomas et al. (2004, 2005), and Siopis et al. (2009) and is based on the technique of orbit superposition (Schwarzschild, 1979). Similar axisymmetric codes are described in Rix et al. (1997); van der Marel et al. (1998); Cretton et al. (1999); Valluri et al. (2004) while van den Bosch et al. (2008) present a fully triaxial Schwarzschild code. Our code begins by choosing a trial potential that is a combination of the stellar density, dark matter density, and possibly a central black hole. We then launch $\sim 15,000$ orbits carefully chosen to uniformly sample the isolating integrals of motion. In an axisymmetric potential, orbits are restricted by three isolating integrals of motion, E, L_z, and the non-classical "third integral" I_3. As it is not possible to calculate I_3 a priori, we use a carefully designed scheme to systematically sample I_3 for each pair of E and L_z (Thomas et al., 2004; Siopis et al., 2009). Orbits are integrated for many dynamical times, and each orbit is given a weight w_i. We find the combination of w_i that best reproduces the observed LOSVDs and light profile via a χ^2 minimization subject to the constraint of maximum entropy (Siopis et al., 2009).

We run models by varying 3 parameters—the stellar M/L_I and two parameters specifying the dark matter density profile. Some models are also run with a central black hole whose mass is varied in addition to the other 3 model parameters. Each model is assigned a value of χ^2 and we identify the best-fitting model as that with the lowest χ^2. We determine the 68% confidence range on parameters by identifying the portion of their marginalized χ^2 curves that lie within $\Delta\chi^2 = 1$ of

the overall minimum.

3.3.1 Model Assumptions

Our trial potential is determined by solving Poisson's equation for an assumed trial density distribution. On our two-dimensional polar grid, this takes the form:

$$\rho(r,\theta) = \frac{M}{L}\nu(r,\theta) + \rho_{DM}(r) \tag{3.1}$$

where M/L is the stellar mass-to-light ratio, assumed constant with radius, and $\nu(r,\theta)$ is the unprojected luminosity density. The assumed dark matter profile $\rho_{DM}(r)$ is discussed below. For simplicity, we assume Fornax is edge-on in all our models.

3.3.2 Dark Matter Density Profiles

We parameterize the dark matter halo density with a number of spherical density profiles. We use NFW halos:

$$\rho_{DM}(r) = \frac{200}{3}\frac{A(c)\rho_{crit}}{(r/r_s)(1+r/r_s)^2} \tag{3.2}$$

where

$$A(c) = \frac{c^3}{\ln(1+c) - c/(1+c)}$$

and ρ_{crit} is the present critical density for a closed universe. The two parameters we fit for are the concentration c and scale radius r_s. We also use halos derived from the logarithmic potential:

$$\rho_{DM}(r) = \frac{V_c^2}{4\pi G}\frac{3r_c^2 + r^2}{(r_c^2 + r^2)^2} \tag{3.3}$$

These models feature a flat central core of density $\rho_c = 3V_c^2/4\pi G r_c^2$ for $r \lesssim r_c$ and an r^{-2} profile for $r > r_c$. We fit for V_c and r_c, the asymptotic circular speed at $r = \infty$ and core radius respectively. We run over 10,000 models with only three distinct parameterizations: NFW halos, and logarithmic models with and without an IMBH.

3.4 Results

We find significant evidence for cored logarithmic dark matter density profiles. These models are preferred at the $\Delta\chi^2 = 77$ level when compared to models with an NFW halo, a highly significant result. Perhaps more convincingly, the values for the concentration preferred by our models are around $c = 4$. Only relatively recently formed structures like galaxy clusters are expected to have concentrations this low (NFW).

Table 3.1 summarizes the results of our models, while Figures 4.3 and 3.2 illustrate the preference for cored models over models with an NFW halo in fitting to the kinematics. We stress again that LOSVDs like those plotted in Figure 4.3 are the kinematic constraint, and not the Gauss-Hermite moments of Figure 3.2.

While we fit for V_c and r_c in the cored models, these parameters are strongly degenerate. Our model grid extends to 3.3 kpc, thus any model with $r_c > 3.3$ kpc has a uniform density $\rho_c = 3V_c^2/4\pi G r_c^2$ over the entire range of our model. Furthermore, we have no velocity information from stars past $R \geq 1.6$ kpc and therefore cannot

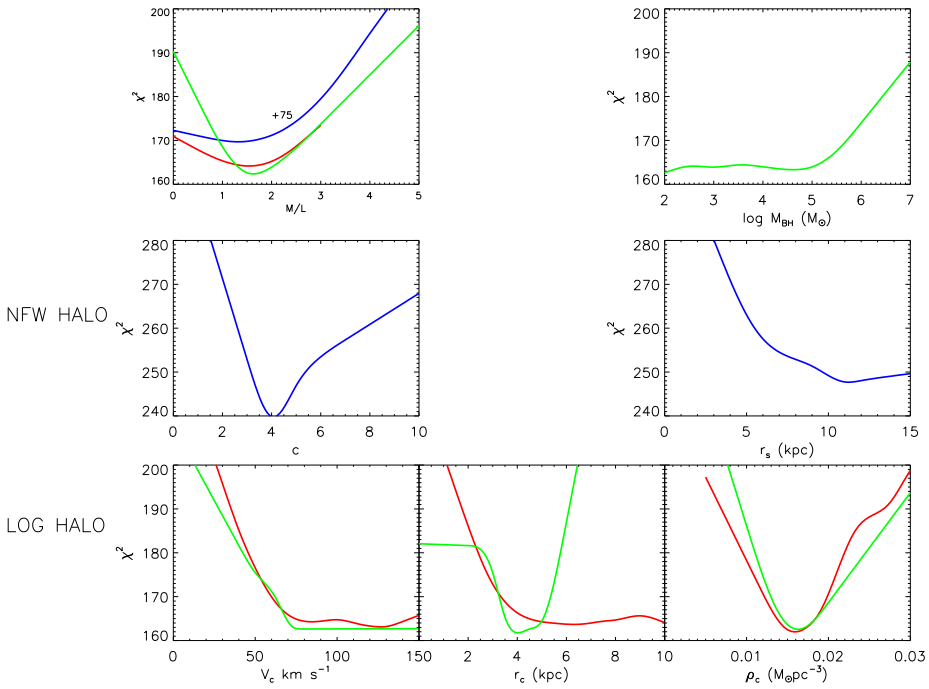

Figure 3.3 χ^2 curves for all parameterizations of the mass profile. NFW halos (blue) are parameterized by concentration c and scale radius r_s. Logarithmic halos with an IMBH (green) and without (red) are specified by V_c and r_c. We also plot core density $\rho_c = 3V_c^2/4\pi G r_c^2$ as it is the controlling parameter over the radial range of our models. We fit for stellar M/L_I in all models (upper left panel). NFW models have much higher χ^2 and are scaled down by 75 to fit on the same axis. Black hole mass for logarithmic halos with an IMBH (green) is plotted in the upper right panel. Note the apparent minimum in r_c for logarithmic halos with an IMBH is due to incomplete parameter sampling.

constrain the kinematics in the outer parts of the galaxy. Thus, for models with $r_c \gtrsim 1.6$ kpc, ρ_c is now the only parameter that differentiates between models. As ρ_c is dependent on both V_c and r_c, the latter two parameters are completely degenerate.

Figure 3.3 illustrates this effect. Plotted are the χ^2 curves for each model parameter. Lines of the same color indicate a common parameterization of the mass profile (e.g. cored + IMBH). While the χ^2 for both V_c and r_c asymptotes to large values, ρ_c is tightly constrained. Note that the behavior of r_c for logarithmic profiles with an IMBH (green line) is a result of incomplete parameter sampling. With a more densely-sampled parameter space, the χ^2 curve for r_c for cored models with an IMBH would likely asymptote to large r_c in a similar fashion as models without an IMBH (red curve).

The addition of a central black hole to the mass profile does not make a noticeable difference to the overall χ^2 for most values of $M_\bullet$. We therefore place a 1-σ upper limit on $M_\bullet \leq 3.2 \times 10^4 M_\odot$.

We plot the mass profile for our best-fit model in Figure 3.4 (solid black line with surrounding 68% confidence region). This is a cored logarithmic dark matter profile without a central black hole. The mass profile of our best-fit dark halo is plotted as the dashed line, and the stellar mass profile is plotted in red. The contribution of dark matter to the total mass increases with radius as the local dynamical mass-to-light ratio rises from approximately ~ 2 to greater than 100 in the outermost bin of our model.

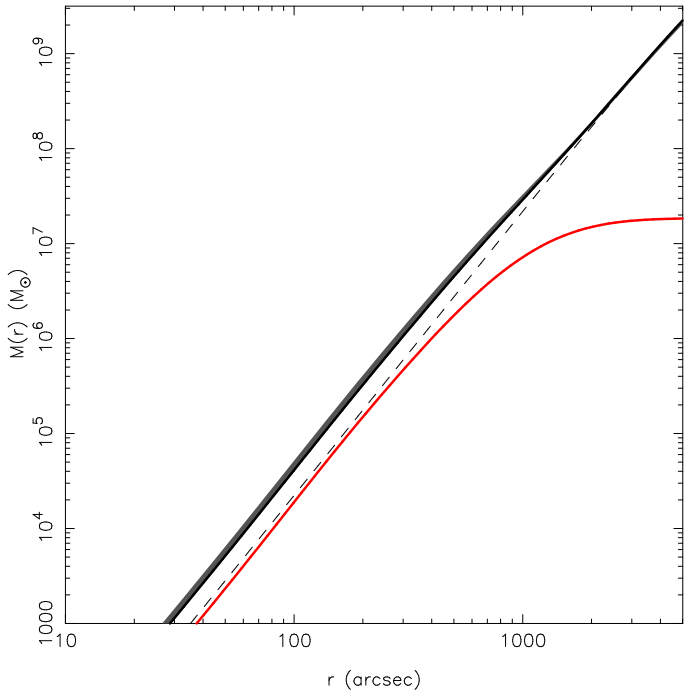

Figure 3.4 Total enclosed mass for our best-fit model (black line with surrounding confidence region). Red line is the enclosed stellar mass. Dashed line is our best-fit dark matter halo.

3.4.1 Orbit Structure

We construct a distribution function for the galaxy from the set of orbital weights w_i resulting from the χ^2 minimization of our best-fit model. To explore the orbit structure, we determine the internal (unprojected) moments of the distribution function in spherical coordinates. Streaming motions in the $\mathbf{r}$ and $\boldsymbol{\theta}$ directions are assumed to be zero. In this coordinate system, cross-terms of the velocity dispersion tensor are zero.

Figure 6.5 plots the anisotropy in the diagonal components of the dispersion tensor. While some panels show an average value near unity, there are regions in

every panel where the ratio plotted is different from one. Additionally, we define the tangential velocity dispersion $\sigma_t \equiv \sqrt{\frac{1}{2}(\langle v_\phi^2 \rangle + \sigma_\theta^2)}$ where $\langle v_\phi^2 \rangle$ is the second moment $\langle v_\phi^2 \rangle = \sigma_\phi^2 + V_\phi^2$, and V_ϕ^2 is the mean rotation velocity. With this definition, we plot the ratio σ_r/σ_t in the bottom panels of Figure 6.5 to investigate whether orbits are radially or tangentially biased. From these plots it is clear that the common assumptions of Jeans modeling—constant or zero anisotropy—are unrealistic. We find that at most radii in the galaxy, orbits are radially biased. The uncertainty in the anisotropy is largest at small radii, as evidenced by the size of the 68% confidence regions in Figure 6.5. This is likely due to the sparsity of kinematics in the inner part of the galaxy (there are limits to how closely target fibers can be spaced in multi-fiber spectroscopy).

In a recent paper, Kazantzidis et al. (2011) simulated the effects of tidal stirring on a number of dSph progenitors around a Milky Way sized halo. They found radial anisotropy in all of the final remnants, and our models are consistent with these findings.

3.5 Discussion

3.5.1 Cores and Cusps

Our analysis shows that for the Fornax dwarf an NFW dark matter halo with inner slope $\alpha = 1$ is rejected with high confidence. We have kinematics from 30 pc-1.6 kpc, and over this range the models prefer an $\alpha = 0$ uniform density core with $\rho_c = 1.6 \times 10^{-2} M_\odot \, \mathrm{pc}^{-3}$. We do not attempt to fit for models with an intermediate value of the slope $0 \leq \alpha \leq 1$. Further investigation is necessary before we can

conclude that the best fitting dark matter profile is the logarithmic model. The steep $\alpha = 1$ cusp of the NFW profile is, however, robustly ruled out.

The models, in general, seem to prefer less mass in the areas over which we have kinematic constraints. In NFW models, the concentration c sets the normalization (or y-intercept) of the density profile. Because c cannot be lowered below an astrophysically reasonable limit, NFW models enclose more mass than cored models. This difference is reflected in the χ^2 difference between cored and NFW models, as the kinematics are best fit by models with less mass. Figure 3.2 hints at this as the best fit NFW model (dashed line) typically has higher values for σ than either the data or best-fitting cored model (solid line).

Several groups have approached the core/cusp issue in dSphs by taking advantage of the fact that some dSphs host multiple populations of tracer stars that are chemically and dynamically distinct. By fitting models to each component, the underlying dark matter profile can be modeled more accurately. Amorisco & Evans (2011a) fit two-component distribution function models to Sculptor, while Walker & Peñarrubia (2011) apply a convenient mass estimator (discussed below) to each stellar component in Sculptor and Fornax. It is believed that this mass estimator is unaffected by orbital anisotropy, thus their method yields a robust determination of the dynamical mass at two locations in the galaxy—allowing for the slope of the dark matter profile to be measured. Each of these studies finds models with a cored dark matter halo preferable to the predicted cuspy NFW profile.

It must be noted, however, that we are not observing the pristine initial dark matter distribution in this galaxy. Rather, it has likely been modified by complex

baryonic processes over the lifetime of the galaxy. These processes may include: adiabatic compression (Blumenthal et al., 1986), halo rebounding following baryonic mass loss from supernovae (Navarro et al., 1996a), or possibly dynamical friction acting on clumps of baryons (El-Zant et al. 2001; but see also Jardel & Sellwood 2009). Although we chose this galaxy because these effects were likely to be small, they are nevertheless not well understood and our result must be taken in that context.

3.5.2 Central IMBH

We are unable to place a significant constraint on the mass of a central IMBH. Figure 3.3 (upper right) shows the marginalized χ^2 curve against IMBH mass for cored dark matter density profiles. The curve asymptotes to low values of IMBH, thus we are only capable of placing an upper limit on the mass of any potential IMBH. Furthermore, our best-fit cored model with and without an IMBH have the same χ^2. We therefore impose a 1-σ upper limit on $M_\bullet \leq 3.2 \times 10^4 M_\odot$. It is unfortunate that we are not able to place a lower limit on $M_\bullet$ because measurements of black holes in the range $M_\bullet \lesssim 10^4 M_\odot$ place direct constraints on SMBH formation mechanisms. Our models, however, do robustly rule out a black hole of larger mass.

In massive galaxies it is thought that the radius of influence, $R_{\rm inf} \sim GM_\bullet/\sigma^2$ must be resolved in order to detect and precisely measure a black hole (Gebhardt et al., 2003; Kormendy, 2004; Ferrarese & Ford, 2005; Gültekin et al., 2009b). Using our upper limit on $M_\bullet$ we can calculate the maximum radius of influence of

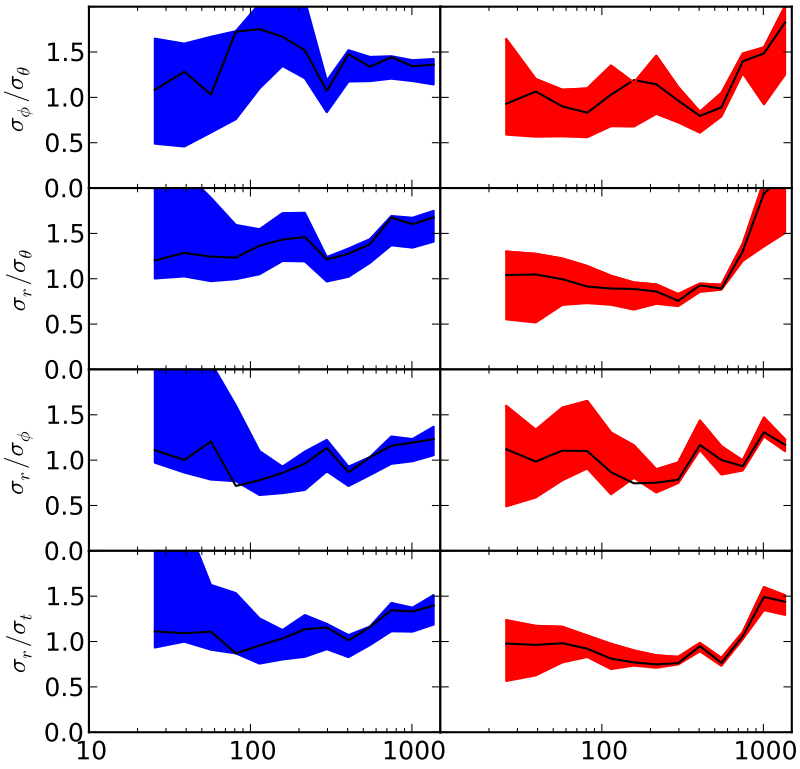

Figure 3.5 Anisotropy in various components of the velocity dispersion tensor. Blue and red shaded regions correspond to the 68% confidence regions along the major and minor axis, respectively. The black line is our best-fit model.

a potential black hole. Estimating the central velocity dispersion at $\sigma \sim 10$ km s^{-1} gives an upper limit for $R_{\rm inf} \lesssim 14$ pc. Our kinematics start at $R = 26$ pc, so it is not surprising that the minimum black hole mass we were able to detect has $R_{\rm inf}$ close to 26 pc. To detect smaller black holes, we require kinematics of stars closer to the center of the galaxy.

We are able to detect the dynamical influence of a black hole with a similar mass as Valluri et al. (2005) detect in NGC 205, however with kinematics of much lower resolution. Our innermost model bin is centered around 30 pc whereas they use high-resolution kinematics from the *Hubble Space Telescope* to resolve spatial scales less than 1 pc. The advantage we have is that the central velocity dispersion is much smaller in Fornax, which makes $R_{\rm inf}$ larger for fixed $M_\bullet$. NGC 205 is also more than five times as distant as Fornax.

3.5.3 Mass Estimators

Several authors have come up with convenient estimators of total mass within a given radius for local group dSphs. Strigari et al. (2008a) use the mass enclosed within 300 pc while Walker et al. (2009b) and Wolf et al. (2010) find a similar expression for the mass contained within the projected half-light radius. These estimators bear striking resemblance to a result obtained by Cappellari et al. (2006) derived from integral field kinematics of massive elliptical galaxies, and they all hint at an easy way to determine dynamical masses without expensive modeling. They are believed to be insensitive to velocity anisotropy based on the derivation in Wolf et al. (2010), and we compare their estimates to our models as a check on this.

For the mass contained within 300 pc we measure $M_{300} = 3.5^{+0.77}_{-0.11} \times 10^6 M_\odot$, roughly a factor of three smaller than Strigari et al. (2008a) who measure $M_{300} = 1.14^{+0.09}_{-0.12} \times 10^7 M_\odot$ using Jeans models with parameterized anisotropy.

The Cappellari et al. (2006), Walker et al. (2009b), and Wolf et al. (2010) mass estimators are all of the form

$$M(R_e) = k\langle\sigma^2_{LOS}\rangle R_e \tag{3.4}$$

with the difference between them reflected in their value of the constant k. In order to more fairly compare between these estimators and our models, we use the values for the luminosity-weighted line-of-sight velocity dispersion $\langle\sigma^2_{LOS}\rangle = 11.3^{+1.0}_{-1.8}\,\mathrm{km\ s^{-1}}$ and projected half-light radius $R_e = 689\,\mathrm{pc}$ that we calculate from the data used in our models.

Our best-fitting model has $M(R_e) = 3.9^{+0.46}_{-0.11} \times 10^7 M_\odot$ enclosed within the projected half-light radius. Interestingly, each mass estimator predicts a value for $M(R_e)$ significantly greater than what our models measure. With each group's value for k and our kinematics, the mass estimates are: $M(R_e) \approx 5.1^{+1.0}_{-1.5} \times 10^7 M_\odot$ (Walker et al., 2009b), $M(R_e) \approx 8.1^{+1.6}_{-2.4} \times 10^7 M_\odot$ (Wolf et al., 2010), and $M(R_e) \approx 1.0^{+0.3}_{-0.2} \times 10^8 M_\odot$ (Cappellari et al., 2006).

The evidence that mass estimators are anisotropy-independent comes largely from comparison to spherical Jeans models (except Cappellari et al. 2006). The weakness of these models is that the anisotropy must be parameterized and is restricted to be a function of radius only. Our models are not subject to these con-

straints since the anisotropy is calculated non-parametrically and is free to vary with position angle. We suggest that the best way to prove the accuracy of mass estimators is to compare with models that can self-consistently calculate both mass and anisotropy for realistic potentials.

For bright elliptical galaxies, Cappellari et al. (2006) and Thomas et al. (2011) have done just that. In these cases, the mass estimates are checked against masses derived from axisymmetric Schwarzschild modeling and good agreement is found. Ours is the first study to perform a similar test with dSphs, and there is no reason to assume that success with bright ellipticals guarantees accuracy in the dSph regime.

3.5.4 Tidal Effects

The principle of orbit superposition, and hence our entire modeling procedure, relies on the assumption that the galaxy is bound and in a steady state. The amount of tidal stripping in Fornax due to the effect of its orbit through the Milky Way's halo is not well-known. For reasonable values of Fornax total mass m, Milky Way mass M, and Galactocentric radius R_0, the tidal radius of Fornax is $r_t \sim (m/3M)^{1/3} R_0 \sim 13.5$ kpc. This estimate of r_t is sufficiently larger than our model grid that we would not expect tidal effects to be important over the radial range of our models. If Fornax is on an eccentric orbit about the Milky Way, however, the above equation for r_t is not valid and estimation of the tidal radius is not as straightforward. Fortunately, studies investigating its transverse motion suggest the orbit of Fornax is roughly circular (Piatek et al., 2007; Walker et al., 2008).

KG acknowledges support from NSF-0908639. We thank the Texas Advanced Computing Center (TACC) for providing state-of-the-art resources for computing. We are grateful to the Magellan/MMFS Survey collaboration for making the stellar velocity data publicly available. Additionally, we thank Matthew Walker, Mario Mateo, and the anonymous referee for helpful comments on an earlier draft of the paper.

Chapter 4

Measuring Dark Matter Profiles Non-Parametrically in Dwarf Spheroidals: An Application to Draco[1]

"I see nobody on the road" said Alice.
"I only wish *I* had such eyes," the King remarked in a fretful tone.
"To be able to see Nobody! And at that distance too!
Why, it's as much as *I* can do to see real people, by this light."

Lewis Carroll - *Through the Looking-Glass*

We introduce a novel implementation of orbit-based (or Schwarzschild) modeling that allows dark matter density profiles to be calculated non-parametrically in nearby galaxies. Our models require no assumptions to be made about velocity anisotropy or the dark matter profile. The technique can be applied to any dispersion-supported stellar system, and we demonstrate its use by studying the Local Group dwarf spheroidal (dSph) galaxy Draco. We use existing kinematic data at larger radii and also present 12 new radial velocities within the central 13 pc obtained with the VIRUS-W integral field spectrograph on the 2.7m telescope at McDonald Observatory. Our non-parametric Schwarzschild models find strong evidence that the dark matter profile in Draco is cuspy for $20 \leq r \leq 700$ pc. The profile for $r \geq 20$ pc is well-fit by a power law with slope $\alpha = -1.0 \pm 0.2$, consistent

[1]Published in Jardel, J., R., Gebhardt, K., Fabricius, M., Drory, N., Williams, M., J., 2013, ApJ, 763, 91. Reprinted with permission from the American Astronomical Society.

with predictions from Cold Dark Matter (CDM) simulations. Our models confirm that, despite its low baryon content relative to other dSphs, Draco lives in a massive halo.

4.1 Introduction

Understanding how dark matter is distributed in low-mass galaxies is central to the study of galaxy formation in the cold dark matter (CDM) paradigm. The first CDM simulations predicted that all dark matter halos share a universal density profile with a cuspy inner slope of $\alpha \equiv d\ln\rho_{DM}/d\ln r = -1$ (Navarro et al. 1996b, hereafter NFW). When observers began studying low-mass galaxies, however, they mostly found halos with a uniform density $\alpha = 0$ core (Burkert, 1995; Persic et al., 1996; Borriello & Salucci, 2001; de Blok et al., 2001; Blais-Ouellette et al., 2001; Simon et al., 2005). This disagreement between theorists and observers over the form of $\rho_{DM}(r)$ became known as the core/cusp debate.

Since the debate began, the number of profile parameterizations used to describe low-mass galaxies by both theorists and observers has only increased. Observers champion empirical fits such as the Burkert profile (Burkert, 1995; Salucci & Burkert, 2000), cored isothermal models (Persic et al., 1996) or simply generic broken power laws (Koch et al., 2007; Strigari et al., 2008b; Walker et al., 2009b). Theorists have also introduced new fits to their simulated halos with varying, although still cuspy, inner slopes (Navarro et al., 2004; Stadel et al., 2009; Navarro et al., 2010). Modeling a galaxy with each of these parameterizations would not only be time consuming, but also biased if the true profile is unlike any of them. It is therefore preferable to use non-parametric methods to determine $\rho_{DM}(r)$.

Van den Bosch et al. (2006) first experimented with non-parametric orbit-based models by allowing the mass-to-light ratio M/L to vary with radius in the globular cluster M15. We introduce a similar modeling technique that uses axisym-

metric Schwarzschild modeling, combined with knowledge of the full line-of-sight velocity distribution (LOSVD) of stars, to break the well-known degeneracy between mass and orbital anisotropy. We demonstrate the capability of these models by applying them to the Local Group dwarf spheroidal (dSph) galaxy Draco. Draco is part of an interesting class of objects that are some of the most dark matter-dominated galaxies discovered. This makes differentiating between dark and luminous mass in dSphs easier as the baryons have less of an effect on the total density profile than they do in larger galaxies. Recently, using improved data and modeling techniques, Adams et al. (2012) found a cuspy dark matter profile in the low-mass galaxy NGC 2796 where previous studies found a core. Studies like these motivate us to investigate the dSphs with more sophisticated models.

Our models represent a significant improvement over previous work on dSphs as most studies use spherical Jeans models (Gilmore et al., 2007; Walker et al., 2009b; Wolf et al., 2010) which require the modeler to make assumptions about the nature and degree of the anisotropy. These assumptions vary in complexity from simply assuming isotropy, which can bias the estimate of α (Evans et al., 2009), to parameterizing the anisotropy as a general function of radius (Strigari et al., 2008b; Wolf et al., 2010). Models that allow for more freedom in the anisotropy typically fall victim to the mass-anisotropy degeneracy and cannot robustly determine the inner slope of $\rho_{DM}(r)$ (Walker et al., 2009b). We hope to make a robust determination of the inner slope in Draco with a suite of more general non-parametric Schwarzschild models.

4.2 Non-parametric Schwarzschild Models

At the heart of our non-parametric technique is the orbit-based modeling code developed by Gebhardt et al. (2000b, 2003), updated by Thomas et al. (2004, 2005), and described in detail in Siopis et al. (2009). All orbit-based codes are based on the principle of orbit superposition first introduced by Schwarzschild (1979). Similar axisymmetric codes are used by Rix et al. (1997),van der Marel et al. (1998), Cretton et al. (1999), and Valluri et al. (2004) while van den Bosch et al. (2008) present a fully triaxial modeling code. The current Schwarzschild models that allow for dark matter do so by requiring the modeler to assume a parameterization for the dark matter density profile $\rho_{DM}(r)$. Unfortunately, this parameterization is often exactly what we wish to determine. Current methods get around the circular logic of this dilemma by running models with different parameterizations and comparing their relative goodness-of-fit with a χ^2 test. Non-parametric modeling sidesteps the issue entirely, and lets the parameterization of $\rho_{DM}(r)$ be output from the models, rather than input as a guess.

The principle of orbit superposition works by choosing from a library of all possible stellar orbits only those orbits that best reproduce the observed kinematics of the galaxy being modeled. If we know the mass density profile of the galaxy, and hence the potential, we can compute the appropriate orbit library. However, since we do not know the potential of the galaxy, we must construct a number of models with slightly different mass distributions and compare the goodness-of-fit of the resulting allowed orbits. The radial profile of the total (dark + stellar) mass density in a galaxy can be written as:

$$\rho(r) = \frac{M_*}{L} \times \nu(r) + \rho_{DM}(r) \tag{4.1}$$

where M_*/L is the mass-to-light ratio of the stars, $\nu(r)$ is the stellar luminosity density profile, and $\rho_{DM}(r)$ is the dark matter density profile. In principle we know M_*/L, which can vary as a function of radius, from stellar population models. We also know $\nu(r)$ from the de-projection of the observed surface brightness profile. Our task is to construct orbit libraries for varying $\rho(r)$ and match the allowed orbits to kinematics in the form of LOSVDs—the distribution of projected velocities observed. Some orbit libraries will contain orbits that do a good job at fitting the observed LOSVDs and others will not. The best-fitting model identifies the best-fitting $\rho(r)$. Once we know this, we can invert Equation (4.1) to solve for $\rho_{DM}(r)$. The trick is to vary $\rho(r)$ in a systematic way. This is the principal difference between our new approach and standard Schwarzschild modeling which tries to vary $\rho(r)$ by varying the parameters that define an assumed dark matter profile.

To compute the orbit library for each model, we first calculate the potential. We assume axisymmetry and make use of the stellar ellipticity to define the density at angle θ in our meridional grid. The dark matter halo is assumed to have the same ellipticity as the stars. We solve Poisson's equation for the potential associated with this density distribution by decomposing $\rho(r, \theta)$ into spherical harmonics (Siopis et al., 2009). With the potential known, we launch 20,000-30,000 orbits and integrate their motion for roughly 100 crossing times, storing position and velocity information at each timestep.

Orbits in axisymmetric potentials respect three isolating integrals of motion: energy E, the z-component of angular momentum L_z, and the non-classical third integral I_3. By specifying all three of these quantities together, an orbit is uniquely defined. Unfortunately, there is no analytical form for I_3 and it is generally not known a priori. We therefore rely on the sampling scheme of Thomas et al. (2004) to construct an orbit library which uniformly samples E, L_z, and I_3 and thereby contains all possible orbits for a given potential.

Each orbit in the library is given a weight w_i, and a set of w_i are chosen so the observed kinematics are appropriately reproduced by the orbits which have been weighted, averaged, and projected. Quantitatively, we observe N_{LOSVD} LOSVDs in the galaxy at various positions. Each LOSVD contains N_{vel} velocity bins with uncertainties, so the number of observables the models must match to is given by the product $N_{\mathrm{LOSVD}} \times N_{\mathrm{vel}}$. The goodness-of-fit of a model is judged by

$$\chi^2 = \sum_{i=1}^{N_{\mathrm{LOSVD}}} \sum_{j=1}^{N_{\mathrm{vel}}} \left(\frac{\ell_{ij}^{\mathrm{obs}} - \ell_{ij}^{\mathrm{mod}}}{\sigma_{ij}} \right)^2 \tag{4.2}$$

where ℓ_{ij}^{obs} and ℓ_{ij}^{mod} are the j^{th} velocity bin of the i^{th} LOSVD from the observations and model respectively, and σ_{ij} is the uncertainty in ℓ_{ij}^{obs}.

Given the freedom to choose from upwards of 10,000 orbital weights to match only $N_{\mathrm{LOSVD}} \times N_{\mathrm{vel}} \sim 100$ observables, a standard χ^2 minimization routine can populate the distribution function in any number of ways that introduce unwanted noise. To avoid distribution functions that are noisy or unrealistic, however still consistent with the observables, we employ a maximum entropy smoothing

technique developed by Richstone & Tremaine (1988) and described in Siopis et al. (2009). Instead of minimizing χ^2, we maximize the objective function

$$\hat{S} = -\sum_{i=1}^{N_{\rm orb}} w_i \log\left(\frac{w_i}{\Delta\Omega_i}\right) - \alpha_S \chi^2 \tag{4.3}$$

where $N_{\rm orb}$ is the number of orbits in the library, and $\Delta\Omega_i$ is the phase-space volume of the $i^{\rm th}$ orbit. See Siopis et al. (2009) for a technical description of how we calculate phase-space volumes and maximize $\hat{S}$.

The first term in Equation (4.3) is an entropy-like quantity and the second term is χ^2 from Equation (6.1). The parameter α_S controls which term influences $\hat{S}$. For small α_S, orbital weights are chosen to produce a smooth distribution function at the expense of reproducing the data. For large α_S, the data are well-fit by the model (χ^2 is small), but the resulting distribution function is likely not smooth. We determine the appropriate α_S for each model using the scheme described in Siopis et al. (2009). We start with $\alpha_S = 0$ and incrementally increase it until changes to χ^2 between successive iterations are small. Thus, the maximum entropy constraint serves to initialize the search for the minimum when $\alpha_S = 0$. By slowly increasing α_S, we drive down the importance of entropy to the fit until it no longer matters.

4.2.1 Varying $\rho(r)$ Between Models

The major innovation of our new modeling technique is how we choose the density profile $\rho(r)$ of each model. Current methods assume $\rho_{DM}(r)$ and calculate $\rho(r)$ from Equation (4.1), however this requires knowledge of the appropriate pa-

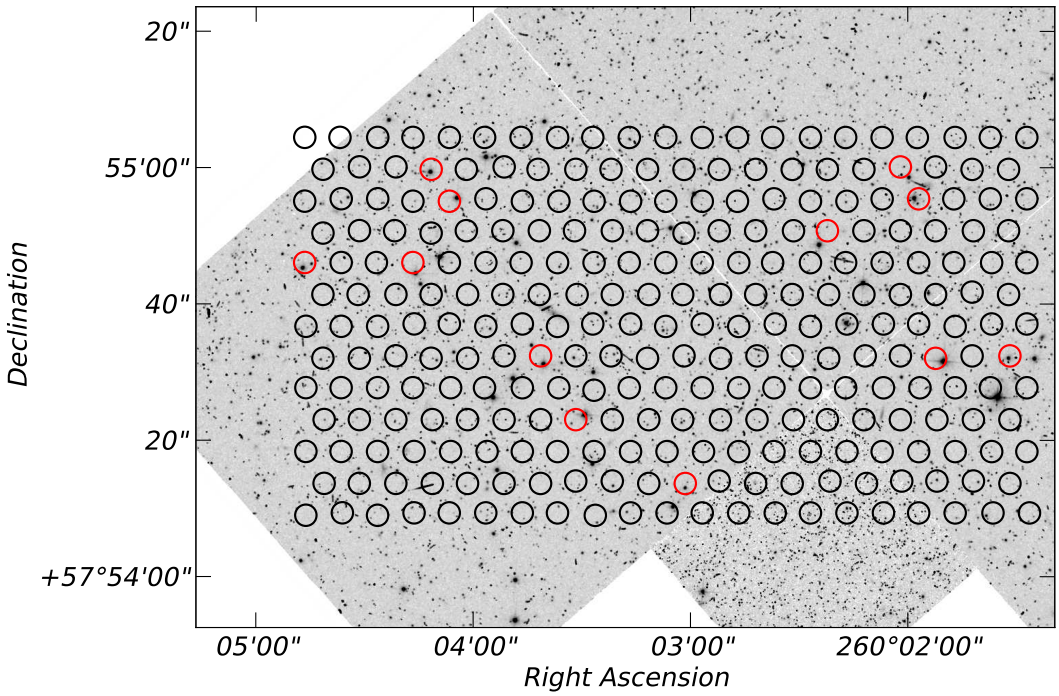

Figure 4.1 VIRUS-W IFU overlaid on top of an *HST* image from Ségall et al. (2007). Red circles highlight fibers containing stars used in the determination of the central LOSVD. Note the *HST* PSF is significantly smaller than the typical $2''$seeing at McDonald Observatory.

rameterization for $\rho_{DM}(r)$. We use a fundamentally different strategy and divide $\rho(r)$ into $N_{\rm bin}$ discrete points whose value ρ at radius r_i is labeled ρ_i. The $N_{\rm bin}$ points are spaced evenly in log r and connected by straight line segments. Each trial density profile is now defined by the ρ_i at each of the $N_{\rm bin}$ bins. We run many models adjusting the values of the ρ_i so as to sample all possible density profiles. This strategy requires no assumptions to be made about the shape of $\rho(r)$ or $\rho_{DM}(r)$, but it is computationally intensive for large $N_{\rm bin}$.

The choice of $N_{\rm bin}$ is a compromise between accuracy in reproducing $\rho(r)$ and computational resources. Large values of $N_{\rm bin}$ can make parameter space impossibly large, while small values can be overly restrictive on $\rho(r)$. We have experimented with $N_{\rm bin}$= 5, 7, and 10. The added freedom with $N_{\rm bin}$=7 or 10 was not found to be worth the increase to the dimensionality of parameter space. We have also tried connecting the ρ_i with splines, but found the additional freedom produced unrealistic density profiles. Concern over the smoothness of $\rho(r)$ may be mitigated by the fact that $\rho(r)$ only matters to our models in that it determines the potential. As the potential is the integral of $\rho(r)$, this introduces additional smoothness.

We extrapolate the density at the outermost point as a power law with slope α_∞. The only parameters in the model are the ρ_i themselves and the extrapolation slope α_∞. The models also have the flexibility to add a central black hole of mass $M_\bullet$ to the galaxy for future studies.

4.2.2 Separating dark from stellar mass

Once the best-fitting $\rho(r)$ is found, the task remains still to recover the underlying dark matter density profile. This involves finding some other constraint on the stellar mass-to-light ratio. We can often determine M_*/L from simple stellar population (SSP) models. The required input for SSP models varies greatly, and different methods are appropriate depending on the galaxy modeled. For example, if spectra are available, stellar population synthesis models or Lick indices can be used. Lacking spectra, one can use the relations between broad-band colors and M_*/L (Bell & de Jong, 2001). In nearby dSph galaxies where individual stars are resolved, color-magnitude diagrams can be constructed to fit for age and metallicity with isochrones. We can also evaluate the radial variation of M_*/L as well without much additional effort. Spectral or photometric data need only be spatially binned with the same procedure repeated at each bin. Once M_*/L is calculated, stellar density is simply the product of the (possibly radially varying) $M_*/L \times \nu(r)$.

4.3 Application to Draco

We apply our new non-parametric Schwarzschild modeling technique to study the nearby Draco dSph. Draco is a satellite galaxy of the Milky Way orbiting at a distance from the sun of only 71 kpc (Odenkirchen et al., 2001). At this distance individual stars are resolved even with ground-based observatories. Consequently, the data we use are radial velocities of individual stars. Radial velocities are available for 158 stars in Draco, and we present radial velocities from new observations of an additional 12 stars near the center of Draco.

We choose Draco because it is the most dark matter-dominated of the "classical" (pre-SDSS) dSphs. We can therefore differentiate between dark and luminous mass more easily since the baryons contribute less to the total density profile than they do in larger galaxies. Consequently, we can absorb larger uncertainties in M_*/L. The primary science goal of this work, and a future study of all dSphs, is to determine the functional form of the dark matter profile in dSphs and compare results to theoretical predictions by CDM.

4.3.1 Data

4.3.1.1 Kinematics

We use a combination of published radial velocities and new observations for kinematics in Draco. Data exist at larger radii for 158 stars (Kleyna et al., 2002), but we wish to explore the central region of Draco in order to have the best constraint on the inner slope of $\rho_{DM}(r)$.

To accomplish this, we observe the center of Draco with the VIRUS-W integral field unit (IFU) spectrograph (Fabricius et al., 2008) on the 2.7m Harlan J. Smith telescope at McDonald Observatory . This instrument allows for a high density of stars to be observed simultaneously, but with the drawback that fibers are not positionable. There are 267 fibers that cover the $105'' \times 55''$ field of view with a $1/3$ fill factor. We observed the spectral region covering 4900Å to 5500Å with a resolving power $R \sim 9000$.

The observations took place over the first half of 5 nights from 2011 August 1-5 in excellent conditions. Seeing was typically $2''$or better, which is smaller than

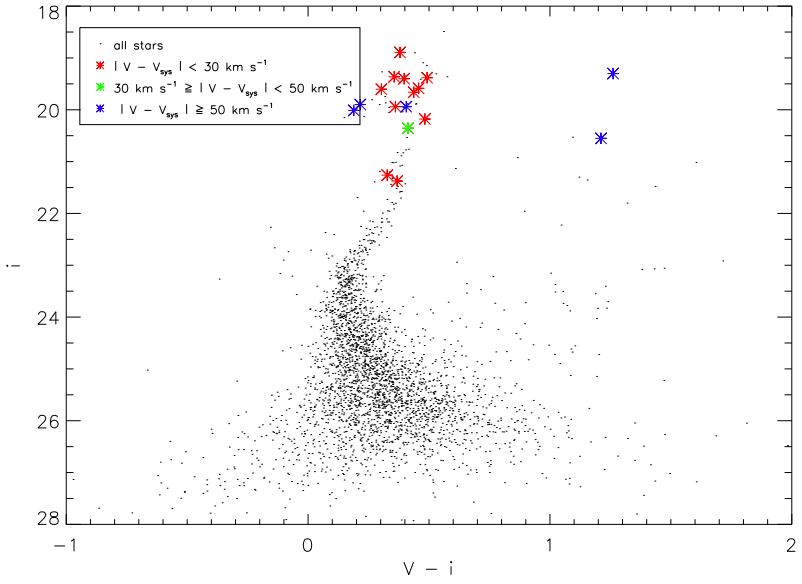

Figure 4.2 Color-magnitude diagram of stars near the center of Draco. Colored asterisks are stars we observe, coded according to their offset from Draco's systemic velocity V_{sys}. Red stars have $|V - V_{sys}| < 30$ km s^{-1}, blue stars have $|V - V_{sys}| > 50$ km s^{-1}, and the green star has a radial velocity between 30 and 50 km s^{-1}of V_{sys}.

the $3\farcs2$ diameter fibers. The standard battery of bias, Hg-Ne arc lamp, and twilight calibration frames were taken at the start of each night. We use an early implementation of the Cure data reduction software. Cure is being developed as the pipeline for the Hobby-Eberly Dark Energy Experiment (HETDEX) (Hill et al., 2006). We briefly describe steps taken to reduce the VIRUS-W data. A detailed description of Cure is beyond the scope of this paper.

We perform standard CCD processing steps, using the fitstools package (described in Gössl & Riffeser 2002), to create master bias, twilight flat, and arc lamp images for each night. We use twilight flats in combination with arc lamp images to determine the distortion solution–a two-dimensional map which translates the (x,y) position of a pixel on the CCD to a fiber number and wavelength.

Our science frames consist of 15-minute integrations of a single pointing of the central part of the galaxy. Prior to observing, we determined the optimal position of the IFU by examining *Hubble Space Telescope (HST)* photometry of the central region (Ségall et al., 2007). With accurate fiber and star positions, we determined a pointing that maximizes the number of bright stars on fibers (see Figure 4.1). There are 57 science frames with this pointing, totaling roughly 14 hours of integration.

We apply each night's distortion solution to the science frames yielding rectified, wavelength-calibrated frames. We then collapse and median-combine these science frames along with the twilight flat frames. Each night's stacked science frame is divided by the appropriate master flat for that night.

Since the majority of the 267 fibers in the IFU are on empty sky, we are able

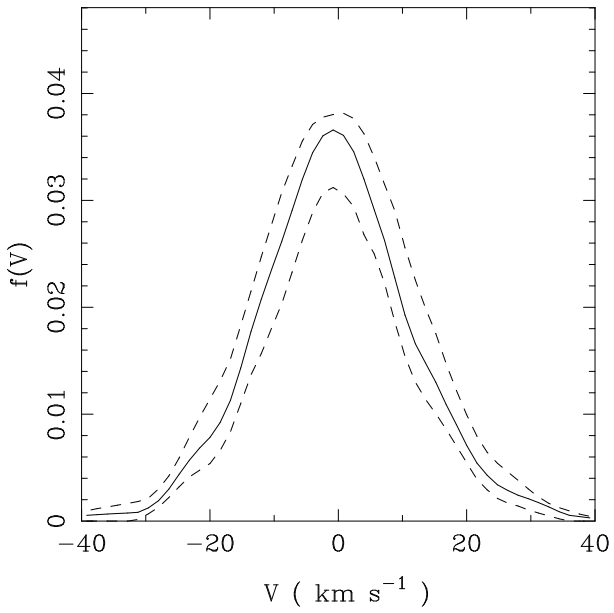

Figure 4.3 LOSVD generated from the discrete velocities of 29 stars

to calculate an accurate sky model directly from each science frame. We compute this sky model for each fiber on the chip using a moving-window average of 20 nearby fibers. We subtract the sky model from each frame, and the resulting sky-subtracted frames for each night are median-combined.

We extract 1-D spectra from 17 fibers containing stars. Star 2 in our sample is used as a velocity standard since it is the brightest member star with known radial velocity from Armandroff et al. (1995). We cross-correlate the other 16 spectra to star 2 using the IRAF task `FXCORR`. By cross-correlating to the spectrum of a star with known heliocentric radial velocity in Draco, we automatically remove the contribution from Earth-Sun motion. We perform the cross-correlation analysis on the combined image, and in doing so introduce a small bias due to the change in the

Table 4.1. Radial Velocities Obtained with VIRUS-W

Star	RA	Dec	$V_{\rm helio}$ km s^{-1}	$\Delta V_{\rm helio}$ km s^{-1}	R_{TD}
1	$17^{\rm h}20^{\rm m}14^{\rm s}.76$	$+57°54'32.''40$	-288.1	2.57	4.76
2	$17^{\rm h}20^{\rm m}07^{\rm s}.49$	$+57°54'32.''04$	-299.1[1]	1.89[1]	...
3	$17^{\rm h}20^{\rm m}06^{\rm s}.12$	$+57°54'32.''40$	-293.1	3.99	8.75
4	$17^{\rm h}20^{\rm m}14^{\rm s}.11$	$+57°54'23.''04$	-310.9	3.35	6.01
5	$17^{\rm h}20^{\rm m}12^{\rm s}.10$	$+57°54'13.''68$	-270.6	3.37	7.47
6	$17^{\rm h}20^{\rm m}16^{\rm s}.78$	$+57°54'59.''76$	-276.2	1.91	12.98
7	$17^{\rm h}20^{\rm m}08^{\rm s}.14$	$+57°55'00.''12$	-258.4	3.89	7.87
8	$17^{\rm h}20^{\rm m}16^{\rm s}.44$	$+57°54'55.''08$	-293.2	6.05	8.01
9	$17^{\rm h}20^{\rm m}07^{\rm s}.80$	$+57°54'55.''44$	-307.6	4.51	10.92
10	$17^{\rm h}20^{\rm m}09^{\rm s}.48$	$+57°54'50.''76$	-277.7	3.61	8.02
11	$17^{\rm h}20^{\rm m}19^{\rm s}.10$	$+57°54'46.''08$	-292.2	3.23	10.94
12	$17^{\rm h}20^{\rm m}17^{\rm s}.11$	$+57°54'46.''08$	-277.8	2.17	14.39

[1]From Armandroff et al. (1995)

Note. — Heliocentric radial velocities for the 12 member stars observed with VIRUS-W at the center of Draco

heliocentric velocity correction over the course of the observing run. However, the magnitude of this change is only 0.1 km s^{-1}, much smaller than our uncertainties.

We list the heliocentric radial velocities and Tonry-Davis R_{TD} values determined for the 12 stars we report as members in Table 4.1. The Tonry-Davis value indicates the relative strength of the primary peak in the cross-correlation function to the average (Tonry & Davis, 1979). The right ascension and declination given for each star in Table 4.1 indicate the position of the center of the VIRUS-W fiber containing that star.

To determine membership for the 17 stars, we use the photometry of Ségall et al. (2007) to produce a color-magnitude diagram (CMD). Figure 4.2 presents the resulting CMD, where the colored symbols indicate observed stars. We also group the stars according to their offset from Draco's systemic velocity, which we assume is $V_{\rm sys} = -293$ km s^{-1} (Armandroff et al., 1995). Stars with radial velocity offsets greater than 50 km s^{-1} are classified as non-members, while stars with offsets less than 30 km s^{-1} are categorized as members. The one star with radial velocity $V - V_{\rm sys} = 32.6 \pm 3.9$ km s^{-1}(green symbol in Figure 4.2) is classified as a possible member. Possible and non-members are discarded from further analysis, leaving 12 member stars. Note that blind sigma-clipping retains these same 12 stars as members.

We have individual radial velocities for stars at positions around the galaxy, but our models want the full distribution of radial velocities at each position (the LOSVDs). We group the individual velocities into spatial bins and determine the LOSVD at each bin via an adaptive kernel density estimator (Silverman, 1986; Gebhardt et al., 1996). In velocity space, this procedure replaces each of the N discrete observations with a kernel of width h and height proportional to $N^{-1}h^{-1}$. We use the Epanechnikov kernel (an inverted parabola) and sum the contribution from each discrete velocity to obtain a non-parametric representation of the LOSVD. The 1σ uncertainties on the LOSVDs are calculated through bootstrap resamplings of the data (i.e. sampling with replacement from the N velocity measurements, see Gebhardt et al. 1996; Jardel & Gebhardt 2012). In Figure 4.3 we show an example LOSVD.

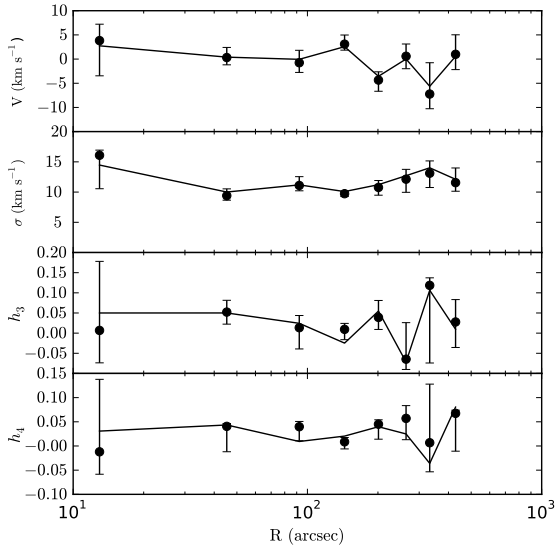

Figure 4.4 Gauss-Hermite moments fit to the 8 LOSVDs generated from 170 radial velocities. The solid line is the result of our best-fit model.

We combine the new VIRUS-W data with 158 additional radial velocities from the literature (Kleyna et al., 2002). We divide these 170 radial velocities into 8 radial bins of roughly 20 stars each. LOSVDs are calculated for each of these bins, yielding kinematics coverage over the radial range 25″–1500″ (8 pc–500 pc). We fit Gauss-Hermite moments to the 8 LOSVDs and plot the kinematics in Figure 6.2. This is only done for comparison purposes as the models fit directly to the LOSVDs. We compare the velocity dispersion as determined from the Gauss-Hermite fit with the standard deviation of the individual velocities (using the biweight scale; see Beers et al. 1990) in order to determine the best value for the smoothing width h.

The issue of foreground contamination frequently comes up in the study of dSphs using individual radial velocities. There is always the possibility that some

fraction of the observed stars are members of the Milky Way. These stars would be velocity outliers and therefore artificially increase the measured velocity dispersion or, in our case, the width of the LOSVD. Fortunately, the foreground Milky Way stars are well-separated in velocity space from the Kleyna et al. (2002) sample. Contaminants are also unlikely to have colors and magnitudes that place them on the red giant branch of Draco's color-magnitude diagram. Łokas et al. (2005) use these two constraints to estimate that there are of order 1-2 Milky Way contaminants in the entire Kleyna et al. (2002) data set.

4.3.1.2 Photometry

Our models are required to not only match the observed LOSVDs but also the three-dimensional luminosity density profile $\nu(r)$. The first step in obtaining $\nu(r)$ is to measure the two-dimensional surface brightness profile. We use the photometry of Ségall et al. (2007) who publish a number density profile of stars in Draco. This profile covers the radial range from $15''$- $2400''$. We extrapolate the profile as a power law out to $R = 6000''$ by fitting a constant slope to the profile in logarithmic space. To convert the number density profile to an effective surface brightness profile, we apply an arbitrary zeropoint shift in log space until the luminosity obtained by integrating the surface brightness profile is consistent with the observed luminosity (Mateo, 1998). We plot this surface brightness profile in Figure 6.1.

We deproject the surface brightness profile according to the procedure detailed in Gebhardt et al. (1996). We assume surfaces of constant luminosity density

ν are coaxial spheroids and perform an Abel inversion. For Draco we adopt an ellipticity of $e = 0.3$ (Odenkirchen et al., 2001). We assume an inclination of $i = 90^\circ$ for simplicity. Inclination is typically one of the more difficult quantities to constrain (Thomas et al., 2007b). In addition to simplifying our models, assuming $i = 90^\circ$ provides the advantage that the deprojection is unique. For a detailed discussion of how uncertainties in viewing angle and geometry propagate through our models see Thomas et al. (2007a).

The resulting luminosity density profile we calculate has an average logarithmic slope $\langle d\ln\nu/d\ln r\rangle = -0.4$ inside 50 pc. In Figure 6.1 we plot $\nu(r)$ and also illustrate the positions of our kinematics data.

4.3.2 Models

Our non-parametric models of Draco use $N_{\rm bin}$=5 radial bins spaced equally in $\log r$ from 15″to 2000″. We initialize our search for the minimum with a brute force method, constructing a coarse grid in $N_{\rm bin}$+1 dimensions from which we calculate all possible permutations of the $N_{\rm bin}$ parameters and the extrapolated slope α_∞. Additionally, we require the density profile of each model to be monotonically decreasing or constant. This is a natural constraint, and it significantly lowers the number of models needed to sample parameter space.

Once the models defining the coarse grid are evaluated, we employ an iterative sampling scheme to focus in on and define the minimum in better detail. This method takes all the models with χ^2 within $\chi^2_{\rm lim}$ of the minimum $\chi^2_{\rm min}$ as starting points. For each starting point, a fractional step of size δ_i is taken above and below

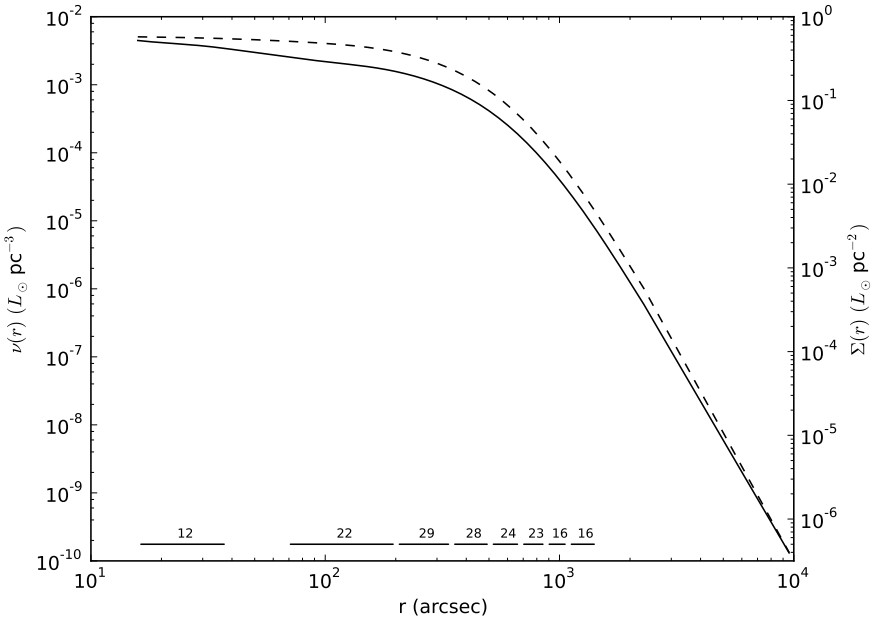

Figure 4.5 Surface brightness profile $\Sigma(r)$ (dashed) and deprojected luminosity density profile $\nu(r)$ (solid) used in our models. Horizontal lines near the x-axis indicate the radial position of our kinematics bins. Numbers refer to the number of radial velocities used per bin. Note the central location of the new VIRUS-W data (innermost bin) in comparison to existing data.

the initial value, one at a time, for all the density bins. If there is no change to $\chi^2_{\rm min}$, then δ_i is decreased. This procedure is repeated until δ_i is less than a specified threshold. Additional models are also run as needed to fill in regions of parameter space that appear interesting.

We do not attempt to fit for α_∞ as we clearly do not have kinematics in that radial range to constrain the mass. Instead, we treat α_∞ as a nuisance parameter and marginalize over it in our analysis. We restrict the value of the extrapolated slope to $\alpha_\infty \in \{-2,-3,-4\}$ and every $\rho(r)$ we sample has been run with each of these values. These slopes are representative of the isothermal, NFW, and Hernquist (1990) density profiles.

Since Draco orbits within the dark matter halo of the Milky Way, it is probable that is has been tidally stripped at large radii. To account for this, the density is truncated at the tidal radius r_t defined by

$$r_t \sim \left(\frac{m}{3M}\right)^{1/3} D. \tag{4.4}$$

For reasonable values of the Milky Way's mass M, Draco's mass m, and the Galactocentric radius of Draco's orbit D (assumed circular), Equation 4.4 gives an approximate tidal radius $r_t \approx 3$ kpc. We therefore truncate $\rho(r)$ at this radius. We also assume the dark halo in Draco has the same flattening as the stars and therefore leave q_{DM} fixed at 0.7. In the future we plan to investigate models with varying q_{DM}, however that is not the focus of this paper.

4.4 Results

The χ^2 curves for all the ρ_i are plotted in Figure 4.6. Each dot represents a single model, and the red curve is a smoothed fit to the minimum. We obtain the red curve through a smoothing process that is similar to a boxcar average, except that we take the biweight of the 7 lowest χ^2 values within the boxcar. This method is therefore less sensitive to outliers than a traditional boxcar average. When determining a smoothed fit to the minimum, one is tempted to use only the points with the lowest χ^2. However, numerical noise causes models to scatter to both higher and lower χ^2 in some bins. This is difficult to see by eye because scatter to higher values of χ^2 causes the models to blend in with the black points in Figure 4.6 while scatter to lower χ^2 makes models appear to stand out. The sliding biweight robustly picks out the center of this distribution

The red curve plots $\chi^2(\rho_i)$ for each radial bin, and therefore gives an indication of the model-preferred density at radius r_i. We estimate the 1σ uncertainties on each of the ρ_i by determining the portion of each parameter's χ^2 curve, marginalized over all other parameters, that lies within $\Delta\chi^2 = 1$ of the overall minimum. Figure 4.6 shows this limit as a horizontal line whose intersection with the red curve indicates the 1σ range of the density at bin i. In all further analysis we identify the midpoint of this range as the best-fitting value and report uncertainties as symmetric about this value.

In two cases, bins 4 and 5, there are secondary minima that extend almost to the $\Delta\chi^2 = 1$ line but not quite. It is likely that with perfect coverage of parameter space the area between these minima would be filled in. However, available

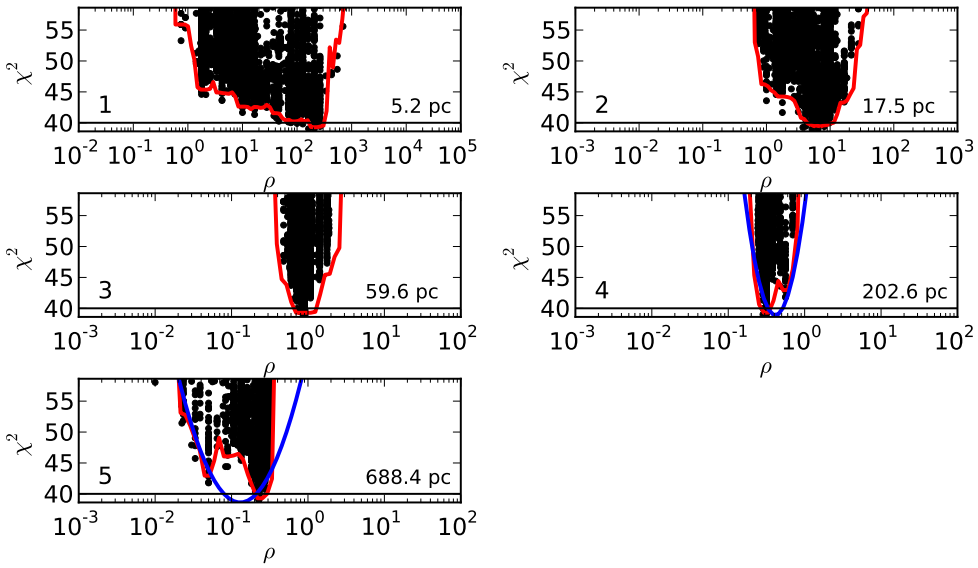

Figure 4.6 χ^2 curves for all of the ρ_i parameters. Each black dot represents a single model (combination of $\rho_1, \rho_2, \ldots \rho_5$) and the red curve is a smoothed fit to the minimum. The red curve in any panel therefore is the χ^2 curve marginalized over the other density points. The unit of density is $M_\odot$ pc^{-3}. In panels 4 and 5, the blue curve is a parabola in $\log \rho$ that we use to interpolate between two local minima.

computational resources limit the extend to which we can sample parameter space. In order to be more conservative in our analysis we fit a quadratic in $\log \rho$ to these minima, centered roughly on the midpoint between them (blue curves in Figure 4.6).

The best-fitting model has unreduced $\chi^2_{\rm min} = 9.1$, and the number of observables our models fit to is $\nu = N_{\rm LOSVD} \times N_{\rm vel} = 8 \times 15 = 120$. If we were to naively calculate a reduced χ^2, we would estimate $\chi^2_\nu = 0.08$. This low value of χ^2_ν results from an overestimation of the number of independent degrees of freedom ν. The adaptive kernel density estimator we use to compute the LOSVDs introduces correlations among neighboring velocity bins, therefore reducing the number of truly independent degrees of freedom.

To account for this, we consider the Gauss-Hermite parameterizations of our best-fitting model (solid line in Figure 6.2) and input LOSVDs (points with error bars in Figure 6.2). This model has $\chi^2_{\nu_{GH}} = 0.33$ where ν_{GH} is 4 Gauss-Hermite parameters $\times$ 8 LOSVDs= 32. This $\chi^2_{\nu_{GH}}$ is still less than 1, however it is more consistent with previous studies (Gebhardt et al., 2003) and may be due to correlations among the Gauss-Hermite parameters (e.g. Houghton et al. 2006). We use $\chi^2_{\nu_{GH}}$ to calculate the appropriate scaling to apply to our models which use the LOSVDs in determining χ^2. We scale all un-reduced χ^2 values by the factor $\chi^2_{\nu_{GH}}/\chi^2_\nu = 4.3$

4.4.1 Obtaining M_*/L

We have so far identified the best-fitting total density profile. In order to study the dark matter profile we must subtract the stellar density profile $\rho_*(r)$. This

involves finding an independent constraint on the stellar mass-to-light ratio M_*/L. Using stars within the central $5'$ of Draco, we construct a $g' - i'$ color-magnitude diagram (CMD) from the photometry of Ségall et al. (2007). We fit isochrones (Marigo et al., 2008) to the CMD, corrected for Galactic extinction (Schlegel et al., 1998), so that we may determine the age and metallicity of the stellar population.

Figure 4.7 shows the CMD with our best isochrone fit. The red giant branch is well-defined, and we obtain a sensible fit with age $t_{\rm age} = 12.7$ Gyr and metallicity $[{\rm Fe/H}] = -1.4$. Using the SSP models from Maraston (2005) we are able to convert $t_{\rm age}$ and $[{\rm Fe/H}]$ to a V-band stellar mass-to-light ratio $M_*/L_V = 2.9 \pm 0.6$. Uncertainties in M_*/L_V represent the spread in SSP predictions when different initial mass functions are assumed in the models.

4.4.2 The Dark Matter Profile

With M_*/L_V determined from stellar population models, we can subtract $\rho_*(r)$ from the best-fitting total density profile obtained during the modeling procedure. We plot the resulting dark matter profile in Figure 4.8. The red band is the 68% confidence band for each density point, marginalized over the others, and the gray band shows the 68% confidence band of all the parameters jointly (at $\Delta\chi^2 = 7.04$).

From Figure 4.8, it seems plausible that $\rho_{DM}(r)$ can be fit by a power law of the form $\log\rho_{DM} = \alpha \log r + \beta$ with the exception of perhaps the innermost data point. The slope of this fit α can be directly compared to both theoretical predictions and observations of similar dSphs. The innermost point, however, is puzzling. Its

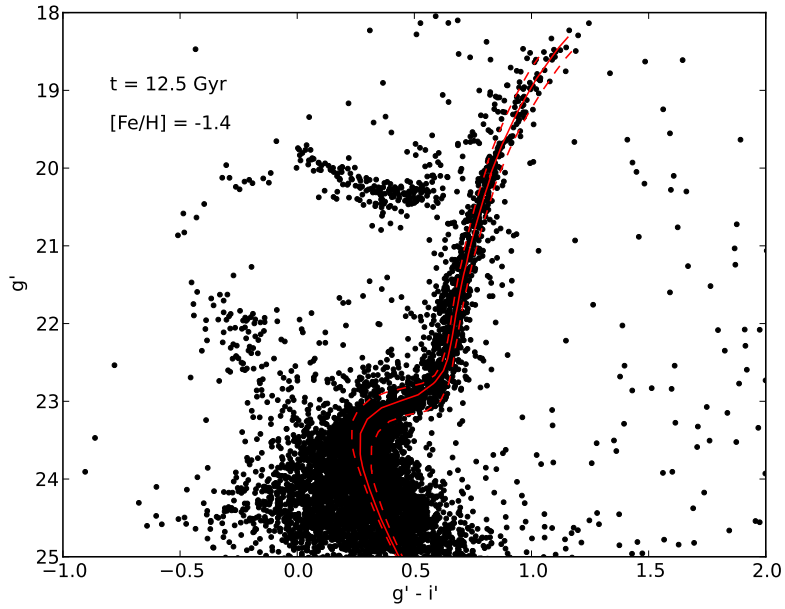

Figure 4.7 Color-magnitude diagram of stars within the central 5′of Draco. From left to right, we plot isochrones of $(t_{age} \times 10^9 \mathrm{yr}, [\mathrm{Fe/H}]) = (11.5, -1.6)$, $(12.5, -1.4)$, and $(13.5, -1.3)$. The solid red line is the $(12.5, -1.4)$ isochrone we use when determining M_*/L_V.

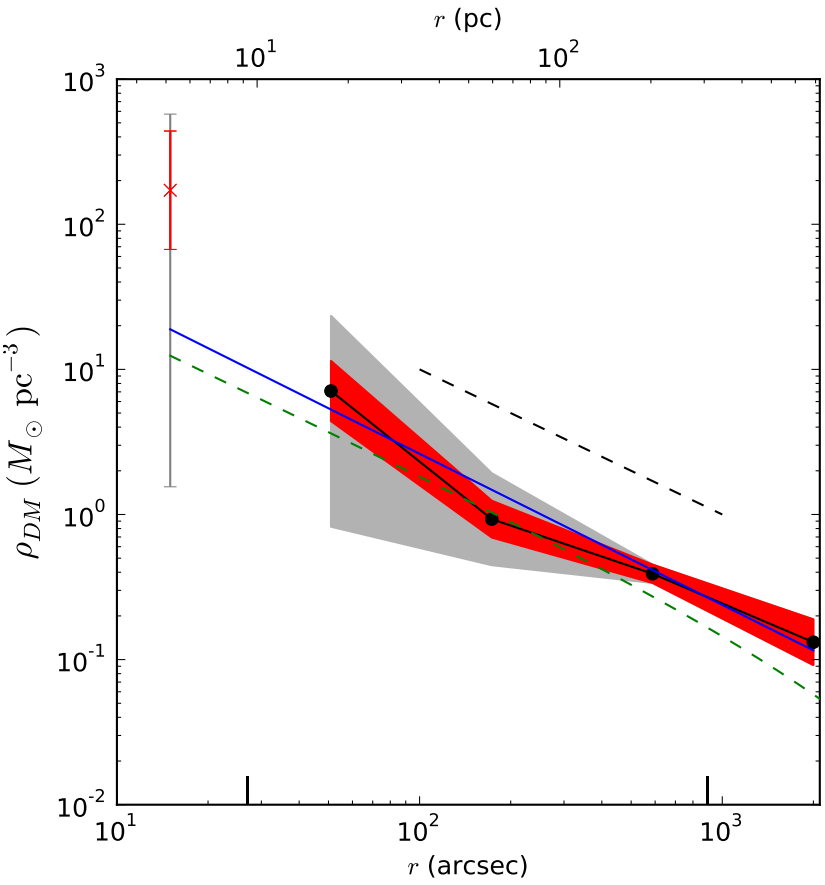

Figure 4.8 Best-fitting dark matter density profile in Draco. The red shaded region represents the point-wise 68% confidence band for $\rho_{DM}(r)$ ($\Delta\chi^2 = 1$), with the solid black line derived from forcing symmetric logarithmic errors. The gray shaded region is the 68% confidence band on $\rho_{DM}(r)$ considering all parameters jointly ($\Delta\chi^2 = 7.04$). We plot the innermost point (excluded from all futher analysis) an an error bar with the same color scheme. The solid blue line is the best power law fit to the profile, and the dashed line shows an r^{-1} NFW-like profile. We plot the best-fitting NFW halo from a small grid of parametric models as the dashed green line. Vertical lines along the x-axis indicate the radial range of our kinematic data.

value indicates a large central density and a departure from the power-law nature of the outer profile. Further puzzling is that its point-wise uncertainty (plotted as a red error bar) indicates strong constraint despite the fact that we have no kinematic data in this region of the galaxy. We speculate that, in the absence of such data, models are able to arbitrarily increase the central density. Since the volume of this inner bin is small, the total amount of mass added is negligible. With no kinematics in this region, models can easily absorb this mass without affecting χ^2. We therefore exclude the innermost point in all further analysis.

The resulting power law fit to the outer four points is shown in blue in Figure 4.8. We characterize the uncertainty in this fit by constructing 1,000 Monte Carlo realizations with noise added to the density profile. We draw each point *i* randomly from a Gaussian distribution with mean $\log \rho_i$ and dispersion given by the width of the 1σ confidence band at point *i* in Figure 4.8. We repeat the fit for each realization, and determine the 1σ uncertainties on α from the 68% span of this distribution. This procedure yields $\alpha = -1.0 \pm 0.2$. None of the 1,000 realizations has a slope $\alpha > -0.45$ strongly indicating that the galaxy is not cored for $r \gtrsim 20$ pc.

4.4.3 Orbit Structure

Once we have determined the best-fitting model, we can calculate the internal (unprojected) moments of the distribution function at each of the bins in our meridional grid. Of interest is the anisotropy in the velocity dispersion tensor, which we quantify with the ratio σ_r/σ_t—the ratio of radial to tangential anisotropy in the galaxy. We define the tangential anisotropy σ_t as

$$\sigma_t \equiv \sqrt{\frac{1}{2}(\sigma_\theta^2 + \sigma_\phi^2 + v_\phi^2)} \tag{4.5}$$

in spherical polar coordinates where v_ϕ is the rotational velocity. Streaming motions in the r and θ directions are assumed to be zero. We plot σ_r/σ_t in Figure 6.5. Since the LOSVDs we use in Draco contain contributions from stars at all angles θ, we average σ_r and all quantities in Equation (4.5) when calculating σ_r/σ_t. Consequently, we lose the ability to evaluate anisotropy as a function of θ. This can be avoided if better kinematics coverage is available, either through more stars with radial velocities in dSphs or two-dimensional integral-field spectroscopy in more distant galaxies. Fortunately most other large dSphs in the Local Group have many more radial velocities publicly available.

We plot σ_r/σ_t in Figure 6.5 over the radial range that our LOSVDs sample. We determine the uncertainties in σ_r/σ_t by the maximum/minimum values of σ_r/σ_t for models within $\Delta\chi^2 = 7.04$ of $\chi^2_{\rm min}$ (1σ for $N_{\rm bin}$+1 degrees of freedom).We find evidence for radial anisotropy at all radii, consistent with the "tidal stirring" theory describing the origin of the Milky Way dSphs (Łokas et al., 2010; Kazantzidis et al., 2011). Uncertainties are large on σ_r/σ_t, likely due to the small number of radial velocities available as kinematic constraint. To constrain the anisotropy better, more radial velocities are needed.

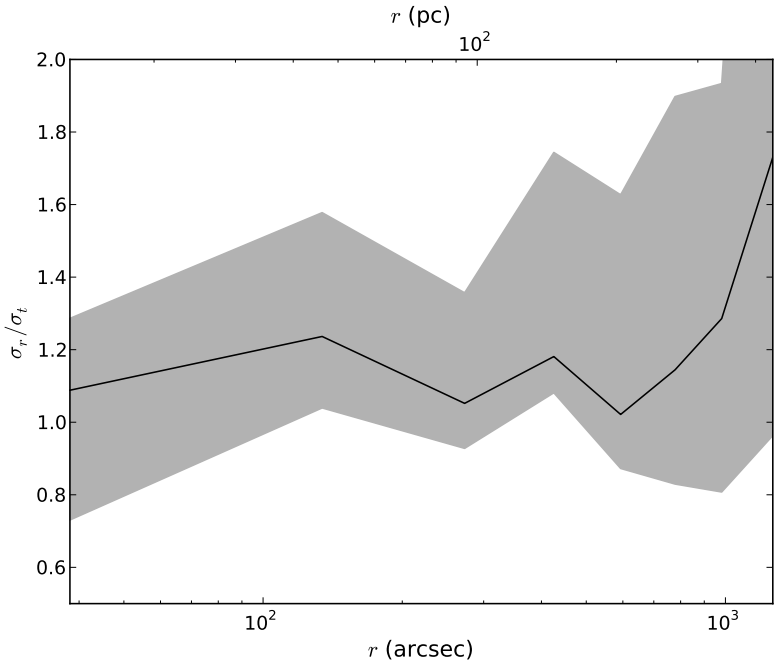

Figure 4.9 Ratio of the radial to tangential components of the velocity dispersion. Values of σ_r/σ_t different from unity indicate anisotropy. The black line is our best-fitting model.

4.5 Discussion

4.5.1 Improvement over Parametric Methods

Since we eventually fit our non-parametric dark matter profile with a power law, one can ask why we do not initially use a power law-parameterized profile. This would seem advantageous, especially given the large parameter space required by non-parametric methods. This reasoning, however, relies on the assumption that we know the profile is a power law a priori. The point of this study is to relax this assumption and see what type of profile comes out of the modeling, rather than impose unjustified interpretation on the problem. It happens that Draco hosts a nearly power law density profile, but by not assuming this a priori we allow more general models to be explored. As a rough check that our models have converged to a global minimum, we run a small grid of parametric models with an NFW dark matter density profile. The best-fitting of these models is plotted in green in Figure 4.8.

4.5.2 Interpreting the Dark Matter Profile

It is important to note that we only constrain the dark matter density profile over little more than a decade in radius from $20-700$ pc. One could easily imagine our power law fit changing from $\alpha = -1$ to a core ($\alpha = 0$) inside of $r \sim 20$ pc. Likewise, the slope may also change at larger radii than $r \sim 700$ pc without our knowledge. The NFW density profile has an outer slope $\alpha = -3$ for $r \gg r_s$, but our profile does not change slope within our model grid. This could indicate that $r_s \gg 700$ pc, but without knowledge of the outer slope we cannot say with certainty

that the profile is NFW-like.

Recent cosmological N-body simulations have been found to produce density profiles shallower than the traditional $\alpha = -1$ cusps (Stadel et al., 2009; Navarro et al., 2010). Many authors suggest that dark matter profiles are best parameterized by the Einasto profile (Navarro et al., 2004; Merritt et al., 2005; Gao et al., 2008; Navarro et al., 2010) where the slope varies with radius according to a power law $\alpha(r) \propto r^n$. These profiles can have shallower cusps than NFW, but do not have constant slopes over a large range in radius. Our non-parametric density profile is well-fit by a single power law from $20 \lesssim r \lesssim 700$ pc, but, again, this is a fairly narrow range in radius. Our models cannot rule out an Einasto-like change in slope outside this radial range. More kinematics are needed to characterize the density profile at large and small radii.

When calculating the potential, we allow the outer slope of $\rho(r)$ to vary between $2 \leq \alpha_\infty \leq 4$ for $r > 700$ pc, but, unsurprisingly, we are unable to constrain α_∞. Tidal effects may also alter the shape of $\rho_{DM}(r)$ since Draco is orbiting within the dark matter halo of the Milky Way. The tidal radius calculated from Equation (4.4) is sufficiently large that tides are unlikely to affect the stellar component, but $\rho_{DM}(r)$ at large radii could be affected. If this is the case, $\rho_{DM}(r)$ would decline more steeply than expected and the total mass enclosed would be smaller than what we calculate.

The cuspy $\alpha = -1$ dark matter profile we find in Draco stands in contrast to many other observational studies of dSphs that find $\alpha = 0$ cores (Gilmore et al., 2007; Walker & Peñarrubia, 2011; Jardel & Gebhardt, 2012). The effects of baryons

are still not well-understood, and could potentially drive α to different values on a galaxy-by-galaxy basis. These effects are the sum of at least two competing processes. Adiabatic compression (Blumenthal et al., 1986) draws in dark matter boosting the central ρ_{DM} and driving α to more negative values. On the other hand, feedback from star formation and supernovae can cause strong outflows (Navarro et al., 1996a; Binney et al., 2001) which can in turn remove dark matter from the centers of galaxies, reshaping cuspy profiles into $\alpha = 0$ cores.

In a recent paper, Governato et al. (2012) use high resolution cosmological N-body simulations with a fully hydrodynamical treatment of baryons to test these two competing effects in low-mass dwarf galaxies. They find that the cuspiness of the dark matter halo is directly related to the amount of star formation activity in the galaxy. This is expressed as a correlation between α and stellar mass M_*. Their interpretation is that galaxies that form more stars (larger M_*) have more supernovae and a greater potential to turn a cuspy dark matter profile into a core. Using their least-squares fit to the M_*-α correlation, they predict $\alpha \approx -1.3$ (at 500 pc) for Draco's stellar mass. This is in approximate agreement with our measured value of $\alpha = -1$.

Perhaps owing to the lack of stellar velocities available in Draco compared to other dSphs, there are not many studies investigating its dark matter profile through dynamical models. A rough comparison can be made with Łokas et al. (2005) who fit profiles with an inner slope of $\alpha = -1$ and an outer exponential cutoff at large radii. They find a total mass-to-light ratio that varies with radius between $100 \gtrsim M_{\rm tot}/L_V \gtrsim 1000$ in the inner ~ 700 pc. These values are comparable to the

total mass-to-light ratio we calculate in the inner ~ 300 pc. However, unlike Łokas et al. (2005) we do not impose an exponential cutoff in $\rho_{DM}(r)$ at large radii. Our calculated $M_{\rm tot}/L_V$ therefore rises sharply at large radii where the stellar luminosity profile is decreasing much faster than $\rho_{DM}(r)$.

Importantly, $M_{\rm tot}/L_V \gg M_*/L_V = 2.9 \pm 0.6$ (the stellar mass-to-light ratio we derive from SSP models) at all radii. This means we can confidently state that Draco is dark matter-dominated at all radii, allowing us to easily absorb errors in M_*/L_V from SSP models. In other words, when determining $\rho_{DM}(r)$ from Equation (1) the uncertainty in $\rho(r)$ dominates the uncertainty in stellar density since the product $M_*/L \times \nu(r)$ is much smaller than $\rho(r)$. This is one of the reasons we choose to test this non-parametric technique on Draco first. In the future we plan to extend this analysis to the remaining Local Group dSphs, which are also thought to be dark matter-dominated everywhere.

4.5.3 Draco's Mass

We plot the enclosed mass profile of our models in Figure 4.10. The shaded region is the 1σ confidence band derived from the extreme values of $M(r)$ for all models within $\Delta\chi^2 = 5.84$ of the minimum (1σ for $N_{\rm bin}= 5$ free parameters, marginalizing over α_∞). The vertical ticks on the x-axis represent the radial extent of our kinematics coverage. From this plot it is apparent that, despite its low luminosity and stellar mass, Draco lives in a dark matter halo that is surprisingly massive.

An interesting comparison can be made with the brightest dSph Fornax,

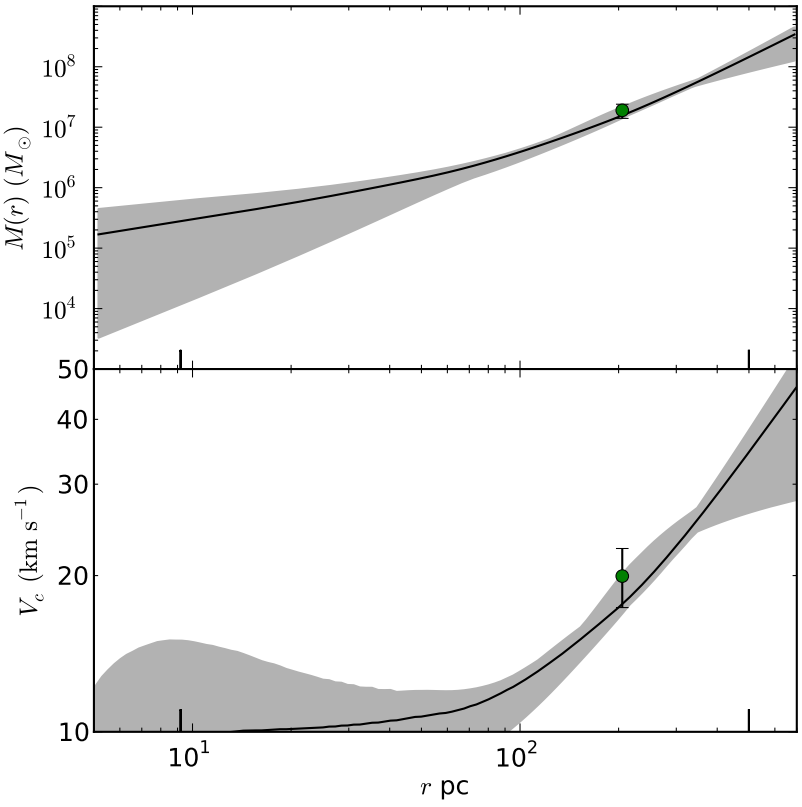

Figure 4.10 (Top): Enclosed Mass profile of our best-fitting model (black line) and 1σ confidence region. The green point is the Wolf et al. (2010) mass estimator. (Bottom): Circular speed profile and 1σ confidence region. Colors are the same as above. Vertical tick marks on the x-axis represent the range of our kinematics coverage.

roughly two orders of magnitude higher in luminosity. If we compare the mass enclosed within a common physical radius of 300 pc, we find that for Draco $M_{300} \equiv M(r = 300 \text{ pc}) = 3.8^{+0.84}_{-0.29} \times 10^7 M_\odot$, and Jardel & Gebhardt (2012) measure $M_{300} = 3.5^{+0.77}_{-0.11} \times 10^6 M_\odot$ for Fornax. Of course, Fornax is much more extended than Draco so it is sensible to also compare the mass enclosed within the deprojected half-light radius of each galaxy's stellar component. For Draco we measure $M_{1/2} \equiv M(r = r_e) = 1.6^{+0.6}_{-0.2} \times 10^7 M_\odot$, and in Fornax Jardel & Gebhardt (2012) measure $M_{1/2} = 5.8^{+1.0}_{-0.2} \times 10^7 M_\odot$. We would prefer to compare the total mass of each galaxy, but there are no kinematic tracers far enough out in the halo that the density profile declines sharply enough to keep mass finite for any dSph. Consequently, we cannot constrain the total mass observationally and we must rely on comparions to simulations (Section 5.4).

We also use our dynamical models to compare our measurement of $M_{1/2}$ with the convenient mass estimator proposed by Wolf et al. (2010) (see Walker et al. 2009b and Cappellari et al. 2006 for similar formulae). This formula relates $M_{1/2}$ to the directly observable luminosity-weighted line-of-sight velocity dispersion $< \sigma^2_{LOS} >$ and projected half-light radius R_e. The Wolf et al. (2010) mass estimator is written as:

$$M_{1/2} \approx 4G^{-1} R_e < \sigma^2_{LOS} > \tag{4.6}$$

and Wolf et al. (2010) give a theoretical argument for why the effect of anisotropy is minimized near r_e for a variety of stellar systems in spherical symmetry.

For a more fair comparison of Equation (4.6) to our models we calculate $M_{1/2}$ from our data set, not the value listed in Wolf et al. (2010). We use $< \sigma^2_{LOS} >= 11.3 \pm 1.6$ km s^{-1}, calculated directly from our data in Figure 6.2, as well as R_e = 158.1 pc and r_e = 205.2 pc which we derive from the photometry in Figure 6.1. This calculation yields an estimated $M_{1/2} = (1.9 \pm 0.5) \times 10^7 M_\odot$, in excellent agreement with the mass calculated from our models. We plot the estimated $M_{1/2}$ as the green point in Figure 4.10.

4.5.4 Comparing Draco to CDM Simulations

We can also gain insight into the properties of Draco's dark matter halo by examining the circular speed profile $V_c(r)$ plotted in the lower panel of Figure 4.10 . The green point plotted is $V_{1/2} = \sqrt{GM_{1/2}/r_{1/2}} = 20.0 \pm 2.6$ km s^{-1}using our value of the Wolf et al. (2010) mass estimator. In a recent paper, Boylan-Kolchin et al. (2012) match the observed $V_{1/2}$ of Local Group dSphs to subhalos around a Milky Way-like halo in the Aquarius Simulation (Springel et al., 2008) to derive constraints on each dSph's maximum circular speed $V_{\rm max}$—a quantity directly related to the total halo mass. Boylan-Kolchin et al. (2012) find that this estimate of $V_{\rm max}$ is usually $20-30$ km s^{-1} smaller than the $V_{\rm max}$ they obtain through abundance matching. These results lead them to conclude that the Local Group dSphs are dynamically inconsistent with the types of halos they are predicted to inhabit from abundance matching.

We are in a position to investigate this claim directly in Draco. We do not need to match our $V_{1/2}$ to simulations in order to gain knowledge of $V_c(r)$; we cal-

culate the latter directly, and not just at the half-light radius. Interestingly, much of our circular speed profile lies above the $V_{\rm max} = 20.5^{+4.8}_{-3.9}$ predicted by Boylan-Kolchin et al. (2012). At $r = 500$ pc, the radius where we run out of kinematic tracers and can therefore no longer robustly constrain the mass, we find $V_c = 34.6^{+3.5}_{-8.2}$ km s^{-1}. We can take the lower bound of V_c here as lower limit on $V_{\rm max} \geq 26.4$. The scaling relations between total mass and $V_{\rm max}$ for subhalos (Springel et al., 2008) imply a lower limit on Draco's total mass of $M \geq 1.0 \times 10^9 M_\odot$.

Ours is not the first study to suggest that Draco lives in a halo with such a large mass. Peñarrubia et al. (2008) demonstrate that a family of NFW halos with varying $V_{\rm max}$ and $r_{\rm max}$ are consistent with the stellar kinematics of any King model embedded in an NFW halo. They break this degeneracy by invoking the correlation between $V_{\rm max}$ and $r_{\rm max}$ found in CDM simulations (e.g. Bullock et al. 2001). Their study suggests that Draco is the most massive of the Milky Way dSphs with $V_{\rm max} \approx 35$ km s^{-1}.

The comparison between Draco and Fornax is interesting as the two galaxies are separated by almost two orders of magnitude in luminosity but may have similar masses. Since Draco's inner halo is nicely fit by the NFW density profile (Figure 4.8), we can rely on simulations to extrapolate a total mass $M \geq 1.0 \times 10^9 M_\odot$. However, multiple independent studies using different methods suggest that Fornax does not live in an NFW halo (Goerdt et al., 2006; Walker & Peñarrubia, 2011; Jardel & Gebhardt, 2012), and we therefore should not use the NFW formalism to predict a total mass from its $V_{\rm max}$. Still, the similarity in the galaxies' values of $M_{1/2}$ and M_{300} suggests that the simplest abundance matching models, which require

a one-to-one mapping between luminosity and total mass, may not appropriately describe the dSphs. If Draco and Fornax do indeed have similar masses, despite vastly different baryonic properties, then there must be substantial stochasticity in the galaxy formation process at the dSph mass scale. Even without comparing to Fornax, it is clear that Draco's baryonic properties do not map in the expected way to its halo mass.

K.G. acknowledges support from NSF-0908639. We thank Dave Doss and the staff at McDonald Observatory for observing support. We gratefully acknowledge fruitful discussions with Louis Strigari, Remco van den Bosch, Glenn van de Ven, and Andrea Maccio. This work would not be possible without the state-of-the-art computing facilities available at the Texas Advanced Computing Center (TACC).

Chapter 5

Variations in a Universal Dark Matter Profile for Dwarf Spheroidals[1]

As full and bright as I am
This light is not my own and
A million light reflections pass over me.

Its source is bright and endless
She resuscitates the hopeless
Without her, we are lifeless *satellites* drifting

Maynard James Keenan - "Reflection"

Using a newly-developed modeling technique, we present orbit-based dynamical models of the Carina, Draco, Fornax, Sculptor, and Sextans dwarf spheroidal (dSph) galaxies. These models calculate the dark matter profiles non-parametrically without requiring any assumptions to be made about their profile shapes. By lifting this restriction we discover a host of dark matter profiles in the dSphs that are different from the typical profiles suggested by both theorists and observers. However, when we scale these profiles appropriately and plot them on a common axis they appear to follow an approximate r^{-1} power law with considerable scatter.

[1]Published in Jardel J., R., & Gebhardt, K., 2013, ApJL, 775, 30. Reprinted with permission from the American Astronomical Society.

5.1 Introduction

It is a well known fact that cosmological simulations containing only collisionless dark matter produce halos that share a universal density profile $\rho_{\rm DM}(r)$ (Navarro et al., 1996b; Springel et al., 2008; Navarro et al., 2010). At first, this universal profile was characterized by the double power-law Navarro-Frenk-White (NFW) profile (Navarro et al., 1996b) with (negative) inner logarithmic slope $\alpha = 1$. Modern dark matter-only simulations with increasingly better resolution seem to produce profiles that, in analogy to the Sérsic function (Sersic, 1968), transition smoothly from $\alpha = 3$ in the outer regions to $\alpha \sim 1$ near the center (Merritt et al., 2005; Gao et al., 2008; Navarro et al., 2010). The exact form of $\rho_{\rm DM}(r)$ is still debated by theorists, but most agree that the inner slope is nonzero. Such profiles are called "cuspy" since $\rho_{\rm DM}$ increases as $r \to 0$. In contrast, observers modeling low-mass galaxies with stellar and gas dynamics often find $\alpha = 0$ "cores" in the inner profiles (Burkert, 1995; Persic et al., 1996; Borriello & Salucci, 2001; de Blok et al., 2001; Simon et al., 2005). This disagreement between theory and observations has become known as the core/cusp debate.

We must remember, however, that real galaxies are the products of their unique formation histories, and complex baryonic processes can re-shape dark matter profiles in different ways. Whether originating from adiabatic compression (Blumenthal et al., 1986), supernovae winds (Navarro et al., 1996a), or ram-pressure stripping (Arraki et al., 2012), baryonic feedback has been shown to affect the dark matter profiles of galaxies by perturbing their baryons in a highly non-linear way. Since these processes differ on a galaxy-by-galaxy basis, one should not expect to

observe a universal dark matter profile at $z = 0$. Furthermore, given the number of different ways baryonic feedback can occur, we should not expect it to produce only cored or NFW-like profiles.

Unfortunately, it is difficult to explore the possible range of profile shapes since to construct a dynamical model one generally needs to adopt a parameterization for $\rho_{\rm DM}(r)$. This is not ideal as one is forced to assume the very thing they are hoping to measure. Clearly methods that can measure $\rho_{\rm DM}(r)$ non-parametrically are advantageous. Non-parametric determination of the dark matter profile avoids biasing results by assuming an incorrect parameterization and it also allows more general profile types to be discovered.

To test the universal profile assumption, we apply the technique of non-parametric Schwarzschild modeling to determine $\rho_{\rm DM}(r)$ in five of the brightest dwarf spheroidal (dSph) galaxies that orbit the Milky Way as satellites. These galaxies have excellent kinematics available (Walker et al., 2009a) and have been demonstrated to be good targets for this type of modeling (Jardel et al., 2013). The dSphs as a population are some of the most dark matter-dominated galaxies ever observed (Mateo, 1998; Simon & Geha, 2007) and as such are unique test sites for theories of galaxy formation at low mass scales.

Past studies using Jeans models have had difficulty robustly measuring $\rho_{\rm DM}(r)$ in the dSphs (Walker et al., 2009b) largely due to the degeneracy between mass and velocity anisotropy inherent to these models. In addition to being fully non-parametric, our models break the degeneracy between mass and velocity anisotropy the same way traditional Schwarzschild models accomplish this (Gebhardt et al.,

2000a; Rix et al., 1997; van der Marel et al., 1998; Valluri et al., 2004; van den Bosch et al., 2008). In this letter we apply the most general models to a widely-studied group of galaxies in order to measure their dark mater density profiles and test the universal profile hypothesis.

5.2 Data

Our models use the publicly available kinematics data from Walker et al. (2009a) for Carina, Fornax, Sculptor and Sextans. These data are individual radial velocities for member stars with repeat observations weighted and averaged. Walker et al. (2009a) assign each star a membership probability P based on its position, velocity, and a proxy for its metallicity. Our analysis only includes stars for which $P > 0.95$. Whenever a galaxy has high-quality *Hubble Space Telescope* measurements of its proper motion available (Carina and Fornax; Piatek et al. 2003, 2007) we correct for the effects of perspective rotation following Appendix A of Walker et al. (2008).

As described in Jardel & Gebhardt (2012), stars are placed on a meridional grid according to their positions and folded over the major and minor axes. To preserve any possible rotation, we switch the sign of the velocity whenever a star is flipped about the minor axis. We then group the stars into spatial bins by dividing the grid into a series of annular bins containing roughly 50-70 stars per bin. Fornax and Sculptor have a larger number of stars with measured velocities, and to exploit this we subdivide the annular bins into two to three angular bins in analogy to spokes on a wheel. Table 5.1 presents a summary of the data we use for the dSphs.

For each spatial bin of stars, we reconstruct the full line-of-sight velocity distribution (LOSVD) from the discrete radial velocities observed. This procedure uses an adaptive kernel density estimator (Silverman, 1986) and is described in more detail in Jardel et al. (2013). Uncertainties in the LOSVDs are determined through bootstrap resamplings of the data. We divide each LOSVD into 15 velocity bins which serve as the observational constraint for our models.

Also necessary for the models is the galaxy's three-dimensional luminosity density profile $\nu(r)$. To obtain this, we start with the projected number density profile of stars $\Sigma_*(R)$. For Carina and Sculptor we take $\Sigma_*(R)$ from Walcher et al. (2003), opting to use their fitted King profile for Carina and the actual profile for Sculptor with no fit performed. We also use a King profile to describe $\Sigma_*(R)$ in Sextans, with the parameters taken from Irwin & Hatzidimitriou (1995). In Fornax we use the full profile reported in Coleman et al. (2005). We then convert $\Sigma_*(R)$ to a surface brightness profile $\mu(R)$ by adding an arbitrary zero-point shift, in log space, and adjusting the shift until the integrated $\mu(R)$ returns a luminosity consistent with the value listed in Mateo (1998).

Next we deproject $\mu(R)$ via Abel inversion through the manner described in Gebhardt et al. (1996). For simplicity in the deprojection and subsequent modeling, we assume that each galaxy is viewed edge-on. For a thorough discussion on how uncertainties in viewing angle and geometry propagate through our models we refer the reader to Thomas et al. (2007a). Our models are axisymmetric, so we use the stellar ellipticity to determine ν away from the major axis.

Table 5.1. Properties of the Dwarf Spheroidals

Galaxy	Distance (kpc)	$N_{\rm stars}$	$N_{\rm LOSVD}$	Ellipticity	$R_{\rm trunc}$ (kpc)
Carina	104[a]	702[f]	14	0.33[e]	4.2
Draco	71[b]	170[gh]	8	0.29[e]	3.1
Fornax	136[a]	2409[f]	36	0.30[e]	13.5
Sculptor	85[c]	1266[f]	24	0.32[e]	5.1
Sextans	85[d]	388[f]	8	0.35[e]	5.1

Note. — Summary of the data we use for our study of the dSphs. We list the distances to the dSphs we have assumed, the number of member stars with radial velocity measurements $N_{\rm stars}$, and the number of LOSVDs these measurements are divided into $N_{\rm LOSVD}$. We assume the the dark matter halo has the same ellipticity as the value listed for the stellar component. We also list the truncation radius $R_{\rm trunc}$ used in our analysis. References: [a]Tammann et al. (2008), [b]Odenkirchen et al. (2001), [c]Pietrzyński et al. (2008), [d]Lee et al. (2009), [e]Irwin & Hatzidimitriou (1995), [f]Walker et al. (2009a), [g]Kleyna et al. (2002), [h]Jardel et al. (2013).

5.3 Models

The non-parametric modeling technique we use is described in full detail in Jardel et al. (2013). It is based on the Schwarzschild modeling code of Gebhardt et al. (2000a) updated by Thomas et al. (2004, 2005) and described in Siopis et al. (2009). We have tested our models by using kinematics generated from a Draco-sized mock dSph embedded in a larger dark matter halo with either a cored or NFW-like cuspy profile. In both cases we are able to accurately recover the density profile from which the mock kinematics were drawn.

The fundamental principle behind Schwarzschild modeling, that of orbit superposition, was first introduced by Schwarzschild (1979). The Schwarzschild code that is the backbone of our non-parametric technique has been thoroughly tested using artificial data. It has been shown to accurately recover the mass profile and orbit structure of simple isotropic rotators (Thomas et al., 2005), *N*-body merger remnants (Thomas et al., 2007a), and a mock galaxy containing a supermassive black hole (Siopis et al., 2009). The general Schwarzschild technique has also been tested with artificial data representing the binned individual velocities typically used as input for studying the dSphs (Breddels et al., 2013).

This method works by assuming a trial potential for the galaxy under study and determining all stellar orbits that are possible in that potential. Our orbit sampling scheme is described in detail in Thomas et al. (2004). The orbits are then assigned weights according to how well they match the LOSVDs and a χ^2 value is determined, subject to a constraint of maximum entropy (Siopis et al., 2009). If χ^2 is low, the orbits are a good fit to the kinematics and the trial potential is considered

to be a good estimate for the real potential. If χ^2 is large, the trial potential does not support orbits that can match the kinematics and a new potential is generated. Each model is required to match $\nu(r)$ as well to machine precision.

We construct the many trial potentials by solving Poisson's equation for a specified total density profile $\rho(r)$ along the major axis. We assume the total mass distribution has the same ellipticity as the stellar component and use this adopted ellipticity to define $\rho(r,\theta)$ away from the major axis.

Rather than paramaterizing $\rho(r)$ with an unknown function and sampling its parameters, we take an altogether different approach (detailed in Jardel et al. 2013). To describe $\rho(r)$ we divide the profile into 5 radial points r_i, equally spaced in $\log r$. A trial $\rho(r)$ is then represented by the density ρ_i at each point. In this way, the ρ_i themselves are the parameters that we adjust when picking trial potentials. To sample this parameter space, we employ a similar iterative refinement scheme as discussed in Jardel et al. (2013). We also impose the same constraint that each profile must be non-increasing as a function of radius.

Since the dSphs orbit within the Milky Way's halo, the possibility exists that they are being, or have been, tidally stripped. In constructing our trial potential, we account for this by leaving the slope of $\rho(r)$ outside of our model grid a free parameter α_∞. Each model profile $\rho(r)$ is run with $\alpha_\infty \in \{2,3,4\}$. In this way, we treat α_∞ as a nuisance parameter and marginalize over it for the rest of our discussion. We also truncate the dSphs at the radius $R_{\rm trunc}$ defined by the Jacobi radius given the mass of the dSph, its Galactocentric distance, and the mass of the Milky Way (assumed to be $M_{\rm MW} = 3 \times 10^{12} M_\odot$ and represented by an isothermal

sphere). We list values for $R_{\rm trunc}$ in Table 5.1.

5.3.1 Stellar Density

After running a large number of models for each galaxy, we have a non-parametric measurement of the *total* density profile $\rho(r)$. In order to obtain the dark matter density profile we must subtract the stellar density $\rho_*(r)$. This requires knowledge of the stellar mass-to-light ratio M_*/L_V since $\rho_*(r) = M_*/L_V \times \nu(r)$, assuming that variations in M/L_I with radius are unimportant.

To estimate M/L_I we use photometrically derived determinations of each galaxy's stellar age $t_{\rm age}$ and metallicity [Fe/H] (Lianou et al., 2011). The simple stellar population models of Maraston (2005) then yield an estimate on M/L_I given these two quantities and the assumption of either a Salpeter or Kroupa initial mass function (IMF). We characterize the uncertainty in $\rho_*(r)$ by the spread in values of M/L_I that result from a choice in IMF and the uncertainties in $t_{\rm age}$ and [Fe/H]. For our analysis of $\rho_{\rm DM}(r)$, we add in quadrature the uncertainties on $\rho(r)$ from the models with those on ρ_* due to M/L_I.

In all but one of the dSphs (Fornax), $\rho(r) \gg \rho_*(r)$ making the determination of $\rho_*(r)$ relatively unimportant. In Fornax, however, the relatively large uncertainties on $\rho_*(r)$ make $\rho(r) - \rho_*(r)$ a negative quantity in some cases. This is clearly unphysical as it represents a negative dark matter density. To better study Fornax and other relatively baryon-dominated galaxies, a more accurate determination of M/L_I is required.

5.3.2 χ^2 Analysis

We evaluate the goodness of fit of each model with χ^2 as calculated by

$$\chi^2 = \sum_{i=1}^{N_{\rm LOSVD}} \sum_{j=1}^{N_{\rm vel}=15} \left(\frac{\ell_{ij}^{\rm obs} - \ell_{ij}^{\rm mod}}{\sigma_{ij}} \right)^2 , \tag{5.1}$$

where the sums are computed over the $N_{\rm vel} = 15$ velocity bins for all of the LOSVDs in each galaxy. The ℓ_{ij} correspond to the value in the jth velocity bin of the ith LOSVD. The uncertainty in $\ell_{ij}^{\rm obs}$ is σ_{ij}.

We identify the best-fitting model as that which has the lowest value of the (unreduced) $\chi^2 = \chi^2_{\rm min}$. A naïve calculation of the reduced $\chi^2_\nu = \chi^2_{\rm min}/(N_{\rm vel} \times N_{\rm LOSVD})$ often yields values much less than unity due to correlation between velocity bins caused by our kernel density estimator. We instead test for the overall goodness of fit of our best model by computing $\chi^2_{\nu,GH}$: the reduced χ^2 with respect to a Gauss-Hermite parameterization of our best-fitting LOSVDs. We find $\chi^2_{\nu,GH}$ ranges from $0.3-0.9$ for the four dSphs modeled here. These values are consistent with past results (Gebhardt et al., 2003; Gebhardt & Thomas, 2009; Jardel et al., 2013) and have been demonstrated to lead to accurate recovery of the mass profiles of mock galaxies (Thomas et al., 2005). We therefore scale our model-computed unreduced χ^2 values by a factor equal to $\chi^2_\nu/\chi^2_{\nu,GH}$ in order to bring our reduced χ^2_ν nearer to $\chi^2_{\nu,GH}$.

We present our dark matter profiles at two different levels of confidence. When specifying the dark matter density at a single point, we marginalize over all other parameters using the sliding boxcar technique described in Jardel et al.

(2013) to interpolate χ^2. The 1σ confidence interval thus corresponds to a limit of $\Delta\chi^2 = 1$ (for one degree of freedom) above $\chi^2_{\rm min}$. When referring to the joint 1σ confidence interval of the entire profile, we instead include limits derived from all models within $\Delta\chi^2 = 5.84$ of $\chi^2_{\rm min}$ (for 5 degrees of freedom).

5.4 Results

We present the non-parametrically determined dark matter profiles in Figure 5.1. In addition to the new results for Carina, Fornax, Sculptor, and Sextans, we include the result from Jardel et al. (2013) for Draco. Each panel in Figure 5.1 contains a dashed line with $\rho_{\rm DM} \propto r^{-1}$ to show the generic shape of the NFW profile. The points with error bars in Figure 5.1 are the marginalized dark matter density determined from $\Delta\chi^2 = 1$ at the r_i where the total density is being varied from model to model. The gray points labeled with X's are located interior to the radial range over which stellar kinematics are available. We denote this range for each galaxy with vertical tick marks on the x-axis. The joint confidence band (shaded region) interpolates between the r_i by taking the maximum and minimum value for $\rho_{\rm DM}$ at each radius for every model within $\Delta\chi^2 = 5.84$ of $\chi^2_{\rm min}$.

Given the freedom to choose a dark matter profile of any shape, it is immediately apparent that our models have chosen a variety of shapes for the dSphs. Draco appears the most similar to the NFW profile while Sculptor most closely resembles a broken powerlaw that becomes shallower towards its center. The other galaxies host profiles that resemble neither cores nor cusps: Carina's profile appears flat where we have kinematics but then displays a possible up-bending inside of this

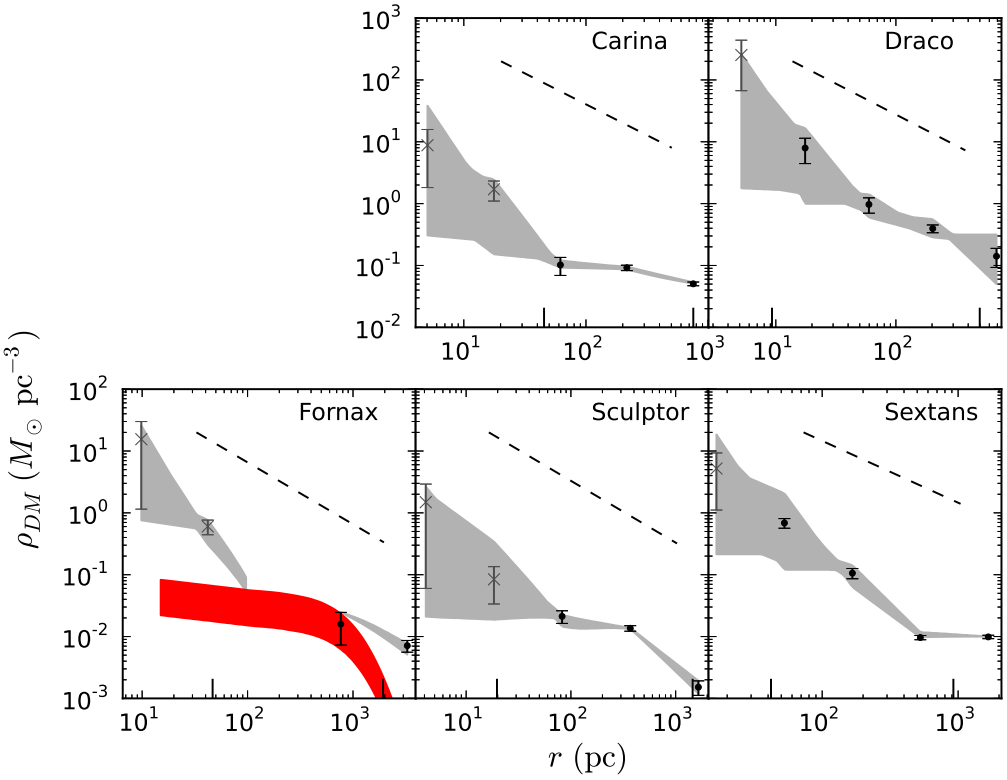

Figure 5.1 Dark matter density profiles for each dSph modeled as well as Draco from Jardel et al. (2013). Points with error bars show the $\Delta\chi^2 = 1$ uncertainties in the ρ_i. These points are gray X's when they lie interior to the our kinematics and black dots otherwise. Vertical black tick marks on the x-axes show the radial extent of this range. The gray shaded regions show the joint confidence range of the entire profile at the level of $\Delta\chi^2 = 5.84$ and interpolated between the ρ_i. Each panel plots a generic r^{-1} NFW-like profile as a dashed line. In Fornax we also plot the stellar density profile $\rho_*(r)$ with 1σ uncertainties in red.

region. Sextans has a steeper slope than the NFW profile until its outermost point where it suddenly becomes flat. These sharp differences among dSph dark matter profiles demonstrate the variety of profile shapes in the Local Group.

Unfortunately, due to a lack of central stellar velocities in the Walker et al. (2009a) data, the central profiles of the dSphs we model become increasingly uncertain there. This is evidenced by the larger error bars on our gray points in Figure 5.1 where we have no kinematics coverage. However, we do have some constraint from projection effects and radial orbits in our models that have apocenters at radii where we do have data.

5.4.1 Fornax

Fornax is an especially difficult case for non-parametric modeling because, compared to the other dSphs, it is relatively baryon-dominated. Our imprecise determination of M/L_I in Fornax causes $\rho_*(r)$ to be greater than the total modeled density at some radii, making $\rho_{\rm DM}(r)$ negative. In our analysis of Fornax, we do not plot the radial range over which this occurs as it is unphysical. Instead in Figure 5.1 we over-plot the stellar density in red to illustrate why the subtraction is difficult in Fornax. In all other panels $\rho_*(r) \ll \rho_{\rm DM}(r)$ and is not plotted.

There is strong evidence from multiple studies using independent methods that suggests Fornax has a dark matter profile that is not cuspy like the NFW profile. (Goerdt et al., 2006; Walker & Peñarrubia, 2011; Jardel & Gebhardt, 2012). Each of these studies only contrasts between cored and cuspy profiles or uses a single slope to characterize the profile. It is therefore interesting to explore the non-parametric

result we obtain. Even though we cannot determine ρ_{DM} where the stellar density is greater than the total density, we can still place an upper limit on ρ_{DM} such that it must not be greater than ρ_* or the red band in Figure 5.1. Given this constraint, we can see that the outer profile of Fornax is flat, while the inner portion rises more steeply than r^{-1}. Past dynamical studies of Fornax only compared generic cored and NFW profiles and did not test this up-bending profile, therefore it is difficult to compare to their results.

5.4.2 A Common Halo?

Despite the differences in the individual profiles of the dSphs, when we plot them on the same axes they appear to follow a combined r^{-1} profile with scatter. We plot this combined profile in Figure 5.2 with each galaxy's profile as a separate color. The uncertainties on the points are the $\Delta\chi^2 = 1$ uncertainties from Figure 5.1. We have scaled each galaxy's profile relative to an arbitrary r^{-1} profile. In this way the shape of each profile is preserved and only the height has been adjusted to reduce the scatter. We fit a line to the $\log \rho_{DM}$ profiles and determine that the slope $\alpha = 1.2 \pm 0.5$. We also restrict our fit to only points in the profile where we have kinematics (dotted line in Figure 5.2) and find a similar slope of $\alpha = 0.9 \pm 0.5$.

We conclude from Figure 5.2 that the *average* dark matter profile in the dSphs is similar to an r^{-1} profile. However, when we model each galaxy individually, we find a variety of profiles that are different from the mean r^{-1} profile. Our interpretation of this observation is that variations in their individual formation histories cause galaxies to scatter from the average profile. Only when multiple galax-

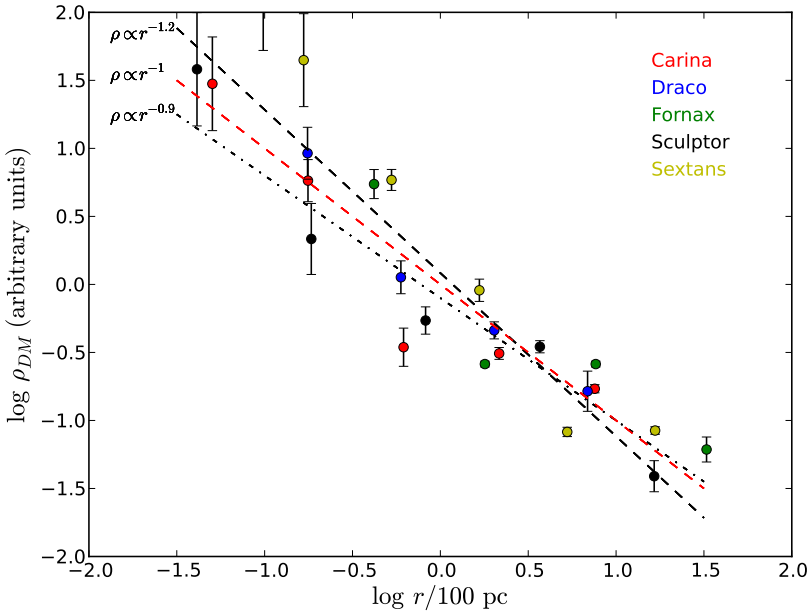

Figure 5.2 Combined dark matter density profiles of all the dSphs plotted on the same axes. Each galaxy's profile is plotted with the same colored points. Uncertainties on these points are the $\Delta\chi^2 = 1$ uncertainties from Figure 5.1. We plot the derived best-fit line with slope $\alpha = 1.2 \pm 0.5$ as a dashed line as well as the NFW profile with $\alpha = 1.0$ as a red dashed line. A fit excluding the points where we have no kinematics available is shown as a dotted line. The individual profiles have been scaled to a common height.

ies are averaged together does it become clear they follow a combined r^{-1} profile. This single power-law profile compares well with the predicted NFW profile in the inner portion of the plot. However, at larger radii ($\gtrsim 1$ kpc in dwarf galaxies) the NFW profile becomes steeper than r^{-1} (Springel et al., 2008). More data are needed at both large and small radii to further explore this.

K.G. acknowledges support from NSF-0908639. This work would not be possible without the state-of-the-art supercomputing facilities at the Texas Advanced Computing Center (TACC). We also thank Matt Walker and the MMFS Survey team for making their radial velocities publicly available.

Chapter 6

Non-parametric Schwarzschild Models of the Milky Way's Dwarf Spheroidal Satellites[1]

When I heard the learn'd astronomer;
When the proofs, the figures, were ranged in columns before me;
When I was shown the charts and the diagrams,
to add, divide, and measure them;
When I, sitting, heard the astronomer,
where he lectured with much applause in the lecture-room,
How soon, unaccountable, I became tired and sick;
Till rising and gliding out, I wander'd off by myself,
In the mystical moist night-air, and from time to time,
Look'd up in perfect silence at the stars.

Walt Whitman - "When I Heard the Learn'd Astronomer"

We present the results of orbit-based (or Schwarzschild) dynamical models for five of the Milky Way's bright dwarf spheroidal (dSph) satellites: Carina, Draco, Fornax, Sculptor, and Sextans. Previous work reported on their dark matter density profiles, here we present other results from the modeling and compare our findings to expectations from recent cosmological and hydrodynamical simulations. Our models find mild radial anisotropy in all five of the dSphs, consistent with predictions from the "tidal stirring" formation scenario. We also find that dSphs with larger stellar masses have more cored dark matter profiles, albeit with

[1]This chapter has been submitted to the Astrophysical Journal wth J.R. Jardel as first author. It appears here with permission from the American Astronomical Society.

large scatter. This trend is observed in recent hydrodynamical simulations that form late-type field dwarfs. Finally, we compare the circular speed profiles from our full dynamical models to those of simulated subhalos orbiting a Milky Way-like halo in the Aquarius simulation. We find that Draco is consistent with some of the halos previously thought to be "too big to fail". However, many simulated halos are still denser than the remaining dSphs.

6.1 Introduction

On the largest scales, the ΛCDM model for structure formation has enjoyed remarkable success in describing the universe we live in. Constraints from large-scale clustering of galaxies (Reid et al., 2010), the Lyman-α forest (Viel et al., 2008), and the cosmic microwave background (Komatsu et al., 2011) all suggest that dark matter is cold (i.e. massive and slow-moving) and contributes to the growth of structure in a bottom-up or hierarchical fashion. On these large scales, galaxy formation is accurately described by ΛCDM.

The current frontier in our knowledge of galaxy formation is at the low-mass level. Here we find disagreement between theory and observations in a variety of interesting cases. For example, observers measure dark matter profiles in dwarf galaxies (Burkert, 1995; Persic et al., 1996; de Blok et al., 2001; Simon et al., 2005) that differ from the theoretical predictions of ΛCDM simulations (Navarro et al. 1996b, hereafter NFW; Springel et al. 2008; Navarro et al. 2010). Studies have also found the population of observed dwarf galaxies orbiting the Milky Way to be both too small in number (Klypin et al., 1999; Moore et al., 1999) and dynamically different from simulations (Boylan-Kolchin et al., 2012).

The Milky Way's dwarf spheroidal (dSph) satellite galaxies are excellent objects to study in order to push our theoretical understanding to its low-mass limit. These nearby galaxies are the smallest that we can ever hope to study in detail with dynamical models. As such, they contain the most information that can be used to test ΛCDM in its low-mass limit.

Extracting this information with dynamics is not without its challenges, however. The dSphs, unlike other low-mass galaxies, are supported against gravity by the random motions of their stars instead of ordered rotation. Dynamical models can be constructed using the projected velocity dispersion profile $\sigma(R)$ and the Jeans equations of stellar dynamics. However, $\sigma(R)$ is, in general, anisotropic and the amount of anisotropy strongly influences the mass inferred from Jeans-based dynamical models. Furthermore, since we often only observe the component of a star's velocity that lies along our line of sight, the anisotropy is usually unconstrained in Jeans models. This leads authors to either make the simplifying assumption of isotropy (Gilmore et al., 2007; Walker et al., 2007) or to marginalize over their ignorance of the anisotropy (Walker et al., 2009a; Wolf et al., 2010). In the first case, models suffer from a bias introduced by an overly restrictive assumption (see Evans et al. 2009), and in the second case the degeneracy between mass and anisotropy precludes the level of precision required for detailed comparison to many theoretical predictions (Walker et al., 2009a; Wolf et al., 2010).

These issues have led several authors to abandon Jeans models in favor of the more general Schwarzschild (or orbit-based) dynamical models (Jardel & Gebhardt, 2012; Breddels et al., 2013). Instead of only fitting to $\sigma(R)$, these models fit to the entire line-of-sight velocity distribution (LOSVD). This allows the velocity anisotropy of a galaxy to be computed since stars on radial or tangential orbits leave signatures of this behavior in the shape of the LOSVD. Once the anisotropy is computed, Schwarzschild models have a more powerful lever with which to constrain the mass distribution.

Recently, Jardel et al. (2013) introduced a method to use Schwarzschild modeling to calculate the mass profiles of dSphs, and also larger galaxies, non-parametrically. This technique does not require the modeler to assume a functional form for the dark matter profile (which is often exactly what they mean to measure). In this paper we extend the analysis performed by Jardel & Gebhardt (2013) on the Carina, Fornax, Sculptor, and Sextans dSphs. In addition to obtaining information about the masses and dark matter content of the dSphs, we also report the types of orbits their stars populate. This orbit structure, calculated by Schwarzschild models while fitting to the LOSVDs, can offer additional hints about a galaxy's formation history (Lynden-Bell, 1967; van Albada, 1982; Hoffman et al., 2010) and the orbit structure of the dSphs is relatively unexplored territory (although see Jardel & Gebhardt 2012; Jardel et al. 2013; Breddels et al. 2013).

We also demonstrate the accuracy of the non-parametric technique through tests of a mock galaxy constructed with a known density distribution. We show that our modeling procedure accurately recovers this distribution from the derived kinematics.

6.2 Data

Our models require both photometry and kinematics to constrain the orbits of stars and the potentials in which they orbit. The data we use are described in Jardel & Gebhardt (2013) and the methods are outlined with more detail in Jardel et al. (2013). For clarity, we briefly discuss the data here. The interested reader is referred to the above papers for more detail.

6.2.1 Photometry

Our photometric analysis begins with the (projected) number density profile of stars $\Sigma_*(R)$. We list the sources of $\Sigma_*(R)$ in Jardel & Gebhardt (2013). To convert $\Sigma_*(R)$ into the more useful surface brightness profile $\mu(R)$, we apply an arbitrary zeropoint shift to $\Sigma_*(R)$ in log space and adjust this value until the integrated luminosity of the new $\mu(R)$ is equal to the value listed for each dSph in Mateo (1998). Next, we deproject each profile via Abel inversion to obtain the three-dimensional luminosity density profile (Gebhardt et al., 1996). For simplicity, and so that the deprojection is unique, we assume each galaxy is viewed edge-on. Our models assume axisymmetric geometry, and to obtain the density profile at position angles other than the major axis, we use the ellipticity adopted in Jardel & Gebhardt (2013). We plot the luminosity density profiles $\nu(R)$ for each galaxy in Figure 6.1.

6.2.2 Kinematics

The kinematics we use are individual radial velocities published in Walker et al. (2009b) with repeat measurements averaged. Using the membership probability P that Walker et al. (2009b) assign to each star, we discard velocities with $P < 0.95$. We correct for perspective rotation in the galaxies where high-quality *Hubble Space Telescope* measurements of proper motion are available (Carina and Fornax; Piatek et al. 2003, 2007). We then place the stars on a meridional grid folded about the major and minor axes. To preserve any possible rotation, we switch the sign of a star's velocity if it is flipped over the minor axis.

We group the resulting velocities into radial bins and construct the full

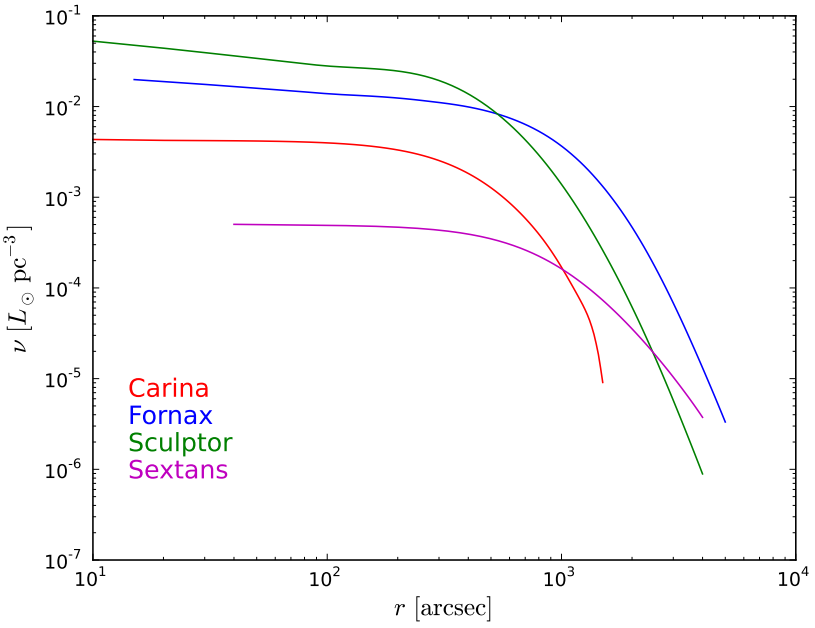

Figure 6.1 Deprojected luminosity density profiles $\nu(R)$ for the four dSphs.

LOSVD through the kernel density estimation procedure detailed in Jardel et al. (2013). The number of stars per bin ranges between 50 and 70. In Fornax and Sculptor, there are a substantial amount of radial velocities available. We therefore group stars into bins at a number of different position angles in addition to the standard radial binning.

Although the LOSVDs themselves are the primary input to the Schwarzschild models, we fit Gauss-Hermite moments to the non-parametric LOSVDs for illustrative purposes. We plot these moments in Figure 6.2.

6.3 Models

We use the non-parametric Schwarzschild modeling procedure introduced in Jardel et al. (2013). Based on the principle of orbit superposition (Schwarzschild, 1979), these models aim to construct a representative sample of the allowed stellar orbits in a galaxy. In doing so, they are constrained to match this population of orbits to the LOSVDs as well as the three-dimensional stellar light profile.

The orbit-based modeling technique begins by assuming a trial potential for the galaxy one wishes to model. This is done by assuming a density distribution $\rho(r,\theta)$, assuming axisymmetry, and solving Poisson's equation for associated potential. The flattening of the dark matter halo is presently tied to the value of the stellar ellipticity in each dSph, although it may in principle be different. Given the test potential, the task is now to populate an orbit library containing a representative sample of the allowed orbits in this potential. This is possible because all orbits in an axisymmetric potential respect three isolating integrals of motion: their

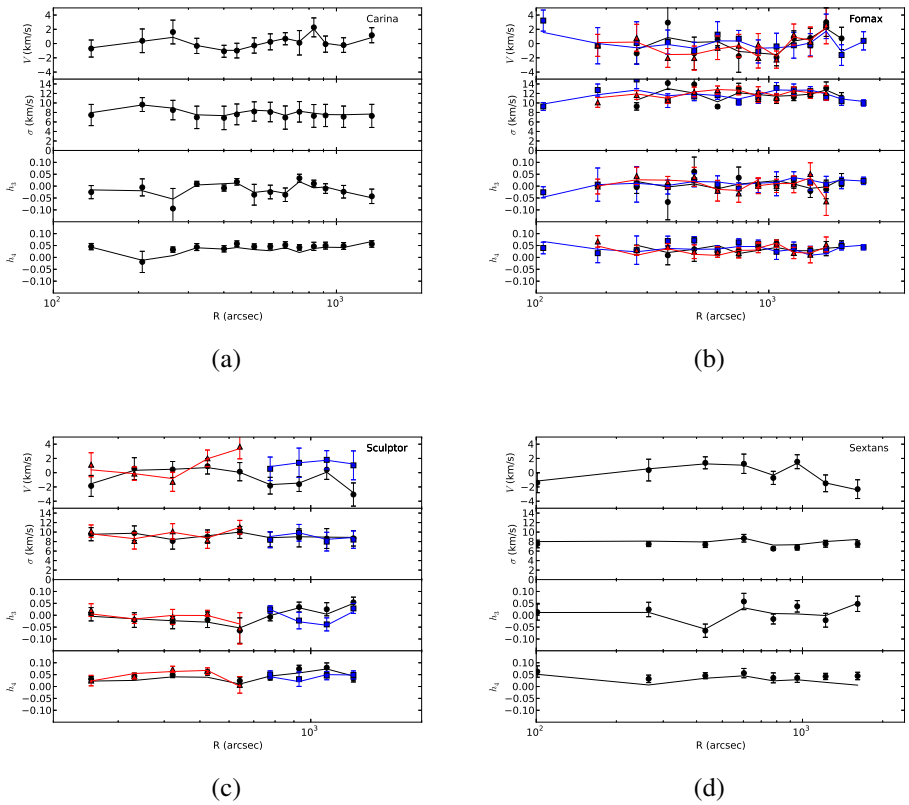

Figure 6.2 Gauss-Hermite moments fit to a) Carina, b) Fornax, c) Sculptor, and d) Sextans. Galaxies that have kinematics at multiple position angles show bins near the major axis in blue and those near the minor axis in red. The solid lines are the best fitting model for each galaxy.

total energy E, the z-component of their angular momentum L_z, and a third integral I_3 for which there exists to scheme to analytically calculate it a priori (Binney & Tremaine, 2008). Populating the orbit library is done by sampling these three integrals of motion over their range of possible values according to the scheme outlined in Thomas et al. (2004). A typical orbit library contains roughly 30,000 orbits.

Once the orbit library is constructed, each orbit is launched in the trial potential and followed for many crossing times. The orbit's position and velocity as a function of time are calculated numerically (Siopis et al., 2009) and stored for later comparison. Once the orbit integration has finished, the models assign a weight to each orbit and optimize the weights such that they best reproduce the observed LOSVDs and stellar luminosity profile. We use a χ^2 minimization technique, subject to a maximum entropy constraint (Siopis et al., 2009), to determine how well the orbit library is able to match the kinematics of the galaxy. If χ^2 is low, then the trial potential is a good fit. For large values of χ^2, the trial potential cannot host the types of orbits that would match the observed LOSVDs and a new trial potential is chosen. A typical model for a galaxy will be the best-fitting result of $\sim 15,000$ trial potentials.

6.3.1 Non-parametric models

The above discussion on Schwarzschild modeling is generic to every orbit-based code (Rix et al., 1997; van der Marel et al., 1998; Cretton et al., 1999; Gebhardt et al., 2000a; Valluri et al., 2004; van den Bosch et al., 2008). Going beyond standard Schwarzschild modeling, we have developed a technique to determine the

mass profile of the galaxy without having to assume anything about the distribution of dark matter. This is implemented in the way we select the trial potentials. Rather than adopting a parameterization for the halo density profile and sampling those parameters to choose trial potentials, we instead divide the total density profile $\rho(r)$ into $N_{\rm bin}$ radial points where we evaluate the density ρ_i at these points. In this way, the ρ_i themselves are the parameters whose values we sample in order to select new trial potentials.

We use $N_{\rm bin}$= 5 locations in the profiles, positioned at equal logarithmic intervals, and connect the ρ_i with straight line segments. The only restriction we place on the form of $\rho(r)$ is that it must be non-increasing with radius. To sample the ρ_i we use the procedure outlined in Jardel et al. (2013) where we initially use a brute force search of roughly ~ 4000 models on a course grid. We then narrow our search using an iterative refinement scheme. Once a large number of models are run near the locations of the suspected minima without further improvements to χ^2, we terminate the parameter search.

In addition to the ρ_i, we describe $\rho(r)$ with one extra parameter α_∞—the power-law extrapolated slope, with $\rho \propto r^{-\alpha_\infty}$ outside of our model grid. Following previous work (Jardel et al., 2013) we run models with $\alpha_\infty \in \{2, 3, 4\}$ for each trial density profile (combination of the ρ_i). In our subsequent analysis we marginalize over α_∞, since it is unconstrained, and treat it as a nuisance parameter. We also truncate the density distribution at the Jacobi radius defined by the dSph mass, Milky Way mass, and Galactocentric distance of each dSph. These truncation radii are listed in Table 1 of Jardel & Gebhardt (2013) and are all much larger than the

radial extent of our model grid. This lends support to the claim that tidal effects in the dSphs are not presently important.

6.3.2 χ^2 Analysis

In fitting to the LOSVDs, our models calculate χ^2 as:

$$\chi^2 = \sum_{i=1}^{N_{\rm LOSVD}} \sum_{j=1}^{N_{\rm vel}=15} \left(\frac{\ell_{ij}^{\rm obs} - \ell_{ij}^{\rm mod}}{\sigma_{ij}} \right)^2 . \tag{6.1}$$

Each LOSVD is broken into $N_{\rm vel} = 15$ bins in velocity space. The value of the ith LOSVD at velocity bin j is given by $\ell_{ij}^{\rm obs}$ and $\ell_{ij}^{\rm mod}$ for the observed and model-predicted LOSVDs respectively. The 1σ uncertainty in $\ell_{ij}^{\rm obs}$ is σ_{ij}. The $\ell_{ij}^{\rm mod}$ are the result of finding the values of the weights for each orbit in the library and χ^2 specifies how good a fit is obtained for a given trial potential. We compare between models (trial potentials) by the difference in χ^2 between a given model and the model with minimum $\chi^2_{\rm min}$. For five degrees of freedom (the five ρ_i) all models within $\Delta\chi^2 = 5.84$ above $\chi^2_{\rm min}$ are considered to be within 1σ.

We use the unreduced χ^2 to discriminate between models since it is often difficult to calculate the number of degrees of freedom in the LOSVDs. In calculating the observed LOSVDs, our kernel density estimator often introduces correlations among neighboring velocity bins. One can estimate the overall goodness-of-fit, and therefore convergence in our parameter sampling technique, by examining the model fits to the Gauss-Hermite moments of the kinematics in Figure 6.2. However, we stress that our models calculate χ^2 with respect to the LOSVDs as in

Equation (1).

6.3.3 Tests of the Models

The Schwarzschild modeling code that is the backbone of our non-parametric procedure has been thoroughly tested with artificial data. These tests show that the procedure is capable of accurately recovering the mass profile and orbit structure of simple cases like an isotropic rotator (Thomas et al., 2005) as well as more complex N-body merger remnants (Thomas et al., 2007a). The models are also able to detect and accurately measure a supermassive black hole at the center of a mock galaxy (Siopis et al., 2009). Here we demonstrate the accuracy of our non-parametric models through similar tests.

We wish to test whether our non-parametric models can accurately recover the density profiles of two known test cases. We choose the density profile of the logarithmic potential, with its inner core that transitions to an outer r^{-2} profile, as well as a single power-law profile with a slope of r^{-1} meant to mimic the inner portion of the NFW profile. These profiles are examples of the types of dark matter profiles found in dwarf galaxies. For the stellar component, we choose to embed the three-dimensional stellar light profile of Draco (Jardel et al., 2013) into these halos. The resulting mass profile is dominated at all radii by the dark matter, as is the case in the dSphs. For simplicity, we assume spherical symmetry.

Once the potential and stellar light distribution have been established, we use the Jeans Anisotropic Multi-Gaussian Expansion (JAM) models of Cappellari (2008) to determine the kinematics that these choices would produce. Under the

simplifying requirements that the test models have no rotation and isotropic velocity ellipsoids, we obtain the projected velocity dispersion profiles $\sigma(R)$ for each test case. These profiles cover a range in radius similar to the dSphs we model in this paper. At each of the 17 locations where $\sigma(R)$ has been evaluated, we construct an LOSVD from the velocity dispersion under the assumption that the higher Gauss-Hermite moments h_3 and h_4, as well as the rotational velocity V, are zero. In our construction of the LOSVDs, we add noise to the velocity dispersion at the 20% level—a level consistent with the observational uncertainties of the dSphs we model.

The LOSVDs for both test cases are then used as input to the non-parametric Schwarzschild models just as they would be for a typical dSph. We use the same parameter sampling technique described in Jardel et al. (2013) to search for the χ^2 minimum. We present the best-fitting density profiles that are recovered in Figure 6.3. We are able to accurately and precisely recover the density profiles in both test cases, indicating these models are well suited for this type of work.

6.4 Results

We present the detailed results of our modeling of Carina, Fornax, Sculptor, and Sextans in this section. Earlier papers reported the derived dark matter density profiles (Jardel et al., 2013; Jardel & Gebhardt, 2013). In this paper we focus on other aspects of the modeling such as the derived circular speed profiles $V_c(r)$ and the orbital anisotropy.

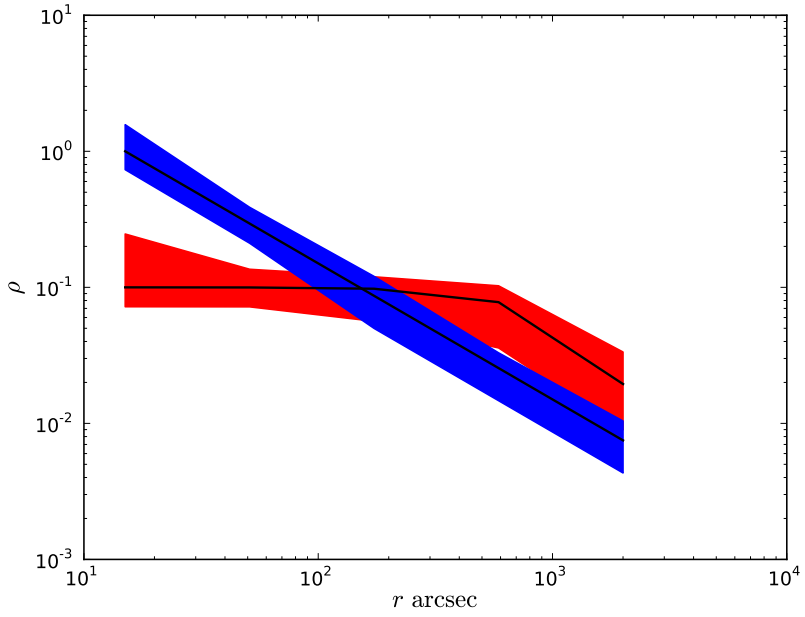

Figure 6.3 Results of our two test cases recovering density profiles with cored (red) and cuspy (blue) profiles. For each profile, the black line is the initial profile from which we derive the kinematics. The 1σ point-wise confidence interval is the shaded colored region.

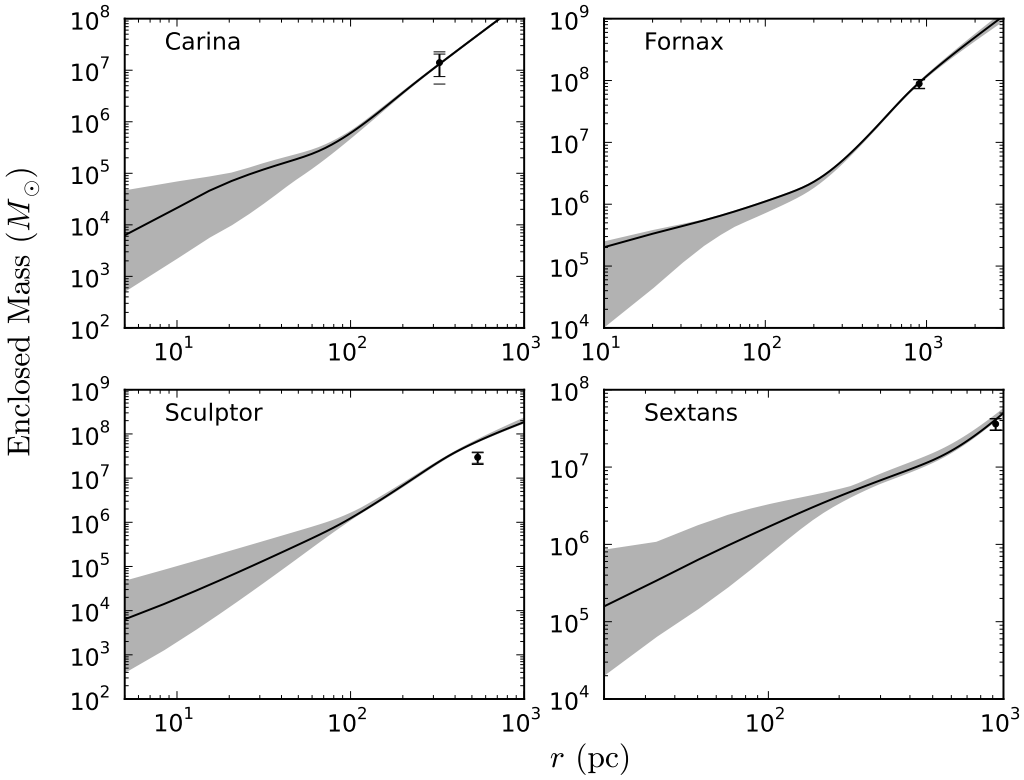

Figure 6.4 Total enclosed mass as a function of radius for Carina, Fornax, Sculptor, and Sextans. The 1σ uncertainties derived from $\Delta\chi^2 = 5.84$ are shown as the gray shaded region. The best fitting model is plotted as a solid line. We also plot the mass derived from the Wolf et al. (2010) mass estimator with its uncertainty as the black point with error bars.

6.4.1 Masses

We plot the total enclosed mass as a function of radius in Figure 6.4. The shaded region indicates the 1σ uncertainties derived from $\Delta\chi^2 = 5.84$ as described above. In each panel, the uncertainties are largest near the center of the galaxy where kinematics are sparse. This is also seen in the dark matter density profiles derived in Jardel & Gebhardt (2013) and motivates the need for more radial velocities in their centers.

We also compare our enclosed mass measurements with the convenient mass estimator suggested by Wolf et al. (2010) (see also Walker et al. 2009a; Cappellari et al. 2006). In Wolf et al. (2010), the authors present an analytical argument that near the three-dimensional half-light radius r_e, the enclosed mass in a galaxy is relatively insensitive to velocity anisotropy. This provides a convenient way to robustly measure the mass at one location in a galaxy without running expensive dynamical models. Much recent work is based on dynamical masses obtained in this manner (Walker & Peñarrubia, 2011; Boylan-Kolchin et al., 2012), and although Wolf et al. (2010) provide an analytical justification for why the anisotropy is minimized near r_e, this justification assumes spherical symmetry as well as a simplified anisotropy profile.

Here we test the accuracy of this mass estimator against the full mass profiles from our non-parametric dynamical models. According to Wolf et al. (2010), the mass enclosed at the three-dimensional half-light radius takes the form:

$$M_{1/2} \approx 4G^{-1}R_e < \sigma^2_{\rm LOS} >, \tag{6.2}$$

where R_e is the projected half-light radius, and $< \sigma_{\rm LOS} >$ is the luminosity-averaged velocity dispersion along the line of sight. We calculate these quantities directly from the kinematic and photometric data that we input to the model. We plot the derived values for the $M_{1/2}$ estimator as points with error bars in Figure 6.4. In all of the galaxies except Sculptor, our model-derived mass at the half-light radius lies within the error bars on $M_{1/2}$. We see this as evidence that $M_{1/2}$ is an accurate estimator of the enclosed mass at r_e, even in axisymmetric galaxies with non-ideal anisotropy profiles.

6.4.2 Orbital Anisotropy

Aside from constraining the mass distribution in these galaxies, our models also calculate the velocity anisotropy from the best-fitting orbit structure. This extra bit of information can potentially encode additional clues about the formation of the dSphs.

It is widely believed that the dSphs were once disky galaxies (Kormendy et al. 2009; Kormendy & Bender 2012 and references therein) that were transformed into their spheroidal shape through environmental processes. One such process, known as "tidal stirring", causes the circular orbits of the proto-dSphs to be heated and randomized by repeated passage through the Milky Way's dark matter halo. This causes an increase in V/σ and results in the transformation of a disk galaxy into a spheroidal. Simulations of this scenario tend to produce dSphs with an excess

of stars on radial orbits (Łokas et al., 2010; Kazantzidis et al., 2011), perhaps owing to the presence of a tidally-induced bar (Łokas et al., 2010).

Here we are able to directly test this prediction by calculating the anisotropy observed in the dSphs. We parameterize this with the ratio of the radial to tangential components of the velocity dispersion tensor in spherical polar coordinates:

$$\frac{\sigma_r}{\sigma_t} = \frac{\sigma_r}{\sqrt{\frac{1}{2}(\sigma_\theta^2 + \sigma_\phi^2 + v_\phi^2)}} \quad . \tag{6.3}$$

Streaming motions in the r and θ directions are assumed to be zero. We compute σ_r/σ_t as a function of radius where our kinematics data lie. Whenever $\sigma_r/\sigma_t > 1$, this indicates regions of the galaxy with radial anisotropy.

We plot the run of σ_r/σ_t with radius in each of the four galaxies in Figure 6.5. Each dSph shows a mild tendency towards radial anisotropy at all radii, and most also show a positive gradient of increasing σ_r/σ_t with radius. The radial anisotropy we observe lends support to the tidal stirring scenario for the dSphs. However, we caution that there are likely many plausible mechanisms that could introduce radial anisotropy to orbit structure of the dSphs.

Ours are not the only measurements of anisotropy in dSphs, however. Using spherical Schwarzschild models that fit to the moments of the LOSVDs, Breddels et al. (2013) find mildly tangential anisotropy in all of the dSphs. This difference could be due to differences in assumptions about geometry, or perhaps a difference in the two groups' modeled best-fitting density profiles. Note, however, that qualitatively the measurements of the total mass enclosed within $r = 1$ kpc agree.

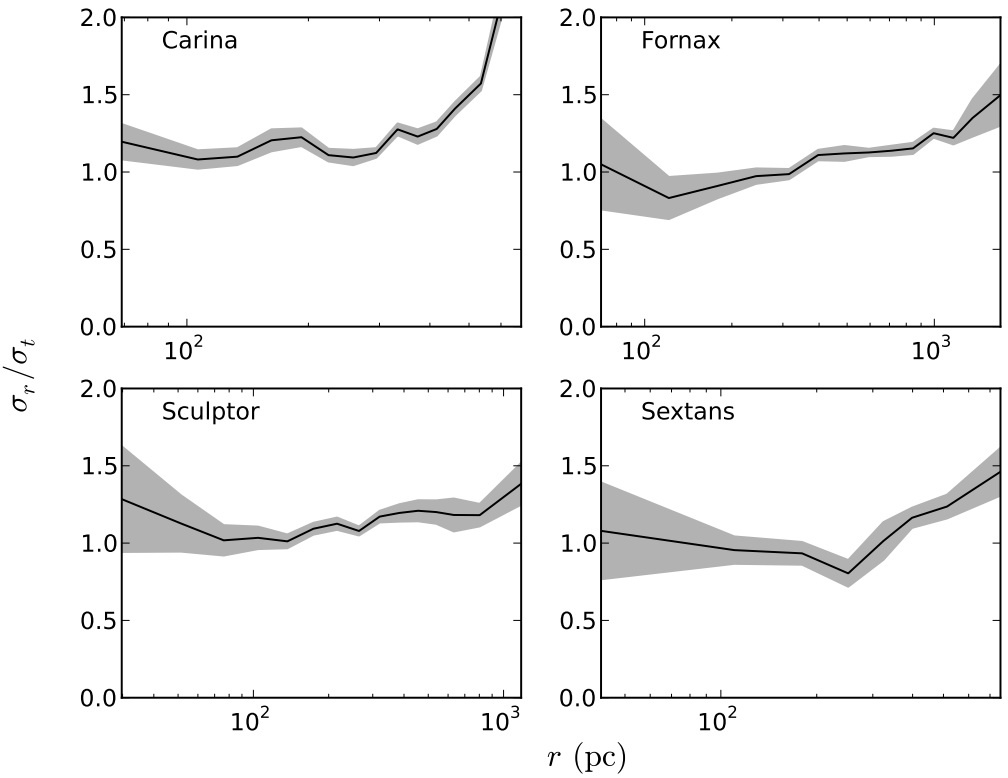

Figure 6.5 Orbital anisotropy in the four dSphs. We plot the ratio of the radial to tangential components of the velocity dispersion, defined in Equation (3). Most of the dSphs exhibit mild radial anisotropy.

6.5 Comparison to Simulations

In this section we further explore the dark matter halos of the dSphs. In Jardel & Gebhardt (2013), we plot the dark matter profiles of five bright dSphs determined with our new non-parametric Schwarzschild technique. We found a variety of differing profile shapes in the dSphs. However, when scaled to a common height we found the *combined* profile of all five dSphs appeared similar to the inner part of the NFW profile. Here, we follow up on those observations and compare our results to cosmological simulations.

6.5.1 Why is there variation in the dSph profiles?

One interesting explanation for the variety of dark matter profiles ties the halo's profile slope to the number of stars that managed to form in the galaxy. Using cosmological *N*-body simulations complete with a hydrodynamical treatment of baryons, Governato et al. (2012) simulate the formation of a number of isolated dwarf galaxies. They find a trend of decreasing dark matter profile slope (becoming more cored) when their simulated dwarf galaxies have larger stellar mass. Recently, Pontzen & Governato (2014) have expanded on these simulations and provided a detailed framework explaining this process (Pontzen & Governato, 2012). They attribute the trend to the fact that when more stars form, this leads to more supernovae, which can cause a greater reduction in central dark matter density (Navarro et al., 1996a). At the extreme low-mass end, however, the force of adiabatic compression (Blumenthal et al., 1986) overwhelms the meager energy from supernovae and cause an increase in dark matter density, leading to profiles steeper than the

NFW cusp.

In Figure 6.6 we plot the dSphs overlaid on the simulated dwarfs from Pontzen & Governato (2014). In general, the dSphs appear to follow the same trend as the simulations, although with larger scatter. However, it must be noted that there would be little correlation if the data point corresponding to Fornax was removed. Figure 6.6 also shows the result of Jardel & Gebhardt (2013), that the mean slope of the dSphs dark matter profiles is near $\alpha = -1$, since the average of all the blue crosses in Figure 6.6 is close to -1. The Pontzen & Governato (2014) work provides a mechanism to explain the variety of profile shapes observed (Jardel & Gebhardt, 2013).

6.5.2 Are the dSphs "Too Big to Fail"?

In addition to the classic Missing Satellites Problem, where ΛCDM simulations produce vastly more low-mass satellites than observed (Moore et al., 1999; Klypin et al., 1999), the Milky Way's satellites have recently been found to differ dynamically from those produced in large-scale ΛCDM simulations (Boylan-Kolchin et al., 2012). Comparing the satellites of a Milky Way-sized halo in the Aquarius Simulations (Springel et al., 2008) to observations of the Milky Way's own dSphs reveals that many more simulated halos have higher circular speeds than any dSph. Boylan-Kolchin et al. (2012) make this determination without running dynamical models, but by using the Wolf et al. (2010) mass estimator to calculate the circular speed V_c at the half light radius for each dSph. Here we extend this work to include the full circular speed profiles of the dSphs measured from dynam-

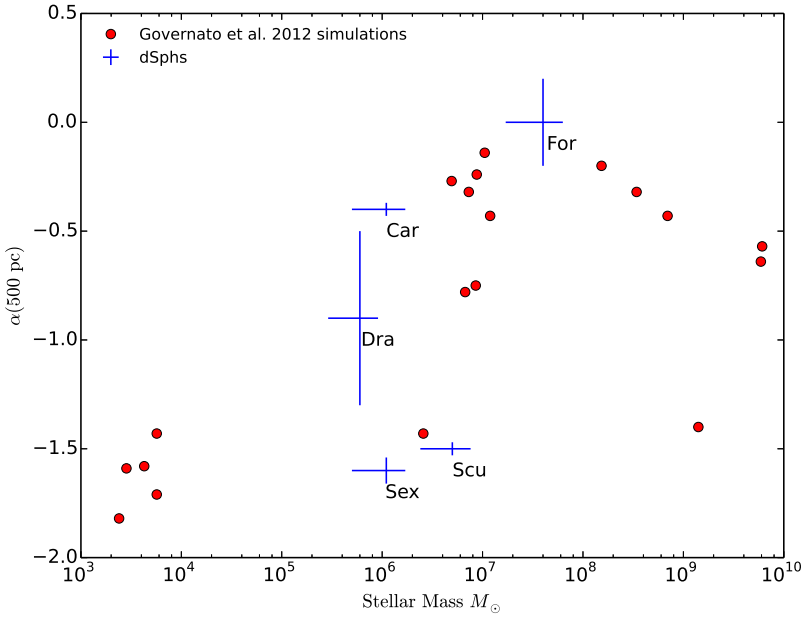

Figure 6.6 Slope of the dark matter density profile as a function of stellar mass for the dSphs and the simulated dwarf galaxies from Pontzen & Governato (2014). The slopes are evaluated at 500 pc for each galaxy/simulation.

ical models.

Nevertheless, it is instructive to make the same comparisons as Boylan-Kolchin et al. (2012) to dark matter-only simulations, but now with the full circular speed profiles determined by sophisticated dynamical models. In Figure 6.7 we plot the 1σ confidence intervals on the circular speed profiles $V_c(r)$ for Carina, Draco, Fornax, Sculptor, and Sextans. Overlaid in gray are the circular speed profiles from satellites around the Aquarius Simulation's E halo (virial mass $M_{\rm vir} = 1.4 \times 10^{12} M_\odot$). Magellanic Cloud-sized halos have been removed by the technique described in Boylan-Kolchin et al. (2012). We also plot our derived values for $V_c(r = r_{1/2})$ from the Wolf et al. (2010) estimator as similar colored points with error bars.

Boylan-Kolchin et al. (2012) interpret the low $V_c(r = r_{1/2})$ of the dSphs when compared to $V_c(r)$ of the simulations to mean that ΛCDM over-predicts the number of massive dwarf galaxies. This is because it is difficult to imagine these massive halos exist in the Local Group but never formed enough stars for us to observe them as dSphs. One alternative to this interpretation is that feedback from supernovae alters the dark matter content of real dwarf galaxies, and should therefore reduce V_c in the gray curves in Figure 6.7. Zolotov et al. (2012) show this effect can be large enough to reconcile the problem. Ram-pressure stripping can also remove baryons and alter the halo density. Arraki et al. (2014) show that this effect, when simulated in a realistic tidal field, leads to massive tidal stripping which can significantly lower V_c enough to match observations. These types of feedback can also expel all the gas from the lowest-mass halos and keep them from ever forming stars, thereby solving

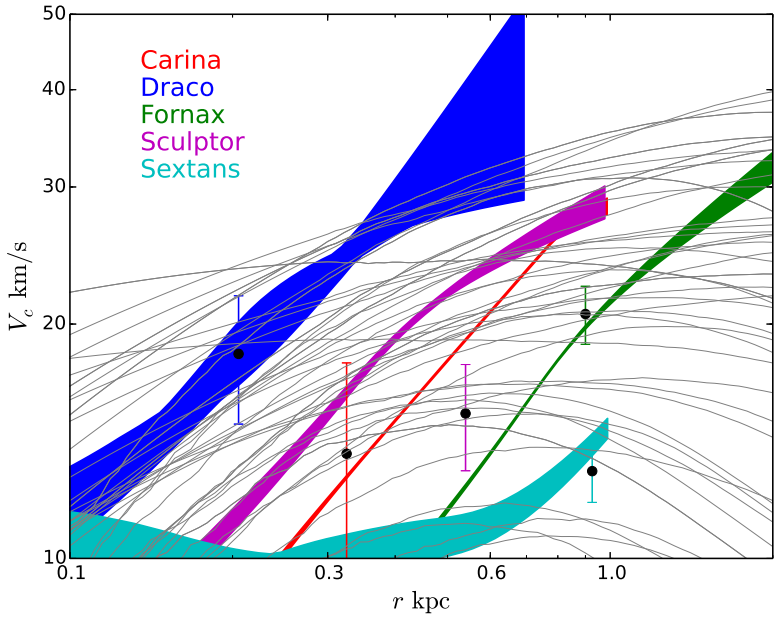

Figure 6.7 Circular speed profiles of Carina, Draco, Fornax, Sculptor, and Sextans plotted with their 1σ uncertainties as filled curves. Also plotted is $V_c(r = r_{1/2})$ measured from $M_{1/2}$ as points with colored error bars. We plot the V_c profiles of subhalos orbiting the E halo in the Aquarius simulation as gray curves. Only shown are subhalos with maximum circular speed $V_{\rm max} > 10$ km s^{-1} and maximum circular speed at infall $V_{\rm max} > 30$ km s^{-1}. The E halo has a virial mass of $M_{\rm vir} = 1.4 \times 10^{12}\,M_\odot$.

the classical missing satellites problem (Brooks et al., 2013).

Another way to relieve the tension between the simulated halos and the Boylan-Kolchin et al. (2012) measurements of the dSphs' $V_c(r = r_{1/2})$ is to change the mass of the Milky Way. Recent work suggests that the number of massive satellites around a Milky Way-sized halo is a stochastic quantity with a large dispersion, and the Milky Way's dSph population may not be as large an outlier as previously thought (Purcell & Zentner, 2012; Wang et al., 2012; Vera-Ciro et al., 2013). However, similar results found in the M31 system (Tollerud et al., 2014) make this option less attractive.

Figure 6.7 shows that at least some of the halos deemed "massive failures" by Boylan-Kolchin et al. (2012) are consistent with being Draco analogs in the Milky Way's satellite system. However, there are still many more simulated halos with greater circular speeds than the remaining four dSphs. It remains an open question whether tension can be relieved through baryonic feedback or by assuming a smaller mass for the Milky Way. If we instead use Draco as an example of agreement between ΛCDM and observations, then this sets an upper limit to the amount of feedback that could have occurred. Otherwise Draco's V_c curve would be far below the simulated curves in Figure 6.7.

This work would not be possible without the supercomputing power provided by the Texas Advanced Computing Center (TACC). We thank Fabio Governato and Andrew Pontzen for providing data from their hydrodynamical simula-

tions. We are also grateful to Mike Boylan-Kolchin and the Aquarius collaboration for providing access to their data.

Bibliography

Adams, J. J., Gebhardt, K., Blanc, G. A., et al. 2012, ApJ, 745, 92

Amorisco, N. C., & Evans, N. W. 2011a, MNRAS, 1606

—. 2011b, MNRAS, 411, 2118

Armandroff, T. E., Olszewski, E. W., & Pryor, C. 1995, AJ, 110, 2131

Arraki, K. S., Klypin, A., More, S., & Trujillo-Gomez, S. 2012, ArXiv e-prints

—. 2014, MNRAS, 438, 1466

Bacon, R., Copin, Y., Monnet, G., et al. 2001, MNRAS, 326, 23

Beers, T. C., Flynn, K., & Gebhardt, K. 1990, AJ, 100, 32

Begelman, M. C., Volonteri, M., & Rees, M. J. 2006, MNRAS, 370, 289

Bell, E. F., & de Jong, R. S. 2001, ApJ, 550, 212

Bendo, G. J., Buckalew, B. A., Dale, D. A., et al. 2006, ApJ, 645, 134

Bersier, D. 2000, ApJL, 543, L23

Bertin, E., & Arnouts, S. 1996, A&AS, 117, 393

Binney, J. 1978, MNRAS, 183, 501

Binney, J., Gerhard, O., & Silk, J. 2001, MNRAS, 321, 471

Binney, J., & Tremaine, S. 1987, Galactic dynamics, ed. Binney, J. & Tremaine, S.

—. 2008, Galactic Dynamics: Second Edition (Princeton University Press)

Blais-Ouellette, S., Amram, P., & Carignan, C. 2001, AJ, 121, 1952

Blumenthal, G. R., Faber, S. M., Flores, R., & Primack, J. R. 1986, ApJ, 301, 27

Borriello, A., & Salucci, P. 2001, MNRAS, 323, 285

Bovill, M. S., & Ricotti, M. 2009, ApJ, 693, 1859

Boylan-Kolchin, M., Bullock, J. S., & Kaplinghat, M. 2012, MNRAS, 2657

Breddels, M. A., Helmi, A., van den Bosch, R. C. E., van de Ven, G., & Battaglia, G. 2013, MNRAS, 433, 3173

Bridges, T. J., Rhode, K. L., Zepf, S. E., & Freeman, K. C. 2007, ApJ, 658, 980

Brooks, A. M., Kuhlen, M., Zolotov, A., & Hooper, D. 2013, ApJ, 765, 22

Bullock, J. S., Kolatt, T. S., Sigad, Y., et al. 2001, MNRAS, 321, 559

Bullock, J. S., Kravtsov, A. V., & Weinberg, D. H. 2000, ApJ, 539, 517

Burkert, A. 1995, ApJL, 447, L25+

Burkert, A., & Tremaine, S. 2010, ApJ, 720, 516

Burkhead, M. S. 1986, AJ, 91, 777

Cappellari, M. 2008, MNRAS, 390, 71

Cappellari, M., Bacon, R., Bureau, M., et al. 2006, MNRAS, 366, 1126

Coleman, M. G., Da Costa, G. S., Bland-Hawthorn, J., & Freeman, K. C. 2005, AJ, 129, 1443

Côté, P., McLaughlin, D. E., Cohen, J. G., & Blakeslee, J. P. 2003, ApJ, 591, 850

Côté, P., McLaughlin, D. E., Hanes, D. A., et al. 2001, ApJ, 559, 828

Cretton, N., de Zeeuw, P. T., van der Marel, R. P., & Rix, H. 1999, ApJS, 124, 383

de Blok, W. J. G. 2010, Advances in Astronomy, 2010

de Blok, W. J. G., McGaugh, S. S., Bosma, A., & Rubin, V. C. 2001, ApJL, 552, L23

de Boer, T. J. L., Tolstoy, E., Hill, V., et al. 2012a, A&A, 544, A73

—. 2012b, A&A, 539, A103

Dekel, A., & Silk, J. 1986, ApJ, 303, 39

Dressler, A. 1989, in IAU Symposium, Vol. 134, Active Galactic Nuclei, ed. D. E. Osterbrock & J. S. Miller, 217

Eisenstein, D. J., & Loeb, A. 1995, ApJ, 443, 11

El-Zant, A., Shlosman, I., & Hoffman, Y. 2001, ApJ, 560, 636

Elias, J. H., Joyce, R. R., Liang, M., et al. 2006, in proc SPIE, Vol. 6269,

Emsellem, E., Monnet, G., & Bacon, R. 1994a, A&A, 285, 723

Emsellem, E., Monnet, G., Bacon, R., & Nieto, J.-L. 1994b, A&A, 285, 739

Emsellem, E., Cappellari, M., Peletier, R. F., et al. 2004, MNRAS, 352, 721

Evans, N. W., An, J., & Walker, M. G. 2009, MNRAS, 393, L50

Fabricius, M. H., Barnes, S., Bender, R., et al. 2008, in Society of Photo-Optical Instrumentation Engineers (SPIE) Conference Series, Vol. 7014, Society of Photo-Optical Instrumentation Engineers (SPIE) Conference Series

Ferrarese, L., & Ford, H. 2005, Space Science Reviews, 116, 523

Ferrarese, L., & Merritt, D. 2000, ApJL, 539, L9

Gadotti, D. A., & Sánchez-Janssen, R. 2012, MNRAS, 423, 877

Gao, L., Navarro, J. F., Cole, S., et al. 2008, MNRAS, 387, 536

Gebhardt, K., & Thomas, J. 2009, ApJ, 700, 1690

Gebhardt, K., Richstone, D., Ajhar, E. A., et al. 1996, AJ, 112, 105

Gebhardt, K., Bender, R., Bower, G., et al. 2000a, ApJL, 539, L13

Gebhardt, K., Richstone, D., Kormendy, J., et al. 2000b, AJ, 119, 1157

Gebhardt, K., Richstone, D., Tremaine, S., et al. 2003, ApJ, 583, 92

Gilmore, G., Wilkinson, M. I., Wyse, R. F. G., et al. 2007, ApJ, 663, 948

Goerdt, T., Moore, B., Read, J. I., Stadel, J., & Zemp, M. 2006, MNRAS, 368, 1073

Gössl, C. A., & Riffeser, A. 2002, A&A, 381, 1095

Governato, F., Zolotov, A., Pontzen, A., et al. 2012, MNRAS, 422, 1231

Grillo, C. 2010, ApJ, 722, 779

Gültekin, K., Richstone, D. O., Gebhardt, K., et al. 2009a, ApJ, 695, 1577

—. 2009b, ApJ, 698, 198

Hargreaves, J. C., Gilmore, G., & Annan, J. D. 1996, MNRAS, 279, 108

Häring, N., & Rix, H. 2004, ApJL, 604, L89

Harris, G. L. H., & Harris, W. E. 2011, MNRAS, 410, 2347

Hernquist, L. 1990, ApJ, 356, 359

Hill, G. J., MacQueen, P. J., Tufts, J. R., et al. 2006, Proc. SPIE, 6269

Hoffman, L., Cox, T. J., Dutta, S., & Hernquist, L. 2010, ApJ, 723, 818

Houghton, R. C. W., Magorrian, J., Sarzi, M., et al. 2006, MNRAS, 367, 2

Irwin, M., & Hatzidimitriou, D. 1995, MNRAS, 277, 1354

Jardel, J. R., & Gebhardt, K. 2012, ApJ, 746, 89

Jardel, J. R., & Gebhardt, K. 2013, ApJL, 775, L30

Jardel, J. R., Gebhardt, K., Fabricius, M. H., Drory, N., & Williams, M. J. 2013, ApJ, 763, 91

Jardel, J. R., & Sellwood, J. A. 2009, ApJ, 691, 1300

Jeans, J. H. 1919, Royal Society of London Philosophical Transactions Series A, 218, 157

Kazantzidis, S., Łokas, E. L., Callegari, S., Mayer, L., & Moustakas, L. A. 2011, ApJ, 726, 98

Kleyna, J., Wilkinson, M. I., Evans, N. W., Gilmore, G., & Frayn, C. 2002, MNRAS, 330, 792

Klypin, A., Kravtsov, A. V., Valenzuela, O., & Prada, F. 1999, ApJ, 522, 82

Koch, A., Kleyna, J. T., Wilkinson, M. I., et al. 2007, AJ, 134, 566

Komatsu, E., Smith, K. M., Dunkley, J., et al. 2011, ApJS, 192, 18

Kormendy, J. 1982, in Saas-Fee Advanced Course 12: Morphology and Dynamics of Galaxies, ed. L. Martinet & M. Mayor, 113–288

Kormendy, J. 1988, ApJ, 335, 40

Kormendy, J. 1993, in The Nearest Active Galaxies, ed. J. Beckman, L. Colina, & H. Netzer, 197–218

Kormendy, J. 2004, in Coevolution of Black Holes and Galaxies, ed. L. C. Ho, 1–+

Kormendy, J., & Bender, R. 2012, ApJS, 198, 2

Kormendy, J., Bender, R., & Cornell, M. E. 2011, Nature, 469, 374

Kormendy, J., Fisher, D. B., Cornell, M. E., & Bender, R. 2009, ApJS, 182, 216

Kormendy, J., & Freeman, K. C. 2004, in IAU Symposium, Vol. 220, Dark Matter in Galaxies, ed. S. Ryder, D. Pisano, M. Walker, & K. Freeman, 377

Kormendy, J., & Freeman, K. C. 2011, in preparation

Kormendy, J., & Gebhardt, K. 2001, in American Institute of Physics Conference Series, Vol. 586, 20th Texas Symposium on relativistic astrophysics, ed. J. C. Wheeler & H. Martel, 363–381

Kormendy, J., & Ho, L. C. 2013, ARA&A, 51, 511

Kormendy, J., & Illingworth, G. 1982, ApJ, 256, 460

Kormendy, J., & Kennicutt, Jr., R. C. 2004, ARA&A, 42, 603

Kormendy, J., & Richstone, D. 1995, ARA&A, 33, 581

Kormendy, J., & Westpfahl, D. J. 1989, ApJ, 338, 752

Kormendy, J., Bender, R., Ajhar, E. A., et al. 1996, ApJL, 473, L91+

Laor, A. 2001, ApJ, 553, 677

Lauer, T. R., Faber, S. M., Ajhar, E. A., Grillmair, C. J., & Scowen, P. A. 1998, AJ, 116, 2263

Lee, M. G., Yuk, I.-S., Park, H. S., Harris, J., & Zaritsky, D. 2009, ApJ, 703, 692

Lianou, S., Grebel, E. K., & Koch, A. 2011, A&A, 531, A152

Łokas, E. L., Kazantzidis, S., Klimentowski, J., Mayer, L., & Callegari, S. 2010, ApJ, 708, 1032

Łokas, E. L., Mamon, G. A., & Prada, F. 2005, MNRAS, 363, 918

Lucy, L. B. 1974, AJ, 79, 745

Lynden-Bell, D. 1967, MNRAS, 136, 101

Mackey, A. D., & Gilmore, G. F. 2003, MNRAS, 340, 175

Magorrian, J., Tremaine, S., Richstone, D., et al. 1998, AJ, 115, 2285

Maraston, C. 1998, MNRAS, 300, 872

—. 2005, MNRAS, 362, 799

Marconi, A., & Hunt, L. K. 2003, ApJL, 589, L21

Marigo, P., Girardi, L., Bressan, A., et al. 2008, A&A, 482, 883

Mateo, M. L. 1998, ARA&A, 36, 435

McLure, R. J., & Dunlop, J. S. 2002, MNRAS, 331, 795

Merritt, D., Navarro, J. F., Ludlow, A., & Jenkins, A. 2005, ApJL, 624, L85

Moore, B., Ghigna, S., Governato, F., et al. 1999, ApJL, 524, L19

Murphy, J. D., Gebhardt, K., & Adams, J. J. 2011, ApJ, 729, 129

Navarro, J. F., Eke, V. R., & Frenk, C. S. 1996a, MNRAS, 283, L72

Navarro, J. F., Frenk, C. S., & White, S. D. M. 1996b, ApJ, 462, 563

Navarro, J. F., Hayashi, E., Power, C., et al. 2004, MNRAS, 349, 1039

Navarro, J. F., Ludlow, A., Springel, V., et al. 2010, MNRAS, 402, 21

Odenkirchen, M., Grebel, E. K., Harbeck, D., et al. 2001, AJ, 122, 2538

Olszewski, E. W., Pryor, C., & Armandroff, T. E. 1996, AJ, 111, 750

Peñarrubia, J., McConnachie, A. W., & Navarro, J. F. 2008, ApJ, 672, 904

Persic, M., Salucci, P., & Stel, F. 1996, MNRAS, 281, 27

Piatek, S., Pryor, C., Bristow, P., et al. 2007, AJ, 133, 818

Piatek, S., Pryor, C., Olszewski, E. W., et al. 2003, AJ, 126, 2346

—. 2002, AJ, 124, 3198

Pietrzyński, G., Gieren, W., Szewczyk, O., et al. 2008, AJ, 135, 1993

Pinkney, J., Gebhardt, K., Bender, R., et al. 2003, ApJ, 596, 903

Pontzen, A., & Governato, F. 2012, MNRAS, 421, 3464

—. 2014, Nature, 506, 171

Purcell, C. W., & Zentner, A. R. 2012, JCAP, 12, 7

Reid, B. A., Percival, W. J., Eisenstein, D. J., et al. 2010, MNRAS, 404, 60

Rhode, K. L., & Zepf, S. E. 2004, AJ, 127, 302

Richardson, W. H. 1972, Journal of the Optical Society of America (1917-1983), 62, 55

Richstone, D. O., & Tremaine, S. 1988, ApJ, 327, 82

Rix, H., de Zeeuw, P. T., Cretton, N., van der Marel, R. P., & Carollo, C. M. 1997, ApJ, 488, 702

Salucci, P., & Burkert, A. 2000, ApJL, 537, L9

Sánchez-Blázquez, P., Gorgas, J., Cardiel, N., & González, J. J. 2006, A&A, 457, 809

Schlegel, D. J., Finkbeiner, D. P., & Davis, M. 1998, ApJ, 500, 525

Schulze, A., & Gebhardt, K. 2011, ApJ, 729, 21

Schwarzschild, M. 1979, ApJ, 232, 236

Ségall, M., Ibata, R. A., Irwin, M. J., Martin, N. F., & Chapman, S. 2007, MNRAS, 375, 831

Sersic, J. L. 1968, Atlas de Galaxias Australes (Cordoba, Argentina: Observatorio Astronomico, Univ. Cordoba)

Shen, J., & Gebhardt, K. 2010, ApJ, 711, 484

Silverman, B. W. 1986, Density estimation for statistics and data analysis, ed. Silverman, B. W.

Simon, J. D., Bolatto, A. D., Leroy, A., Blitz, L., & Gates, E. L. 2005, ApJ, 621, 757

Simon, J. D., & Geha, M. 2007, ApJ, 670, 313

Siopis, C., Gebhardt, K., Lauer, T. R., et al. 2009, ApJ, 693, 946

Springel, V., Wang, J., Vogelsberger, M., et al. 2008, MNRAS, 391, 1685

Stadel, J., Potter, D., Moore, B., et al. 2009, MNRAS, 398, L21

Strigari, L. E., Bullock, J. S., Kaplinghat, M., et al. 2008a, Nature, 454, 1096

—. 2008b, Nature, 454, 1096

Tammann, G. A., Sandage, A., & Reindl, B. 2008, ApJ, 679, 52

Tempel, E., & Tenjes, P. 2006, MNRAS, 371, 1269

Thomas, J., Jesseit, R., Naab, T., et al. 2007a, MNRAS, 381, 1672

Thomas, J., Saglia, R. P., Bender, R., et al. 2005, MNRAS, 360, 1355

—. 2007b, MNRAS, 382, 657

—. 2009, ApJ, 691, 770

—. 2004, MNRAS, 353, 391

—. 2011, MNRAS, 415, 545

Tollerud, E. J., Boylan-Kolchin, M., & Bullock, J. S. 2014, MNRAS, 440, 3511

Tolstoy, E., Hill, V., & Tosi, M. 2009, ARA&A, 47, 371

Tonry, J., & Davis, M. 1979, AJ, 84, 1511

Tonry, J. L., Dressler, A., Blakeslee, J. P., et al. 2001, ApJ, 546, 681

Tremaine, S., Gebhardt, K., Bender, R., et al. 2002, ApJ, 574, 740

Tremblay, B., & Merritt, D. 1996, AJ, 111, 2243

Umemura, M., Loeb, A., & Turner, E. L. 1993, ApJ, 419, 459

Valluri, M., Ferrarese, L., Merritt, D., & Joseph, C. L. 2005, ApJ, 628, 137

Valluri, M., Merritt, D., & Emsellem, E. 2004, ApJ, 602, 66

van Albada, T. S. 1982, MNRAS, 201, 939

van den Bosch, R. C. E., van de Ven, G., Verolme, E. K., Cappellari, M., & de Zeeuw, P. T. 2008, MNRAS, 385, 647

van der Marel, R. P., Cretton, N., de Zeeuw, P. T., & Rix, H. 1998, ApJ, 493, 613

van der Marel, R. P., & Franx, M. 1993, ApJ, 407, 525

Vera-Ciro, C. A., Helmi, A., Starkenburg, E., & Breddels, M. A. 2013, MNRAS, 428, 1696

Viel, M., Becker, G. D., Bolton, J. S., et al. 2008, Physical Review Letters, 100, 041304

Volonteri, M., & Perna, R. 2005, MNRAS, 358, 913

Walcher, C. J., Fried, J. W., Burkert, A., & Klessen, R. S. 2003, A&A, 406, 847

Walker, M. G., Mateo, M., & Olszewski, E. W. 2008, ApJL, 688, L75

—. 2009a, AJ, 137, 3100

Walker, M. G., Mateo, M., Olszewski, E. W., et al. 2006, AJ, 131, 2114

—. 2007, ApJL, 667, L53

—. 2009b, ApJ, 704, 1274

Walker, M. G., & Peñarrubia, J. 2011, ApJ, 742, 20

Wang, J., Frenk, C. S., Navarro, J. F., Gao, L., & Sawala, T. 2012, MNRAS, 424, 2715

Winge, C., Riffel, R. A., & Storchi-Bergmann, T. 2009, ApJS, 185, 186

Wolf, J., Martinez, G. D., Bullock, J. S., et al. 2010, MNRAS, 406, 1220

Wu, X. 2007, ArXiv Astrophysics e-prints

Zolotov, A., Brooks, A. M., Willman, B., et al. 2012, ApJ, 761, 71

Vita

John Jardel was born in Philadelphia and grew up in Cherry Hill, NJ. He went to college at Rutgers University where he developed his interest in astrophysics. After working with Professor Jerry Sellwood at Rutgers, he became interested in the study of dark matter in galaxies. In 2008, John left the Garden State for graduate school at the University of Texas in Austin where he worked with Karl Gebhardt in the field of dynamical modeling of galaxies. John has many interests outside of astronomy, including pitching for the Ultra Deep Fielders (UT Astronomy's softball team), playing volleyball, and cooking. John is leaving astronomy and is excited to start a new career as a Data Scientist at Square Root, Inc. in Austin.

Permanent address: The University of Texas at Austin
Department of Astronomy
2515 Speedway, Stop C1400
Austin, Texas 78712-1205

This dissertation was typeset with LaTeX[†] by the author.

[†]LaTeX is a document preparation system developed by Leslie Lamport as a special version of Donald Knuth's TeX Program.